INVESTIGATING MESOSCALE PHYSICAL PROCESSES FOR VERTICAL AND HORIZONTAL TRANSPORT IN THE BLACK SEA WITH THE IMPLEMENTATION OF A HIGH-RESOLUTION CIRCULATION MODEL

A THESIS SUBMITTED TO
THE GRADUATE SCHOOL OF MARINE SCIENCES
OF
MIDDLE EAST TECHNICAL UNIVERSITY

BY

EHSAN SADIGHRAD

IN PARTIAL FULFILLMENT OF REQUIREMENTS
FOR
THE DEGREE OF DOCTOR OF PHILOSOPHY
IN
OCEANOGRAPHY

SEPTEMBER 2019

Approval of the thesis:

INVESTIGATING MESOSCALE PHYSICAL PROCESSES FOR VERTICAL AND HORIZONTAL TRANSPORT IN THE BLACK SEA WITH THE IMPLEMENTATION OF A HIGH-RESOLUTION CIRCULATION MODEL

submitted by **Ehsan Sadighrad** in partial fulfillment of the requirements for the degree of **Ph. D. in Oceanography Department, Institute of Marine Sciences, Middle East Technical University** by,

Assoc. Prof. Dr. Barış Salihoğlu
Director of the **Institute of Marine Sciences**

Prof. Dr. Süleyman Tuğrul
Head of Department, **Oceanography**

Assoc. Prof. Dr. Bettina Fach Salihoğlu
Supervisor, **Depatment of Oceanography, Institute of Marine Sciences, METU**

Dr. Sinan Arkın
Co-Supervisor, **Depatment of Oceanography, Institute of Marine Sciences, METU**

Examining Committee Members:

Prof. Dr. Şükrü Beşiktepe
Institute of Marine Sciences and Technology, Dokuz Eylul University

Assoc. Prof. Dr. Bettina Fach Salihoğlu
Depatment of Oceanography, Institute of Marine Sciences, METU

Assist. Prof. Dr. Bilge Tutak
Naval Architecture and Ocean, Shipbuilding and Ocean Engineering, Istanbul Technical Unversity

Assist. Prof. Dr. Devrim Tezcan
Department of Marine Geology and Geophysics, Institute of Marine Sciences, METU

Assoc. Prof. Dr. Barış Salihoğlu
Depatment of Oceanography, Institute of Marine Sciences, METU

Date: 02.09.2019

I hereby declare that all information in this document has been obtained and presented in accordance with academic rules and ethical conduct. I also declare that, as required by these rules and conduct, I have fully cited and referenced all material and results that are not original to this work.

Name, Surname: Ehsan Sadighrad

Signature   :

ABSTRACT

INVESTIGATING MESOSCALE PHYSICAL PROCESSES FOR VERTICAL AND HORIZONTAL TRANSPORT IN THE BLACK SEA WITH THE IMPLEMENTATION OF A HIGH-RESOLUTION CIRCULATION MODEL

Ehsan Sadighrad

Ph. D., Department of Oceanography
Supervisor: Assoc. Prof. Dr. Bettina Fach Salihoğlu

September 2019, 127 pages

A three-dimensional, high resolution ocean model, the Nucleus for a European Model of the Ocean (NEMO) is set up for the Black Sea. It is used to simulate the general circulation of the Black Sea and investigate interannual variability of physical properties, dynamics and mesoscale features from 1985 to 2014. The model is validated by univariate and multivariate analyses, comparing the model results with available in situ and satellite data of sea surface temperature, salinity and sea surface height. The simulation of mesoscale eddies in the model is compared to eddies detected from satellite sea surface height data using an eddy statistics analysis. The relationship between wind, kinetic energy and current dynamics is studied to investigate variability in the simulated physical properties and upper layer dynamics. The main aim of thesis research is to investigate the impact of horizontal and vertical transport of water masses from the continental shelf to the basin interior and the exchange in the vertical dimension. Results show that mid-winter is the time of maximum kinetic energy transfer from atmosphere to the ocean. Then a strong Rim Current with maximum eastward transport dominates the circulation. In this time strong vertical, upwelling velocities are observed in the Rim Current and eddies. In late winter and early spring the weakening of wind results in a decrease of kinetic energy and the following generation of mesoscale eddies enhances onshore-offshore exchange. When kinetic energy reaches its minimum in summer, the number of eddies increase but they are not energetic enough to facilitate strong onshore-offshore water exchange. Vertical transport of water masses and hence nutrients rely on kinetic energy transferred from the atmosphere to the ocean. Larger vertical velocities are observed in winter and early spring as a result of deep mixing

and upwelling processes. Vertical velocities are reduced in late spring and summer when kinetic energy is minimum.

ÖZ

KARADENİZ'DE DİKEY VE YATAY TAŞINIMLA İLİŞKİLİ ORTA-ÖLÇEKLİ FİZİKSEL PROSESLERİN YÜKSEK ÇÖZÜNÜRLÜKLÜ SİRKÜLASYON MODELİ KULLANILARAK ARAŞTIRILMASI

Ehsan Sadighrad

Doktora, Oşinografi Anabilim Dalı
Tez Yöneticisi: Doç. Dr. Bettina Fach Salihoğlu

Eylül 2019, 127 sayfa

Bahsedilen çalışma kapsamında üç-boyutlu, yüksek çözünürlüklü okyanus modeli NEMO (Nucleus for a European Model of the Ocean) kullanılmıştır. Bu model ile Karadeniz'in genel sirkülasyonu simüle edilmiş ve fiziksel özelliklerin, dinamiklerin ve orta-ölçekli oluşumların 1985 - 2014 dönemindeki yıllar-arası değişkenliği araştırılmıştır. Model çıktıları in-situ ve uydu verisinde mevcut olan deniz yüzey sıcaklığı, tuzluluk ve deniz yüzey yüksekliği verisi ile tek ve çok değişkenli analiz kullanılarak valide edilmiştir. Orta-ölçekli girdapların model simülasyonları, uydu deniz yüzey yüksekliği verisinden elde edilen girdaplar ile girdap istatistik analizleri kullanılarak karşılaştırılmıştır. İşbu tez araştırmasının asıl amacı kıta sahanlığından iç basene su kütlesinin yatay ve dikey taşınımını ('upwelling') ve dikey yönlü alışverişi araştırmaktır. Bulgular atmosferden okyanusa en yüksek kinetik enerji transferinin gerçekleştiği kış ortası döneminde güçlü Rim Current'ın en yüksek doğu yönünde taşınıma ulaşarak sirkülasyona hükmettiğini göstermektedir. Bu dönemde Rim Current akıntısında ve onu çevreleyen girdaplarda yüksek dikey ve yukarı yönlü hızların oluştuğu görülmektedir. Kış sonu ve ilkbahar başı döneminde zayıflayan rüzgarlar kinetik enerjinin düşmesine neden olurken ve akabinde oluşan orta-ölçekli girdaplar kıyıdan açık denize su alışverişini destekler. Yazın kinetik enerji en düşük seviyesine ulaştığında girdapların sayısı artmaktadır ancak bu girdaplar güçlü kıyı-açık deniz su alışverişini destekleyecek kadar yüksek enerjili değillerdir. Su kütlelerinin dikey yönlü taşınımı ve dolayısıyla besin tuzu taşınımı atmosferden okyanusa transfer olan kinetik enerjiye bağlıdır. Kışın ve ilkbaharın başında, besin tuzlarının dikey taşınımını sağlayan derin karışım ve yukarı yönlü taşınım ('upwelling') prosesleri

sonucu daha yüksek dikey hızlar ölçülmektedir. Dikey hızların ilkbaharın sonunda ve yazın kinetik enerjinin minimum seviyesine düşmesiyle azaldığı görülmüştür.
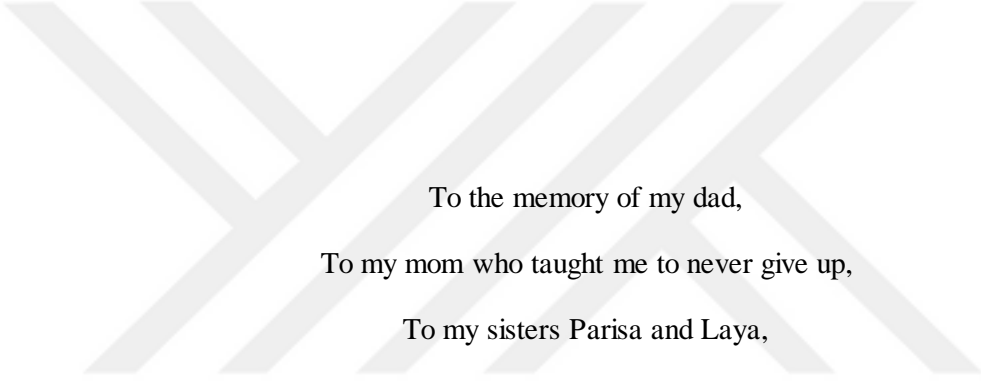
To the memory of my dad,

To my mom who taught me to never give up,

To my sisters Parisa and Laya,

To my wife Roshanak

To Omid and Ilya

ACKNOWLEDGEMENT

I am grateful to my supervisor Assoc. Prof. Dr. Bettina Fach Salihoğlu for her encouragement, enthusiasm and guidance in assisting me throughout this challenging research study.

I would like to thank Dr. Sinan Arkın, Assoc. Prof. Dr. Barış Salihoğlu, Dr. Sinan Hüsrevoğlu and Asst. Prof. Dr. Devrim Tezcan for their insight, suggestions and supports.

My special thanks is to Dr. Sinan Hüsrevoğlu and Dr. Sinan Arkın for their guidance in solving critical problems of my thesis study.

I would like to thank my thesis invited examining committee members Prof. Dr. Şükrü Beşiktepe and Asst. Prof. Dr. Bilge Tutak.

I would like to thank Mehmet Selim Keçeci and Mehmet Beklen for their helps in computer systems.

I would like to thank my friends in Setustu during my 6 years stay.

I would like to thank METU-IMS family for not letting me feel lonely during my studies.

I would like to thank my best friends who never left me alone in my hard times.

I would like to thank Ceren Güraslan, Şehmus Başduvar, Onur Karakuş and Gizem Akkuş for their friendships and supports.

And most importantly, none of this would have been possible without the love of my family, especially my mom who always encouraged me to do my best for my future.

Table of Contents

LIST OF TABLES

LIST OF FIGURES

LIST OF ABBREVIATIONS

ADT – Absolute Dynamic Topography

AVHRR – Advanced Very High Resolution Radiometer

CIL – Cold Intermediate Layer

CIW – Cold Intermediate Water

CLIO – Coupled Large-scale Ice Ocean

CMEMS – Copernicus Marine Environment Monitoring Service

CORE – Coordinated Ocean-ice Reference Experiment

DINEOF – Data Interpolating Empirical Orthogonal Functions

ECMWF – European Centre for Medium-Range Weather Forecasts

EKE – Eddy Kinetic Energy

EMODnet DTM – European Marine Observation and Data Network Digital Terrain Model

EOF – Empirical Orthogonal Function

Era-Interim – European Reanalysis Interim

GEBCO – General Bathymetric Chart of the Oceans

GLS – Ggeneric Length Scale

KPP – K Profile Parameterization

MAE – Mean Absolute Error

MBE – Mean Bias Error

MDT – Mean Dynamic Topography

MFS – Mediterranean Forecasting System

MKE – Mean Kinetic Energy

MLD – Mixed Layer Depth

NAO – North Atlantic Oscillation

NEMO – Nucleus for a European Model of the Ocean

NSME – Nash Sutcliffe Model Efficiency

NWS – NorthWestern Shelf

OASIS – Ocean Atmosphere Sea Ice Soil

OBC – Open Boundary Condition

OGCM – Ocean General Circulation Model

OPA – Ocean PArallelise

P_{bias} – Percentage Model Bias

r – Correlation Coefficient

RMSD – Root Mean Square Deviation

SLA – Sea Level Anomaly

SLP – Sea Level Pressure

SSH – Sea Surface Height

SST – Sea Surface Temperature

SSS – Sea Surface Salinity

STD – Standard Deviation

SVD – Singular Value Decomposition

TKE – Total Kinetic Energy

TVD – Total Variance Dissipation

WOA – World Ocean Atlas

CHAPTER 1

INTRODUCTION

Earth's average surface temperature increase is the main indicator of global warming. In addition to naturally warming and cooling of the earth over long periods of time, human activities play a major role in global warming (Haustein et al., 2017; Medhaug et al., 2017). Covering nearly 71% of the earth with an average depth of 3.8 km, oceans play a central role in climate system. Sea level changes, hydrological cycle changes, ocean currents variations are major impacts of global warming on regional climate. Hence, regional seas like the Black Sea that are societally important regions of the marine environment and potentially highly vulnerable to climate change (Holt et al., 2016). Variations in air temperature, precipitation anomalies, solar radiation, heat flux and wind stress fields as main drivers of climate change influence marine ecosystems at all levels from primary producers to higher predators (Oguz, 2005). Understanding the long term variations of physical properties and hydrodynamic features enables us to identify decadal scale variations and provides us to the knowledge to manage the oceans in order to confront problems arising from these variations (Dunstan et al., 2018). Understanding changes in biodiversity and the food web in the Black Sea requires long term study of its physical properties' variability and hydrodynamics. Several modeling studies have investigated interannual variability of Black Sea's hydrodynamics (e.g. Stanev and Beckers, 1999; Staneva et al., 2010; Knysh et al., 2011; Capet et al., 2012) and its biophysical and biogeochemical interactions, lower trophic level dynamics and food web changes (Akoglu et al., 2014; Cannaby et al., 2015; Salihoglu et al., 2017). An accurate modeling of biogeochemistry, ecosystem and fisheries requires precise modeling of physics. Horizontal advection and vertical exchange of nutrients and organisms play key roles in biogeochemical cycles of marine ecosystems (Barceló-Llull et al., 2016) and is largely dependent on mesoscale physical processes. Meso and sub-mesoscale features, such as eddies, fronts and filaments are ubiquitous in the ocean. Features characterized by large Rossby numbers at the ocean surface are associated with enhanced mixing and strong vertical velocities. They provide a pathway for energy transfer from the atmosphere to the mixed layer and possibly to greater depths which enhances nutrients availability in the euphotic zone and maintains primary production in the ocean (Zhong and Bracco, 2013; Jose et al., 2014). Physical processes such as eddy stirring and trapping, eddy induced horizontal transports, eddy pumping, eddy-wind interactions, unstable fronts, and ageostrophic cross-frontal circulation regulate nutrient transport and sustain productivity in open ocean systems (Oguz et al., 2016). In addition, frontal zones associated with

buoyant jets and boundary currents have been recognized as biogeochemical hot spots in coastal, marginal, and semi-enclosed seas (Oguz et al., 2016).

This thesis provides a detailed analysis of the physical dynamics in the Black Sea and their changes over the past 30 years (1985-2014) through modeling. Given the importance of mesoscale features overall, this thesis also studies the role of mesoscale physical processes in the Black Sea on the horizontal and vertical transport of water masses in an attempt to better understand the coupling between current flow and nutrient and plankton dynamics in this semi-enclosed sea. The thesis is structured as follows: The first chapter of this thesis provides an introduction to general characteristics of the Black Sea, its physical processes of the Black Sea and their importance, modeling of the Black Sea circulation dynamics and the aims of this thesis, respectively. The second chapter describes characteristics of the hydrodynamic model applied for modeling of the Black Sea, the atmospheric forcing, initial conditions, open boundary condition used for parameterization of the Bosphorus Strait. Univariate and multivariate validation of the model is performed to assess its skill in chapter three. In chapter four long term (1985-2014) variability of the Black Sea dynamics and its physical properties is studied. Results of the analysis and scientific scope of the study are discussed in chapter five and chapter six gives a brief summary and conclusion of the thesis study.

1.1 Black Sea

The Black Sea, known as the largest anoxic water body in the world (Oguz, 2005), extends approximately 630 km in the north-south direction between latitudes of 40°93' to 46° 61' N and nearly 1600 km in the east-west direction between longitudes of 27°46' to 41°8' E. It is an elongated and nearly-enclosed basin with a surface of 423,000 km^2 and total volume of 547000 km^3, situated between Europe, Anatolia and Causcasus, and connected through the Bosphorus Strait (with an average depth of about 50 m) to the Mediterranean Sea which is the only connection bounding the Black Sea to the Global Ocean (Oguz et al., 2005; Toderascu and Rusu, 2013) (Figure 1). Within the interior basin, the Black Sea extends down to a maximum depth of around 2200 m. In the north, the narrow Kerch Strait (less than 5m depth) connects the Black Sea with the shallow Sea of Azov. With relatively flat western and northern coastal regions, the Crimean Peninsula with a maximum elevation of slightly more than 400 m is the greatest relief in the region.

Generally, the basin can be divided into four physiographic provinces: the continental shelf, that covers the entire northwestern part of the Black Sea (~200 km width) west of the Crimean

peninsula, but barely exceeds 20 km width in the rest of the basin, excluding a few areas along the Turkish coast, eastern Russia and south of the Crimean peninsula; the basin slope, divided into two distinct types: a relatively steep slope, highly dissected by submarine canyons, and a relatively smooth slope with a more gentle gradient; the basin apron, where the slope has a gradient between 1:40 and 1:1000 similar to that of continental rise; and abyssal plain, in the center of the Black Sea with a gradient of less than 1:1000 which slopes gently to a maximum depth of 2206 m almost directly south of Yalta (Ross et al., 1974).

The northwestern region of the Black Sea consists of an approximate 200 km wide and 0-200 m deep shelf referred to as northwestern shelf (NWS), almost a triangle, narrowing towards the south along the Romanian, Bulgarian coast and occupying ~20% of the total Black Sea. It receives water input from four of Europe's largest rivers: Dniestr, Dniepr, Bug and particularly the Danube (Oguz and Besiktepe, 1999; Oguz et al., 2005; Toderascu and Rusu, 2013). The NWS contributes to about 70% of the Black Sea fresh water input (Blokhina and Afanasyev, 2003; Tsiaras et al., 2008). Hence, water in the NWS is typically colder, fresher and less dense than the open seas in both and winter (Zhou et al., 2014).

Freshwater discharge of ~290 km^3 yr^{-1} is maintained by the rivers Danube, Dniester, Dniepr and Bug in the NWS, Sakarya, Kizilirmak, Yesilirmak, Coruh and Filyos in the southern Turkish coasts and Rioni and Kodori in the southeast of the Black Sea as well as many other small rivers. In addition, an average excess of precipitation (~320 km^3 yr^{-1}) over evaporation (~315 km^3 yr^{-1}) have led the Black Sea to be a basin with a positive water balance (Ünlülata et al., 1990; Özsoy and Ünlüata, 1997), known as a dilution basin (Oguz et al., 1995). The excess of freshwater (~300 km^3 yr^{-1}) is balanced by the net outflow (~300 km^3 yr^{-1}) through the Bosphorus Strait (Ünlülata et al., 1990).

The general circulation of the Black Sea (Figure 2) is characterized by a persistent cyclonic boundary current referred to as the Rim Current with a speed of 50-100 cm/s within the upper layer, and about 10-20 cm/s within the 150-300 m depth range, and a series of seasonal anticyclonic eddies and meanders propagating cyclonically between the Rim Current and the coast around the basin (Oguz and Besiktepe, 1999; Blokhina and Afanasyev, 2003;Korotaev et al., 2003; Oguz et al., 2005; Capet et al., 2012). Apart from anticyclonic eddies transient mesoscale activities in the form of meanders, ubiquitous mesoscale eddies, dipoles and filaments are observed on both sides of the Rim Current (Blokhina and Afanasyev, 2003; Korotaev et al., 2003). The interior of the basin is composed of two or more interconnected cyclonic gyres referred to as the western and eastern gyres.
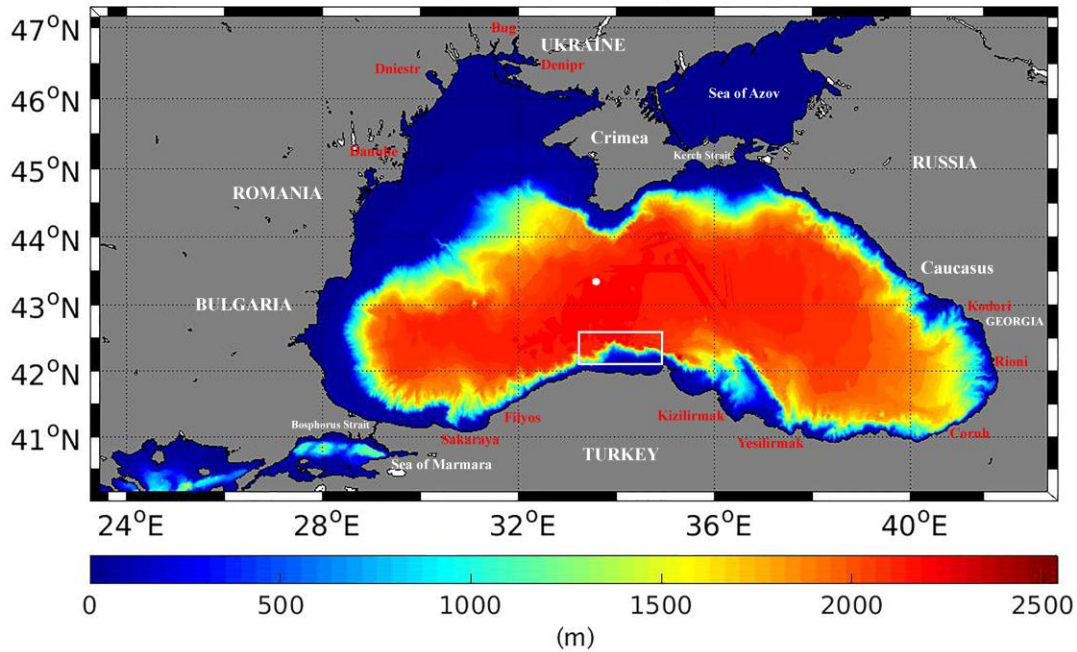
Figure 1: The Black Sea bottom topography constructed from the 0.125 arc-minute resolution dataset of European Marine Observation and Data Network Digital Terrain Model (EMODnet DTM). Geographical locations of the 11 main rivers considered in the study are shown in red color text. White circle denotes a grid point approximately in the center of the basin between western and eastern gyres where vertical structure of temperature, salinity, density and characteristic features of the Black Sea is investigated. White box in the south marks the area over which horizontal and vertical transport is investigated (in section 4.3).

The Black Sea is a highly stratified basin which can be classified into three vertical layers that do not mix (Murray et al., 1991; Ozsoy and Unluata, 1997; Korotaev et al., 2003; Stanev et al., 2004; Stewart et al., 2007; Toderascu and Rusu, 2013); the thin and the most active mixed surface layer, an intermediate layer where the so called Cold Intermediate Layer (CIL) is found and a deep layer. The mixed layer ranges from a few (~5 m) meters in summer (Kara et al., 2008) to between ~70 and 140 m depth in winter (Cannaby et al., 2015) and is strongly influenced by seasonal temperature variations, variations in wind forcing and river discharge. The second layer is formed by the stratification of the surface layer during spring warming. Below the seasonal thermocline, convectively generated cold water is trapped and limited by the permanent halocline (Capet et al., 2013). A process that leads to the formation of the CIL with a minimum temperature of ~6-8 °C located between the halocline (~100-150 m) and the summer thermocline (~20-50 m) (Capet et al., 2013; Akpinar et al., 2017). A small area, west of the Crimean Peninsula and the northern part of the

central basin are known as the main two important regions of formation of the CIL cold and dense water (CIW), accounting for ~42% and ~28% of the annual CIW production, respectively (Capet et al., 2013; Stanev et al., 2003), however formation has even been observed in anticyclonic coastal eddies (Akpinar et al., 2017). Below the CIL lies the bottom layer. CIL ventilation plays a major role in oxygen input in subsurface layers (Stewart et al., 2007) and the bottom of the CIL is situated between the halocline and thermocline (Capet at al., 2012) at the onset of the suboxic layer (Stanev et al., 2018). Hence, CIL thickness is an important parameter in oxygen supply of subsurface layer.
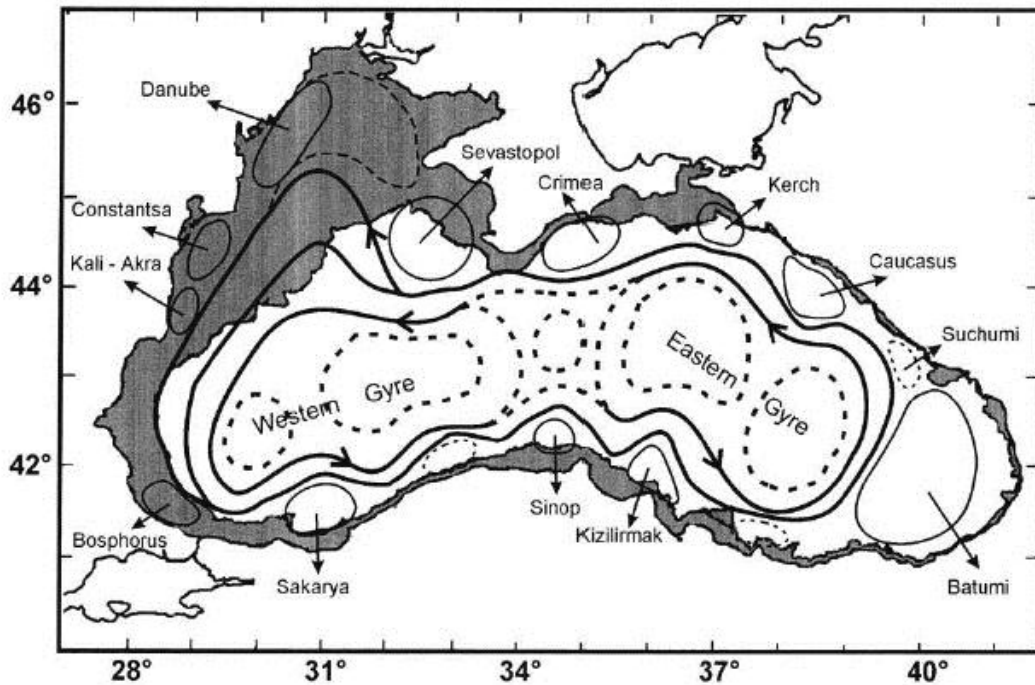
Figure 2: General circulation of the Black Sea (reproduced from Korotaev et al., 2003).

A south to north temperature gradient in the mixed surface layer is revealed by Oguz et al., (1993), showing increasing temperatures along the southern coast from 18.0 °C to 19.5 °C in the cyclonic features of the basin's interior to higher temperatures observed within the anticyclonic eddies, reaching 23.0 °C in the Batumi Eddy region (southeast of the Black Sea) (Oguz et al., 1993). At the central western basin, a sharp decrease of potential temperature from a surface value of 16.664 °C to a minimum value of 6.970 °C at 44 m in the CIL, and then increase to 8.773 °C at 200 m is observed which indicates vertical redistribution of water temperature (Murray et al., 1991).

The enclosed state of the Black Sea and high river discharge has resulted in its lower salinity than the open seas or oceans with an average salinity of ~18 psu at the surface layer increasing to ~22 psu at the bottom layer. Strong stratification of the Black Sea waters prevents mixing of surface layer and bottom layer (receiving saline water from the Mediterranean Sea) is the main reason for the maintenance of the salinity difference. The salinity at the central western basin increases rapidly with depth from a value of 18.289 psu at the surface to a maximum value of 22.321 psu at the bottom (Murray et al., 1991).

1.2 Important Physical Processes in the Black Sea

Physical processes are known as a primary determinant of marine ecosystems dynamics enhancing occurrence of biological processes (Lima et al., 2002). Mesoscale (of the order of 10^2 km) processes are an important vehicle for nutrient transport and play an important role in influencing the distribution and rates of biological processes as well as community structure (Mc Gillicuddy et al.,1998; Lima et al., 2002). Mesoscale physical phenomena such as eddies, fronts (i.e. narrow zones of enhanced horizontal gradients in water properties which separate border areas with different water masses or different vertical structure) and filaments are ubiquitous features of the oceans. They can enhance productivity and biological patchiness through water and communities transport across large horizontal distances or enhance primary production through transport of nutrients to the euphotic zone in upwelling regions which is of paramount importance. Fueling primary production through spatially discrete and temporally episodic nutrient fluxes where phytoplankton growth is nutrient limited is known to be dependent on small scale vertical motions of nutrients as a result of physical dynamics at frontal zones (of the order of 10 km) (Li et al., 2012). Frontal zones are known as increased mixing areas both laterally and vertically which result in surface water fertilization, primary and secondary production increase and are thus characterized by high planktonic biomass (Acha et al., 2004; Oguz et al., 2014).

In the core of cyclonic eddies the uplift of isopycnal surfaces upwells nutrient-rich subsurface water into the euphotic zone, while the entrainment of nutrients from the euphotic zone through the deepening of isopycnal surfaces in the core of anticyclonic eddies takes place. Primary production is sustained through such vertical flux of nutrients (Jose et al., 2014). Development of ageostrophic circulation by unstable fronts also provides significant nutrient upwelling. Baroclinic instability wave development in unstable fronts triggers the formation of divergence and convergence (frontolysis and frontogenesis) and, consequently, upwelling and downwelling zones along the jet advect

nutrients upward along the isopycnals or entrains nutrients to aphotic zone to sustain primary production (Lima et al., 2002; Pitcher et al., 2010; Oguz et al., 2014; Oguz et al., 2016).

The Rim Current is situated over the continental slope zone (Oguz and Besiktepe, 1999) can act as a biogeochemical barrier between coastal and offshore waters (Oguz et al., 1994). However, it exhibits meanders and cross-stream jets with offshore jets extending more than 100 km from the shelf break with peak velocities of about 70 cm/s (Oguz et al., 1994), and as a frontal zone plays a major role in the Black Sea ecosystem. Along with strong buoyancy-induced vertical mixing, the Rim Current, with mesoscale eddies propagating cyclonically around the basin and longshore currents can serve as sources of nutrients and their lateral distributions may contribute to basin-wide plankton productivity (Oguz, 2017) in the Black Sea. Eddies in the Black Sea are influenced by the strength of the Rim Current varying by the seasonal change of the wind stress curl (Kubryakov and Stanichny, 2015).

In winter Rim Current is fueled by strong winds and can act as a barrier which inhibits the exchange of water masses between the shelf and interior basin. In contrast, weakening of the Rim Current in summer due to changes in wind stress results in baroclinic instability leading to enhanced mesoscale eddy activity in the Black Sea (Kubryakov and Stanichny, 2015). Cyclonic and anticyclonic eddies influence the water exchange in horizontal and vertical directions, leading to onshore-offshore as well as vertical exchange of tracers and nutrients. Therefore, a high resolution model capable of detecting mesoscale eddies and their abundance in the Black Sea will give a better understanding of the influence of these hydrodynamic features on nutrient transport and consequently, biological productivity.

The main objective of this thesis is to study the role of physical mechanisms in supplying nutrients for primary production in the Black Sea through the use of a General Circulation Model that reproduces the circulation of the Black Sea including the mesoscale features that are known to play an important role in nutrient transport. Nutrient dynamics are not directly modelled but inferred from the transport of water masses.

1.3 Modeling Black Sea Circulation Dynamics

To understand the dynamics of marine environments (oceans and regional seas) and to predict future changes of these systems, numerical modeling is an invaluable tool. While in-situ oceanographic instruments provide measurements that only sparsely cover the oceans in space and time and satellites

measure data only at the sea surface, ocean general circulation models provide high resolution data covering the entire ocean including the whole water column. Exploring the oceanographic characteristics of marine environments requires both observational and modelling efforts. Despite significant improvements in ocean modeling studies, the state-of-the-art ocean general circulation models require high resolution configurations to resolve important of dynamical features, such as meso and sub-mesoscale eddies, frontal jets, tides and tidally rectified transports (Graham et al., 2017; Wang et al., 2017).

A high level of understanding of biogeochemical processes and primary production dynamics requires high-resolution hydrodynamic models that can resolve meso- and sub-mesoscale features important for the redistribution of ocean properties. These measoscale features may be vortices and currents with a horizontal scale of about 5-10 km contribute to the coastal dynamics and energy (Demyshev et al., 2016). Numerical modeling of the Black Sea as a basin with unique natural conditions like positive net freshwater, ubiquitous mesoscale structures, strong density stratification, distinct vertical biogeochemical structure and a basin wide cyclonic circulation is of growing interest. In addition, ocean observation satellite images of the Black Sea reveal presence of smaller scale processes and features such as sub-mesoscale fronts, filaments and eddies not only in coastal areas and at the shelf edge, but also in open sea (Shapiro et al., 2010; Mizyuk et al., 2016). Hence, resolving the Black Sea general circulation including these meso- and sub-mesoscale features, investigating their seasonal and interannual variability and their role in the exchange between coastal areas and open sea, requires the development of a high resolution numerical hydrodynamic model, as is applied in this study.

Numerous modeling studies have been carried out to simulate the general circulation of the Black Sea. A pioneering modeling study of the Black Sea was conducted by Oguz et al., (1995) to identify the relative contribution of the three primary forcing mechanisms (wind stress, surface thermohaline fluxes and lateral buoyancy fluxes) that determine the Black Sea large scale circulation. Since then several numerical models have been implemented to simulate seasonal and interannual variability of the Black Sea thermohaline circulation and its hydrodynamic features (e.g. Oguz and Malanotte-Rizzoli, 1996; Stanev and Beckers, 1999; Stanev et al., 2002; Vandenbulcke et al., 2009; Vandenblucke et al., 2010; Stanev et al., 2010; Capet et al., 2012) and study the impact of future climate change scenarios on the Black Sea (Cannaby et al., 2015). Recently, numerical models with increased spatial resolution have been implemented to simulate general circulation of the Black Sea (e.g. Zhou et al., 2014; Korotenko, 2015; Mizyuk et al., 2016; Zalesnyi et al., 2016; Miladinova et al., 2017; Stanev et al., 2017) providing more detailed results compared to earlier numerical

simulations, resolving mesoscale eddy fields, seasonal variations of the Rim Current, cyclonic gyres in the deep sea, numerous anticyclonic eddies between the Rim Current and the coast, systems of currents and countercurrents and exchange between the shelf and the deep sea region. However, the aim of this study, investigating role of meso- and sub-mesoscale features and their seasonal and interannual variability in the nutrient exchange between coastal areas and open sea has not yet been investigated by any previous modeling study. There is however one study attempting it with the use of altimetry data (Kubryakov and Stanichny, 2015).

The primitive equation ocean model NEMO (Nucleus for a European Model of the Ocean), described in detail in Madec (2015), is a state-of-the-art modeling framework of ocean related engines, enables the investigation of oceanic circulation and its interaction with the atmosphere (OPA), biogeochemical processes (TOP-PISCES) in the ocean and Ice coupled modeling (LIM) (Reffray et al., 2015). NEMO is widely used for oceanographic research, operational oceanography, seasonal forecast and climate studies (e.g. Storkey et al., 2010; O'dea et al., 2012; Martin et al., 2015; Neves et al., 2016). OPA, the ocean core of NEMO solves the primitive equations for an incompressible fluid (under the hydrostatic and Boussinesq approximations) on a structured Arakawa-C grid with model state variables horizontally/vertically staggered (Soontiens et al., 2016; Trotta et al., 2016). The three-dimensional velocity field, sea surface height, temperature and salinity constitute prognostic variables of the physical ocean component of NEMO. In the vertical direction the model is able to use full or partial step z-coordinates, or s-coordinates, or a mixture of the two. The steep slope of the Black Sea basin topography necessitates application of a z-coordinate numerical model to simulate general circulation of the Black Sea; thus, together with various vertical mixing and advection/diffusion schemes this ability makes NEMO capable of modeling the circulation of the Black Sea in a high spatial resolution.

1.4 Aims of the Study

The main aim of this thesis is to study the changes of important physical parameters and processes such as changes in water temperature, water mass formation, mixed layer depth, cold intermediate layer and formation of eddies to name a few over the past 3 decades (1985 -2014) and how they may be related to the observed climate variability. In addition, the role of these physical mechanisms in supplying nutrient for primary production in the Black Sea is being investigated. This includes assessing the relative importance of mesoscale eddies observed along the Rim Current on the lateral and vertical transport of nutrients into the interior of the Black Sea.

This study investigates:

- Interannual variability of physical parameters
- General circulation and current dynamics of the Black Sea
- Causes of Black Sea circulation and how the transport of water masses is influenced by different physical processes

<center>

CHAPTER 2

MODEL CHARACTERISTICS AND SETUP

</center>

2.1 Nucleus for a European Model of the Ocean (NEMO)

NEMO, a numerical modeling tool comprised of three ocean related engines (OPA: ocean; LIM: sea-ice; TOP-PISCES: biogeochemistry), developed and operated within a European consortium, is a generalized (z-level / terrain-following s- / or a mixture of the two) coordinate primitive equation model which original features have been described by Madec (2015). The OPA (Ocean PArallelise) engine of NEMO for the ocean dynamics and thermodynamics (Blue Ocean) has been developed from the 8.2 release of the OPA model (Madec, 2015). The OPA engine of NEMO is used for both regional and global ocean modeling as an atmospherically forced ocean model and as a coupled atmosphere-ocean model.

The model describes the ocean with the primitive equations, i.e. the Navier-Stokes equations together with the nonlinear equation of state. The vector invariant form of primitive equations is comprised of six prognostic equations; the momentum balance, the hydrostatic equilibrium, the incompressibility equation, the heat and salt conservation equations and the equation of state (Madec, 2015). The vector form of the abovementioned equations in the *(i,j,k)* vector system are (Madec, 2015):

$$\frac{\partial \mathbf{U}_h}{\partial t} = -\left[(\boldsymbol{\nabla} \times \mathbf{U}) \times \mathbf{U} + \frac{1}{2}\boldsymbol{\nabla}(\mathbf{U}^2)\right]_h - f\mathbf{k} \times \mathbf{U}_h - \frac{1}{\rho_0}\boldsymbol{\nabla}_h \mathrm{p} + \mathbf{D}^{\mathbf{U}} + \mathbf{F}^{\mathbf{U}} \qquad (1)$$

$$\frac{\partial p}{\partial z} = -\rho \boldsymbol{g} \qquad (2)$$

$$\boldsymbol{\nabla} \cdot \mathbf{U} = 0 \qquad (3)$$

$$\frac{\partial T}{\partial t} = -\boldsymbol{\nabla} \cdot (T\mathbf{U}) + \mathrm{D}^T + \mathrm{F}^T \qquad (4)$$

$$\frac{\partial S}{\partial t} = -\boldsymbol{\nabla} \cdot (S\mathbf{U}) + \mathrm{D}^S + \mathrm{F}^S \qquad (5)$$

$$\rho = \rho(T, S, p) \qquad (6)$$

<center>11</center>

where **U** is the vector velocity ($\mathbf{U} = U_h + w\boldsymbol{k}$), $\boldsymbol{\nabla}$ is the generalized derivative vector operator in (i,j,k) directions, t is the time, z is the vertical coordinate, T is the potential temperature, S is the salinity, ρ is the *in-situ* density given by the equation of state (equation 6), ρ_0 is a reference density, p the pressure, f is the Coriolis acceleration ($f = 2\boldsymbol{\Omega} \cdot \boldsymbol{k}$) and g is the gravitational acceleration. Parameterization of the small-scale physics for momentum, temperature and salinity is introduced by $\mathbf{D}^{\mathbf{U}}$, D^T and D^S and surface forcing terms are defined as $\mathbf{F}^{\mathbf{U}}$, F^T and F^S.

The three-dimensional velocity field, sea surface height, temperature and salinity are the prognostic variables (Epicoco and Mocavero, 2012). Explicit, split-explicit and filtered free surface formulations provide choices to solve prognostic equations of the active tracers and momentum (Epicoco and Mocavero, 2012; Madec, 2015). Coriolis and momentum advection terms are calculated using a leapfrog scheme and a number of different numerical schemes can be applied to compute the pressure gradient. In addition, several numerical schemes can be applied to the momentum advection, as well to the advection of tracers.

Six fields (two components of the surface ocean stress, the two incoming solar and non-solar heat fluxes, the surface freshwater budget and the atmospheric pressure at the surface ocean) are defined as surface boundary conditions. To provide the model with these six fields, five different formulations/modules are considered: analytical surface boundary conditions in which six fluxes required by the ocean are assumed to be uniform; flux formulation which enables reading the surface boundary condition fields directly from input files; bulk formulation (coordinated ocean-ice reference experiment (CORE) by Large and Yeager (2004) and coupled large-scale ice ocean (CLIO) bulk formulation by Goosse et al. (1999)) which computes surface boundary condition fields using bulk formulae and atmospheric fields and ocean (and/or ice) variables; Mediterranean forecasting system (MFS) bulk formulae by Castellari et al. (1998); and coupled formulation by which the fluxes are provided by the ocean atmosphere sea ice soil (OASIS) coupler (Madec, 2015). Computation of vorticity along the coastline is carried out through four different types of lateral boundary conditions (lateral boundary: a coastline or an intersection with bottom topography which influences relative vorticity and momentum diffusive tends) (Madec, 2015).

As the first open boundary option, the open boundary package OBC has been developed in NEMO to allow the user to define boundary geometry, the forcing data at boundaries and the radiation algorithm at the open boundary (Madec, 2015). Hence, applying open boundary option of NEMO enables user to let information enter the model from outer ocean and/or the perturbation generated inside the computational domain leave without deterioration of the inner model solution.

Accordingly, OBC enhances consideration of inflow/outflow of flux into/from domain as a computational border (Madec, 2015).

Computation of the spatial and temporal variations of the eddy coefficients is carried out by applying lateral physics schemes. For this purpose, different lateral physics schemes are available to compute eddy coefficients variations, the direction along which the lateral diffusive fluxes are evaluated (i.e. model level, geopotential or isopycnal surfaces) and the type of operator (harmonic or biharmonic) for tracers and momentum (Madec, 2015).

Features like shear instability, internal wave breaking and etc. are assumed as the major sources of vertical turbulence which occur at scales smaller than model resolution and hence, turbulent motions are parameterized and never solved explicitly. It is assumed that vertical turbulent fluxes linearly depend on large scale quantities' gradients (Madec, 2015). Several choices are available to compute the vertical eddy viscosity and diffusivity coefficients (i.e. turbulent coefficients) in NEMO. The simplest choice is to assume that the coefficients of viscosity and diffusivity are constant or parameterize them as a function of Richardson number (Madec, 2015; Reffray et al., 2015). Turbulent closure scheme, generic length scale (GLS) and K profile parameterization (KPP) are more complex methods which use the turbulent kinetic energy and the mixing length to estimate the turbulent coefficients (Madec, 2015; Reffray et al., 2015). The turbulence scheme choice plays an important role in computation of eddy viscosity and diffusivity and hence, vertical mixing which creates the mixed layer depth (MLD). Precise computation of the MLD is of paramount important for its role in the energetic exchanges between the ocean and the atmosphere and biogeochemical processes.

2.2 Black Sea Adaptation of the NEMO Model

In this section of the thesis the specific parameters, different schemes used, initial conditions, and forcing applied to the Black Sea adapted NEMO model developed in this study are described in detail. The model is run for 30 years covering the time frame 1985-2014. In the current setup Kerch Strait is closed, but the Bosporus is parameterized as an open boundary, which is also described in detail below.

2.2.1 Model Setup

In this subsection, the schemes used for the advection of tracers, vertical diffusion and constant parameters used in the Black Sea model are briefly described. To calculate advection for tracers the Total Variance Dissipation (TVD) formulation is used, which evaluates the tracer at velocity points using a combination of an upstream and a centered scheme (Madec, 2015) which is a computationally quite expensive but positive scheme and can be used for both active and passive tracers.

Accurate determination of the ocean stratification requires precise computation of the ocean stability which is used in several ocean parameterizations (Madec, 2015). In the model adapted to the Black Sea, GLS turbulence closure model (Umlauf and Burchard, 2003) based on two prognostic equations (one for the turbulent kinetic energy and another for a turbulent quantity used in the transport equation) (Reffray et al., 2015; Madec, 2015) is used to compute the vertical eddy viscosity and diffusivity coefficients. This GLS closure scheme is largely able to reproduce the stratification/homogenization cycle observed at PAPA station as the test case (Reffray et al., 2015) and hence is used for the Black Sea model. Constant parameters used in the Black Sea model are provided in Table 1.

Table 1. Constant parameter values used in the NEMO Black Sea model simulations.

Description of the constants used in the Black Sea model	Value
Fraction of light penetration in non-penetrative wavebands	0.073
Shortest depth of penetration (m)	0.5
Longest depth of penetration (m)	7.5
Horizontal eddy diffusivity for tracers (m^2/s)	-1.0e+8
Horizontal bilaplacian eddy viscosity (m^4/s)	-1.5e+8
Galperin limit	0.267
Minimum value of the turbulent kinetic energy	1.0e-7
Minimum value of the dissipation rate	1.0e-12
Minimum surface roughness	0.02
Baroclinic time step (s)	360
Barotropic time step (s)	12
Number of Barotropic iterations	30
Asselin time filter parameter	0.1

2.2.2 Model Resolution and Constants

The NEMO model adapted to the Black Sea in this study is based on GYRE configuration of NEMO which has been built to simulate the seasonal cycle of a double-gyre box model which provides the investigation of the spontaneous generation of a large number of interacting, transient mesoscale eddies and their contribution to the large-scale circulation (Madec, 2015). The model employs Arakawa-C grid of a resolution of $\Delta x = \Delta y = 0.027°$ (3×3 km $- 1/36.1°$), comprised of 544 and 235 zonal and meridional array sizes, respectively.

The model uses a z-level vertical coordinate system with 61 z-levels. Vertical grid spacing is finer near surface (5 m) to reasonably resolve the vertical structure at the top layers (i.e. vertical water column physical properties such as the mixed layer depth, stratification and current dynamics mainly vertical velocities) and increases with depth to 100 m at the bottom. The maximum depth in the model is 2201.5 m. A detailed explanation is provided here on the z-level coordinate systems and its specifications. The z-level coordinates use depth as vertical coordinates and represent irregular topography as a number of steps (Winther and Evensen, 2006). Modeling of the Black Sea as the world's largest landlocked basin with its NWS occupying ~20% of its total area requires an adequate resolution of the near-bottom dynamics to accurately resolve diapycnal mixing arising primarily through internal waves breaking (Hill et al., 2012) and exchanges between the shelf and the deep sea (Shapiro et al., 2013). It is used in this study because a major limitation of terrain-following sigma coordinates (σ-coordinates) is the occurrence of errors in calculations of the pressure gradient force, which is associated with extrapolations that are required near the sea bed and is partly caused by violating the condition for "hydrostatic consistency" (Kliem and Pietrzak, 1999; Shapiro et al., 2013). On a sloping topography like the Black Sea, hydrostatic consistency condition is severely restrictive. Kliem and Pietrzak (1999) have shown that z-level based methods provide a notable decrease in the error. For the Black Sea, findings of Shapiro et al. (2013) carried out for a number of idealized and real world settings have shown that the best performance is achieved applying a z-coordinate grid.

Two choices are available in NEMO for z-level vertical coordinates: 1) z-level coordinates with full step bathymetry (Figure 3a) and 2) z-level coordinates with partial step bathymetry (Figure 3b). Full step z-level coordinates approximate the true ocean depth to the closest model level, whilst, partial step z-level coordinates make the bottom depth cell variable and adjustable to the real depth of the ocean, providing better representation of small topographic slopes (Bernard et al., 2006). Pressure gradient error and spurious diapycnal diffusion are minimized applying partial step z-level vertical coordinates (Pacanowski and Gnanadesikan, 1998). Pacanowski and Gnanadesikan (1998)

have shown that by increasing horizontal resolution of the model, the partial step discretized bottom topography improves significantly and hence the vertical topographic features are resolved at the scale of the horizontal resolution.
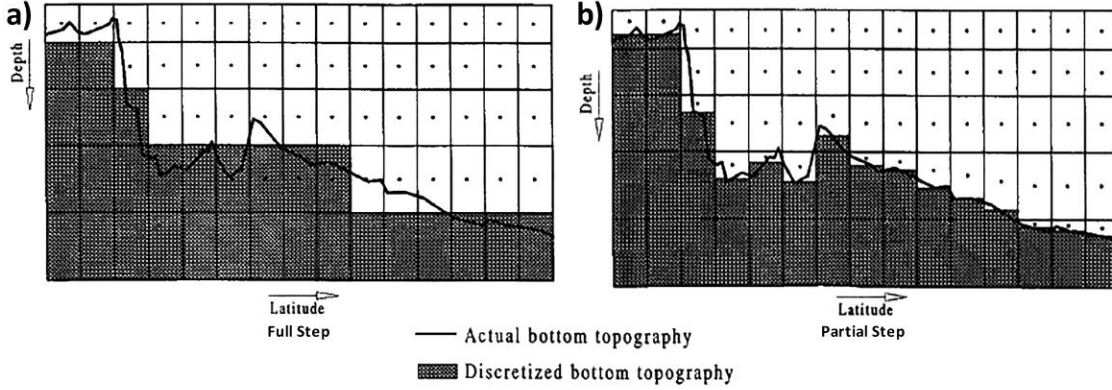
Figure 3: An example for comparison of full step (a) and partial step (b) discretization of bottom topography in z-level coordinate system from (reproduced from Pacanowski and Gnanadesikan, 1998).

2.2.3 Bottom Topography

The bathymetry in the Black Sea model (Figure 1) was derived from 30-seconds resolution provided by General Bathymetric Chart of the Oceans (GEBCO). The bathymetry is interpolated to the Black Sea model grid and smoothed to alleviate horizontal pressure gradient and vorticity error (Sikirić et al., 2009; Martinho and Batteen, 2006). A slope parameter is used to prevent pressure gradient errors. The slope parameter r representing a numerical resolution parameter is defined by:

$$r = \frac{|\delta H|}{2\bar{\bar{H}}} \qquad (7)$$

where $0 < r < 1$, δH is the difference in adjacent cell depths and $\bar{\bar{H}}$ is the mean depth (Mellor et al., 1998).

Generally, r the slope parameter does not exceed the maximum of $r_{max} \approx 0.2$ (Lemrie et al., 2012) or $r_{max} \approx 0.5$ (Penven et al., 2008). This is achieved using iteratively Shapiro filter (Figure 4 and Figure 5). The extent of smoothing has a strong influence on the circulation of models (Penduff et al., 2002). It is believed that to avoid numerical noise the topography should not vary too much at the grid scale. Hence, two passes of Shapiro filter were applied to smooth the topography (Bernard

et al., 2006). Figure 4b shows that after smoothing most of the topographic features (Figure 4a) still remain. After smoothing the maximum slope parameter is reduced to 0.2 (Figure 4b). The only difference is in the continental slope, the canyons are slightly wider and sharp seamounts are slightly flatter (Figure 5- blue line) than the unsmoothed bottom topography (Figure 5- red line).
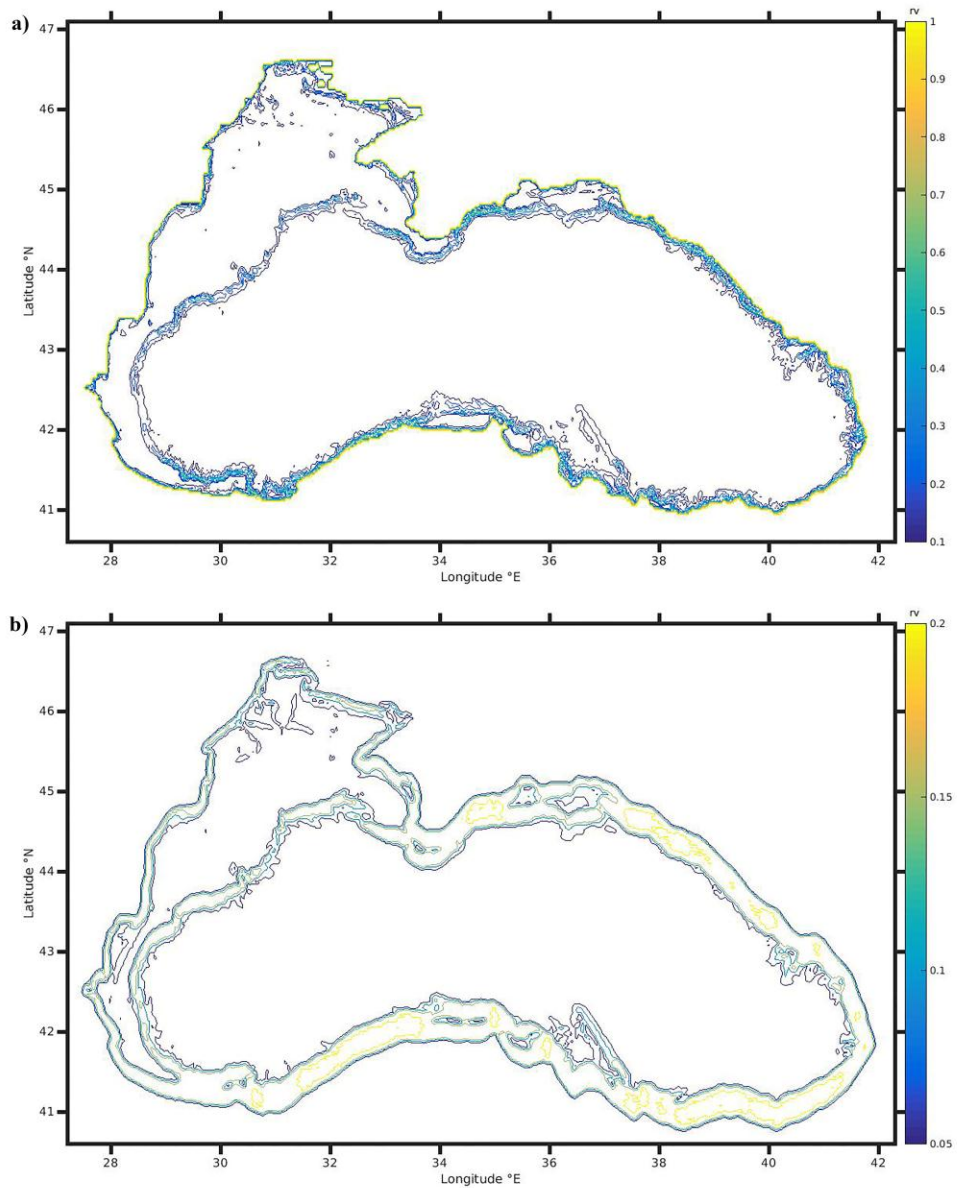
Figure 4: Contour plot of raw topography of the Black Sea (a), and the smoothed topography using Shapiro smoothing filter (b) with slope parameter (r_max ≈ 0.2).
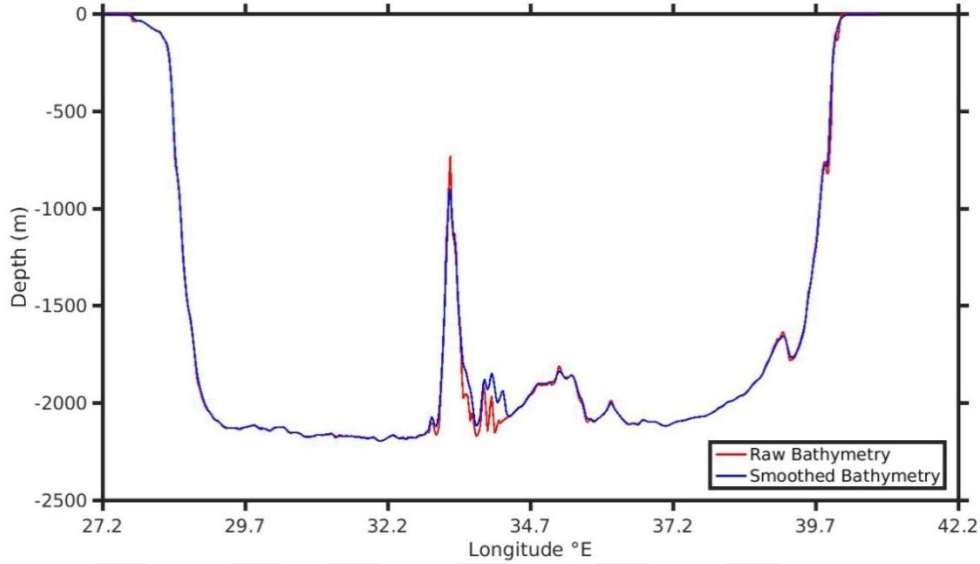
Figure 5: Comparison of normal depth sloping to the bottom (red line) and the slope after smoothed by iterative Shapiro filter (blue line).

2.2.4 Temperature and Salinity Initialization

Temperature and salinity initial conditions for the initialization of the Black Sea model are obtained using Decadal Monthly Mean Climatology (1955-2012) data set from the $0.25° \times 0.25°$ resolution World Ocean Atlas (WOA) 2013 (Locarnini et al., 2013; Zweng et al., 2013). The entire data set for the month of January is averaged to provide the initial conditions for the model run (Figure 6). Data covers the Black Sea region with 57 levels in the vertical direction, with the deepest level reaching 1800 m. Since the coverage of the data is not basin wide and is coarse, spatial interpolation has been applied to produce values of temperature and salinity at locations where there are no field measurements based on measurements taken at other locations for initial conditions of temperature and salinity. A Spring Metaphor interpolation method which assumes springs with a nominal length of zero connecting each node with every neighbor horizontally, vertically and diagonally has been used to interpolate missing values throughout basin.

2.2.5 Wind and Thermal Forcing

Surface fluxes of momentum and heat are of paramount importance in ocean simulations. The Era-Interim (European reanalysis interim version) dataset of the European Centre for Medium-Range

18

Weather Forecasts (ECMWF) provides global climate reanalysis describing the state of the atmosphere since 1979
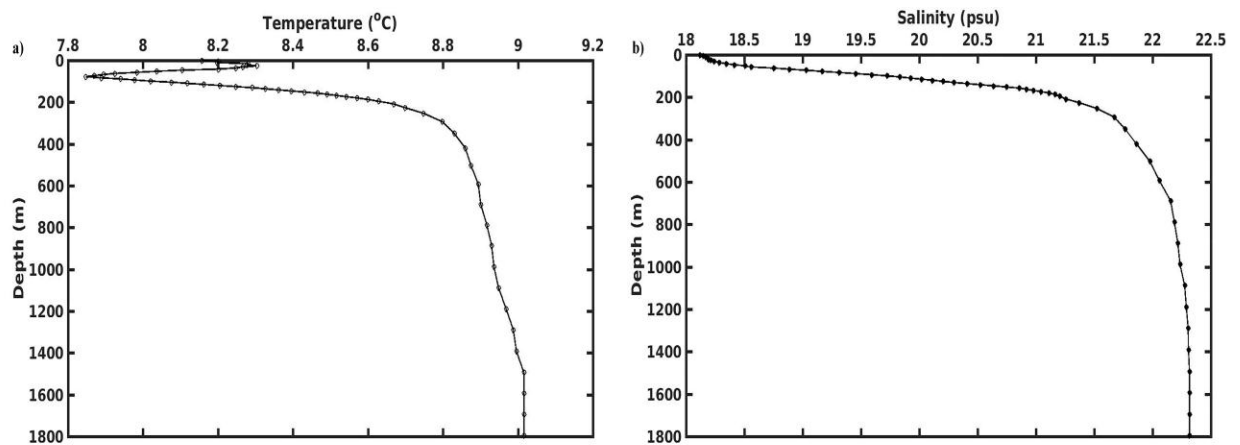
Figure 6: Decadal averaged initial temperature (a) and salinity (b) profiles for January from WOA 2013 (Locarnini et al., 2013; Zweng et al., 2013).

to date on a $0.125° \times 0.125°$ grid and continues to be updated in near-real-time as new data becomes available. A sequential data assimilation scheme was applied to produce Era-interim reanalysis, advancing forward in time (Dee et al., 2011) with approximately 79 km spatial resolution and 6 hourly (3 hours' time-step) surface parameters which adequately capture the variability of meteorological parameters (Karger et al., 2017). The model is forced with 3 hourly atmospheric parameters of wind and thermal forcing, precipitation, air temperature and specific humidity for the time frame of 1985-2014. Wind forcing is comprised of zonal and meridional 10 m wind stress magnitudes (Figure 7). Surface boundary condition in NEMO is computed using bulk formulae and six fields (two components of the surface ocean stress, the incoming solar and non-solar heat fluxes and the surface freshwater budget) and ocean variables. For the computation of fluxes over the ocean surface CORE bulk formulae is used. CORE bulk formulae developed by Large and Yeager (2004) applies an inertial dissipative method used to compute turbulent transfer coefficient (momentum, sensible heat and evaporation) from 10-m wind speed, air temperature and specific humidity (Madec, 2015).

Wind stress on the sea surface representing the velocity structure in the ocean-atmosphere boundary layer plays a key role in oceanic circulation. As the main source of energy for the ocean circulation, wind stress is of paramount importance in modulation of the vertical turbulence and mixing (Kubryakov et al., 2019). Seasonal and interannual variabilities of mesoscale circulation of

the Black Sea as a result of Ekman pumping are generated by the wind curl as the main force driving the Black Sea circulation (Kubryakov et al., 2019). Generally, winds in the black Sea highly influence vertical mixing and eddy dynamics, (Kubryakov et al., 2019; Kubryakov et al., 2016). Specific wind patterns are generated by mountains – the Balkans, the Pontic Mountains, the Caucasus and the Crimean Mountains– surrounding a great portion of the Black Sea (Arkhipkin et al., 2014). The Azores and Siberian high pressure and the Asian low pressure areas influence the general atmospheric circulation of the region with prevailing northeastern winds. Northern and eastern winds are predominant only in the southeastern areas of the Black Sea with speeds of 5-6 ms^{-1} (Figure 7), in winter and autumn (Arkhipkin et al., 2014). In summer, southwestern, northern and southeastern winds are dominant in coastal areas and offshore.

In addition, time series of 2 m air temperature above the sea surface, surface net solar radiation (shortwave radiation) and surface net thermal radiation (longwave radiation) were constructed from the 3 hourly ECMWF Era-Interim dataset for 1985-2014 to be input as forcing to NEMO. A strong seasonal cycle exists in thermal forcing parameters (Figure 8). Seasonal climatologies of the forcing data show cooling from the beginning of September to the end of February and the March-August period indicates warming. The October-February period corresponds to the most distinguishing feature of the monthly surface net solar radiation pattern in cooling cycle because of considerable net heat flux variability within the basin (Oguz and Malanotte-Rizzoli, 1996). The climatology of longwave radiation (Figure 8c) shows strong seasonal variability with relatively large and small values in summer and winter, respectively.
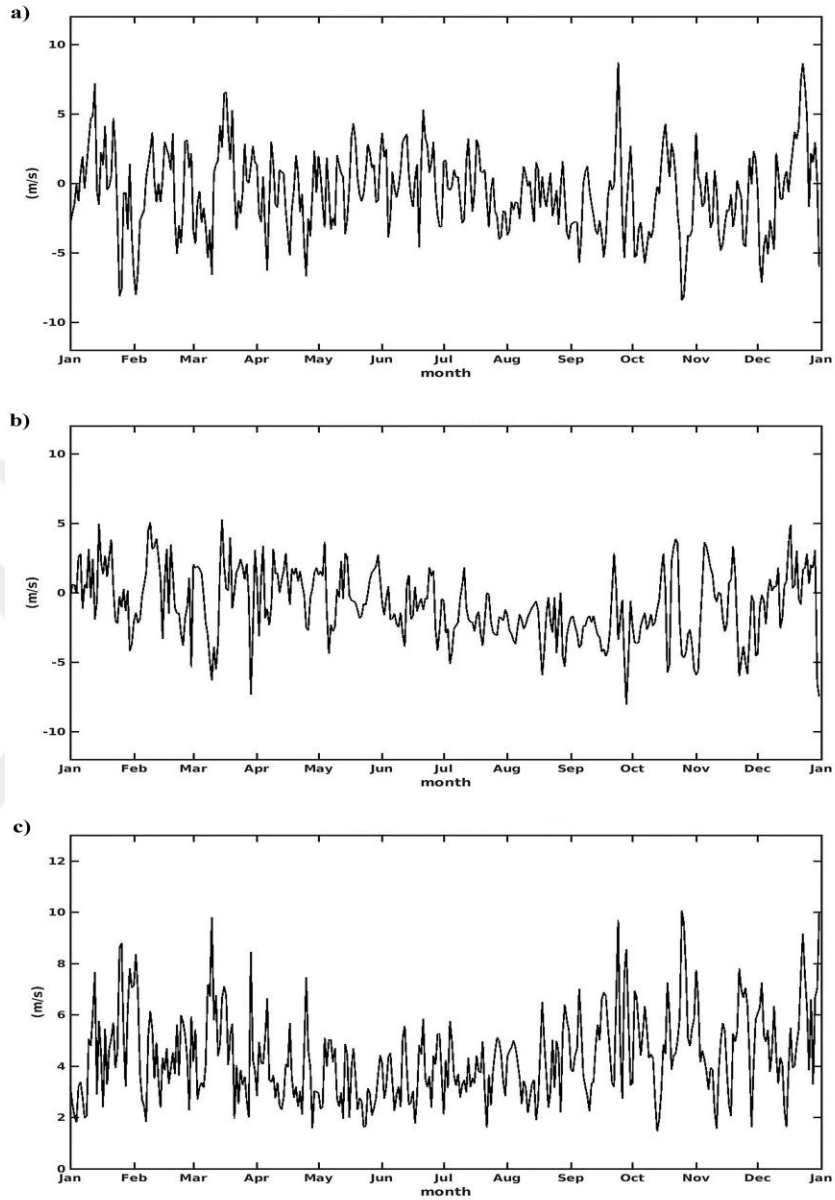
Figure 7: Basin-averaged mean wind speed obtained from ECMWF Era-Interim reanalysis dataset averaged over the time period 1985 – 2014: wind velocity u-component (a), wind velocity v-component (b) and wind speed (c).
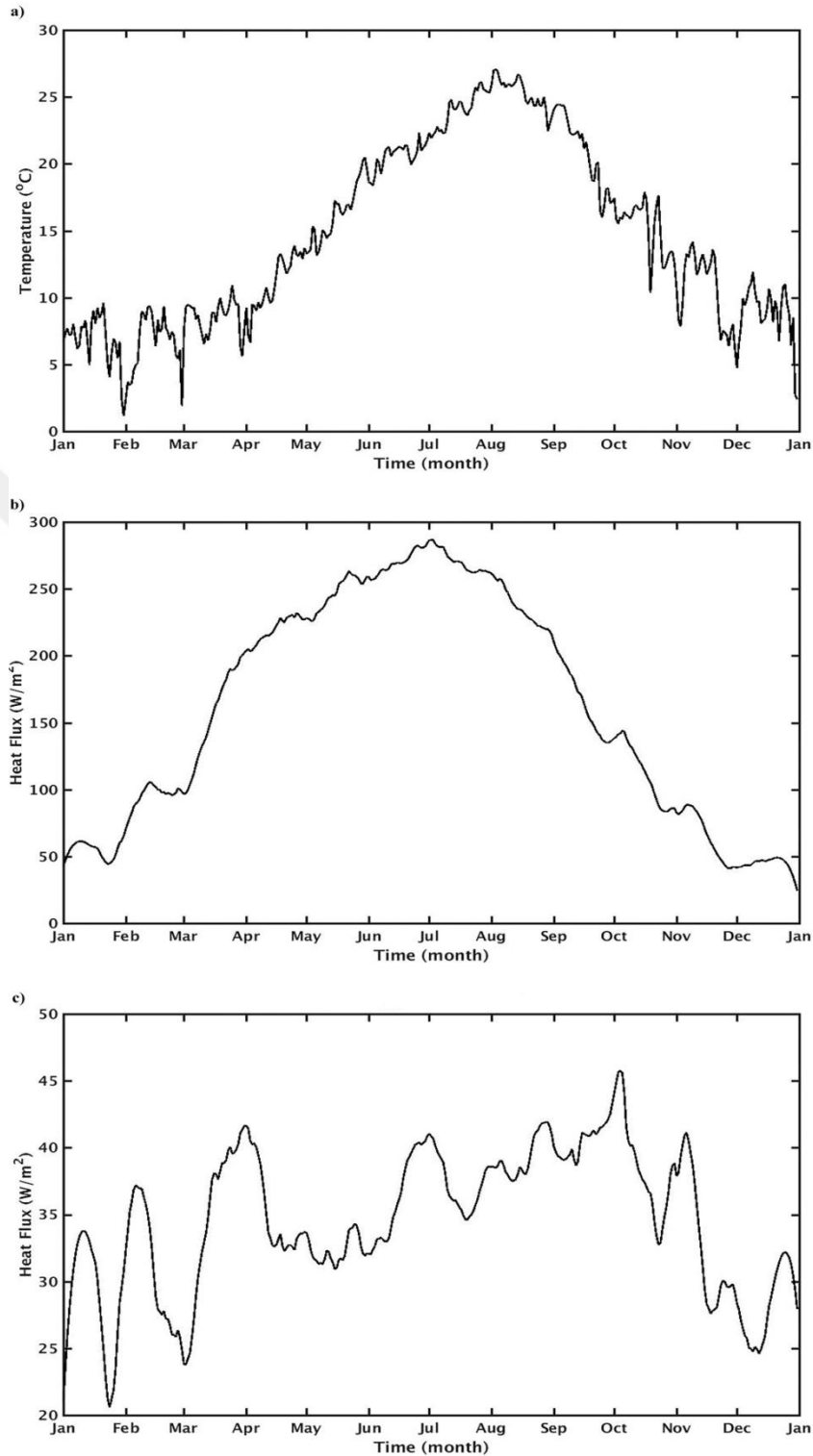
Figure 8: Basin-averaged monthly mean thermal forcing parameters obtained from ECMWF Era-Interim (1985-2014): air temperature at 2 m above the sea surface (a), surface net solar radiation (shortwave radiation) at the sea surface (b) and surface net thermal radiation (longwave radiation) (c).

2.2.6 Precipitation, Evaporation and Specific Humidity

Precipitation changes influence the ocean volume and hence, the ocean heat content. The Black Sea possesses a complex precipitation regime which is influenced by the changes in the atmospheric circulation. Times series of precipitation for the time frame 1985-2014 were also constructed from the Era-Interim data set to force the NEMO model. The seasonal climatology of precipitation (Figure 9) shows that in contrast to spring and summer with lower precipitation, highest amount of precipitation occurs in winter and autumn. Generally, the coastal areas of eastern and southeastern Black Sea possess the highest amount of precipitation which is in agreement with evaporation minus precipitation (E - P) analysis discussed by Oguz and Malanotte-Rizzoli (1996). In the CORE bulk formulae, an inertial dissipative method is used to compute turbulent transfer coefficients of momentum, sensible heat and evaporation from 10 m wind speed, air temperature and specific humidity (Madec, 2015).
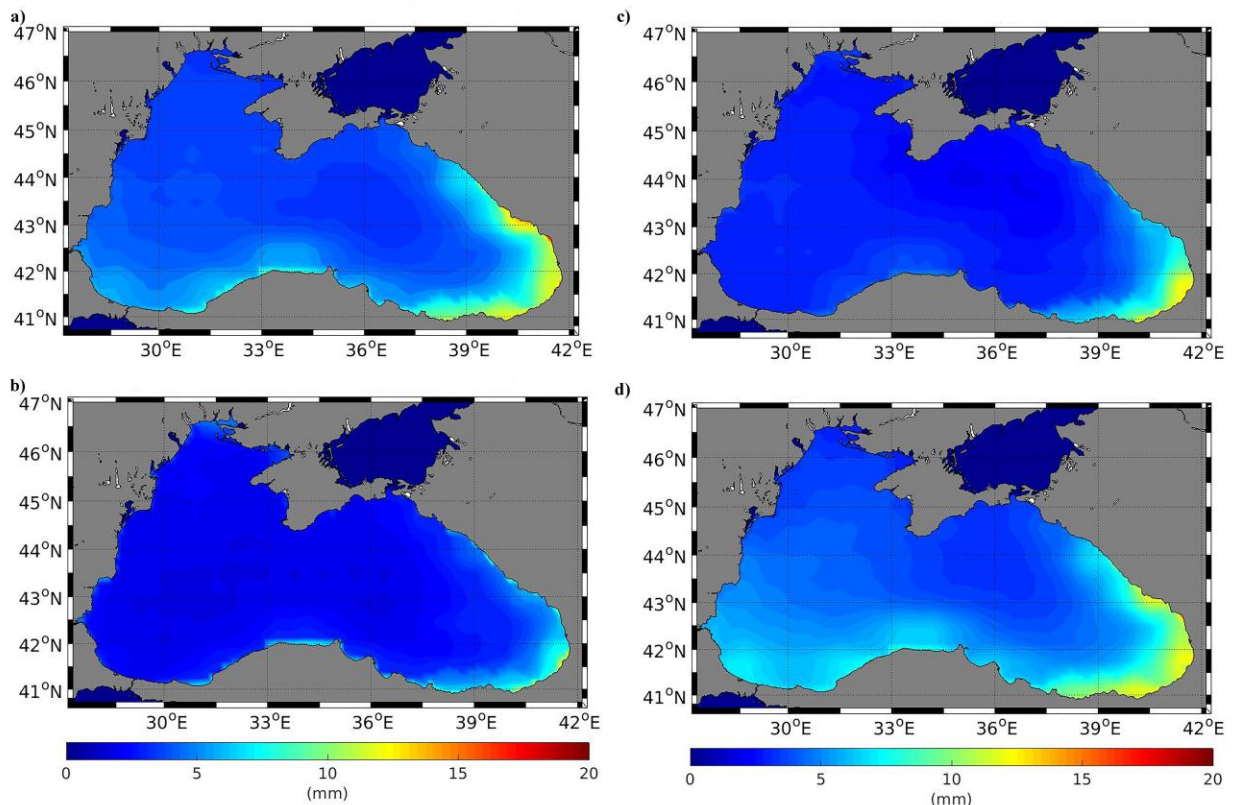
Figure 9: Climatological seasonal mean precipitation (mm) fields over the Black Sea in winter (a), spring (b), summer (c) and autumn (d) calculated from ECMWF Era-Interim (solid and liquid precipitation) dataset (1985-2014).

Along with prognostic sea surface properties, surface wind, air temperature and specific humidity are required to estimate momentum, sensible and latent heat fluxes applying classical bulk formulae. Time series of 2 m dew point temperature and sea level pressure data of ECMWF Era-Interim is used to compute specific humidity. Specific humidity increases along with surface air temperature under fixed relative humidity and hence, local warming increases under the Calusius-Clapeyron equation (Chadwick et al., 2016). Thus, specific humidity (Figure 10) is directly proportional to latent heat flux which directly influences the amount of evaporation. Hence, in bulk formulae specific humidity is used to compute the amount of evaporation and estimate the heat loss.
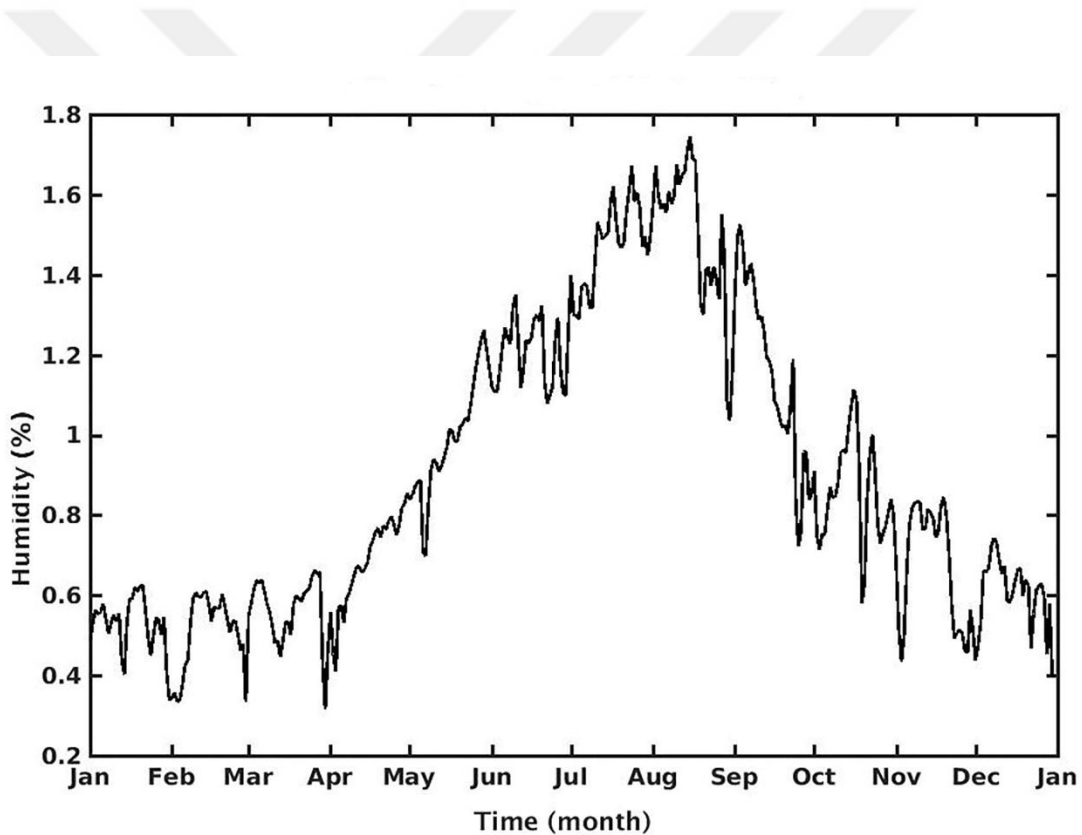
Figure 10: Basin-averaged mean values for specific humidity calculated from ECMWF Era-Interim dataset averaged over the time frame 1985-2014 2 m dew point temperature and surface pressure.

2.2.7 Restoring and Spin Up

One common problem with the model forcing is that the surface heat flux is estimated from various atmospheric reanalysis products (compiled in the ECMWF Era-Interim dataset) with a difference of tens of W/m^2 which eliminates significant climate signals (Carton et al., 2018). In addition, a coarse resolution of atmospheric reanalysis data for regional seas increases the degree of error in computing

ocean physical parameters by ocean general circulation models (OGCMs). This will lead to imprecise computation of ocean physical parameters, specifically sea surface temperature (SST). One way of correcting the model calculated heat flux estimates is by computing heat fluxes from observed values of SST instead of those predicted by the model. Such a technique effectively restores model computed SST to observations. Due to their high temporal and spatial coverage SST data from satellite observations are used (Ortega et al., 2017). To ensure that model computed SST matches observed SST, a flux formulation option defined in the model which adds a corrected heat flux to the surface heat flux (Q_{ns}^0) calculated by the model:

$$Q_{ns} = Q_{ns}^0 + \frac{dQ}{dT}(T_{K=1} - SST_{obs}) \tag{8}$$

is used where Q_{ns}^0 is the model simulated heat flux, Q_{ns} is the corrected surface heat flux, SST_{obs} is the observed (satellite) sea surface temperature field, T is model computed surface layer temperature and $\frac{dQ}{dT}$ is a negative feedback coefficient taken equal to -200 $W/m^2/°K$, which corresponds to a restoring time of 12 days. Restoring SST limits the propagation of the atmospheric forces bias into the upper ocean and hence, enhances correction of heat flux provided by atmospheric model through consideration of observed SST resulting in reproduction of fairly realistic variability of the upper ocean heat content (Iovino et al., 2016). The model spun up for 3 years using the year 1985 repeatedly, after which the model reproduced near surface velocity field including mesoscale processes and adjusted to the initial density field of WOA.

2.2.8 River Discharges

Rivers in the Black Sea model are treated as a "runoff" addition to the precipitation field. River runoff is assumed to enter the sea at surface grid points with a vertical mixing depth of 5 m. Eleven rivers are considered as major rivers to discharge into the Black Sea (Table 2), (Figure 11). Danube, the major European river with the largest upstream area of ~807,000 km² originating from Germany flows to the Black Sea in Romania at the Danube Delta occupying a catchment area of 5,640 km² (Jaoshvili, 2002; Kara et al., 2008). Dniepr with an upstream area of ~463,000 km² and catchment area of ~503,000 km² originates from north Russia is the second largest river discharging into the Black Sea (Jaoshvili, 2002; Kara et al., 2008). Dniestr and Bug (Southern Bug) with catchment area

of ~72,100 km² and 63,700 km², respectively, are the two important trans-boundary rivers flowing to the Black Sea at its northwestern part (Jaoshvili, 2002). In southern Black Sea, Sakarya, Filyos, Kizilirmak and Yesilirmak with a catchment area of ~56,504 km², ~13,156 km², ~78,646 km² and ~36,129 km² are the major rivers influencing the hydrodynamics and ecosystem of the region, respectively (Jaoshvili, 2002). Curuh with catchment area of~22,100 km², and Rioni and Kodori with catchment areas larger than 1,600 km² (Jaoshvili, 2002; Giardino et al., 2015) constitute the most important freshwater discharge into the Black Sea in the eastern coasts. Monthly mean river discharge values in to the Black Sea basin for the 30-year simulation are obtained from Ludwig et al. (2010). Table 3 gives climatological values for the rivers implemented in the model discharged into the Black Sea.

Table 2. List of major rivers discharged into the Black Sea implemented in the hydrodynamic model.

River	Country	Longitude, Latitude	Area(km²)
Dniepr	Ukraine	(32.292°E, 46.542°N)	463,000
Bug (Southern Bug)	Ukraine	(31.958°E, 46.792°N)	63,700
Dniestr	Ukraine	(30.458°E, 46.125°N)	72,100
Danube	Romania	(29.708°E, 45.292°N)	807,000
Sakarya	Turkey	(30.625°E, 41.125°N)	56,504
Filyos	Turkey	(32.042°E, 41.542°N)	13,156
Kizilirmak	Turkey	(35.875°E, 41.708°N)	78,646
Yesilirmak	Turkey	(36.625°E, 41.375°N)	36,129
Curuh	Georgia	(41.625°E, 41.625°N)	22,100
Rioni	Georgia	(41.708°E, 42.208°N)	>1,600
Kodori	Georgia	(41.125°E, 42.875°N)	>1,600

Table 3. Monthly climatological river discharge values (m³s⁻¹) obtained from Ludwig et al., (2009; 2010) and Apeldoorn and Bouwman (2014).

Month	Dniepr	Bug	Dniestr	Danube	Sakarya	Filyos	Kizilirmak	Yesilirmak	Curuh	Rioni	Kodori
Jan.	624.1	22.8	277.1	18171.0	384.4	369.5	277.5	169.4	728.3	2741.3	360.8
Feb.	1.07	2.1	0.0	15550.2	929.6	298.0	894.0	278.7	259.3	1413.7	132.6
Mar.	6663.1	1199.9	2380.0	35447.4	968.3	389.1	1090.8	586.0	427.1	1240.6	108.5
Apr.	15797.9	644.2	1839.0	40482.4	709.3	338.5	2024.7	1253.8	695.6	1024.2	372.4
May	5840.2	344.4	1002.7	32043.1	345.4	244.5	1184.5	1165.5	946.5	588.4	813.0
Jun.	3247.8	196.9	743.8	22646.2	195.5	127.3	560.8	507.1	711.5	475.9	732.7
Jul.	1933.3	115.6	519.5	16664.6	117.5	70.8	328.9	281.9	346.0	350.4	385.0
Aug.	1165.8	69.4	371.3	13280.8	70.9	42.7	198.6	170.2	248.9	338.0	294.4
Sept.	717.6	41.9	315.3	12137.3	42.8	25.8	119.9	102.8	296.6	525.8	323.7
Oct.	667.6	25.3	427.8	14605.1	25.8	15.6	72.47	62.1	488.7	752.8	344.2
Nov.	1094.6	16.6	485.8	17411.8	15.6	84.8	50.4	47.5	557.8	1358.8	216.0
Dec.	422.1	9.5	181.7	14927.0	98.6	193.5	127.9	40.6	490.5	1888.3	236.2
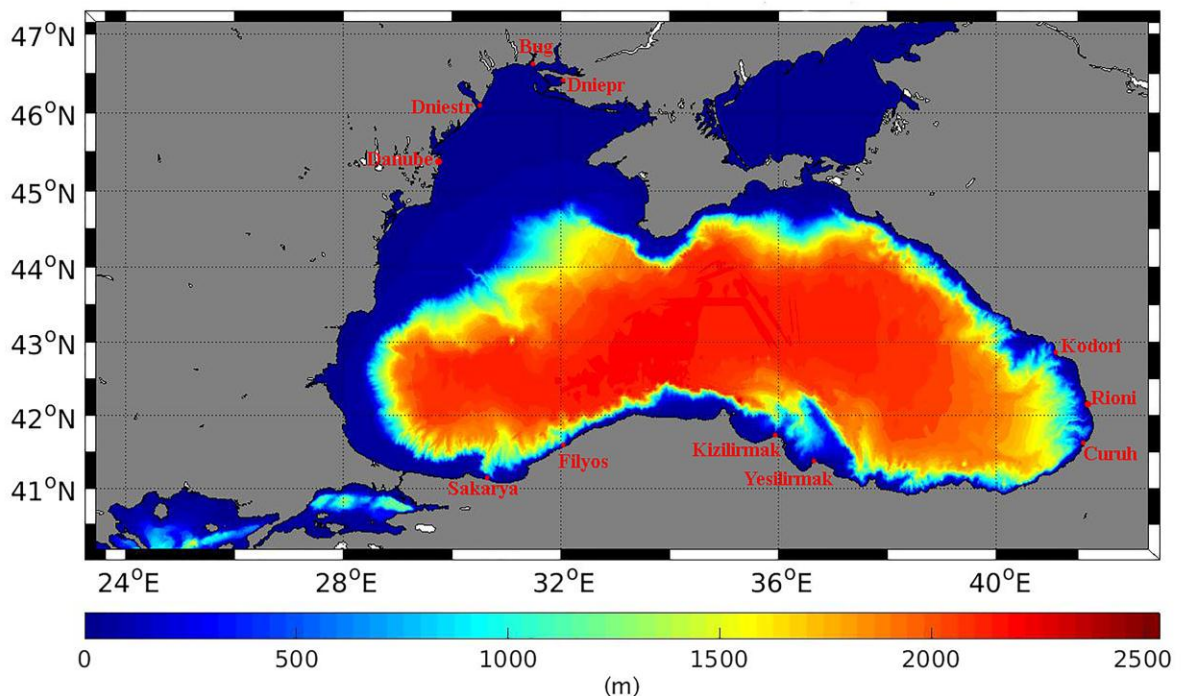
Figure 11: Location of rivers implemented in the hydrodynamic model. Longitude and latitude of the river mouth are approximate longitude and latitude derived from Ludwig et al., (2009; 2010) and Apeldoorn and Bouwman (2014) data.

2.2.9 Unstructured Open Boundary Condition Initialization

The unstructured open boundary condition (BDY) module of NEMO allows easy specification of the open boundaries. It is used for the implementation of Bosporus Strait that allows inflow and outflow of Mediterranean and Black Sea waters into and out of the model domain, respectively. The exchange flow through the Bosphorus is comprised of a two layer flow by brackish flow with a salinity of ~18 psu flowing southward from Black Sea as the upper layer flow and salty water flowing northward to the Black Sea known as the bottom layer with a salinity of ~36 psu. The intrusion of saline Mediterranean water through the Bosphorus below the halocline, drives the interior circulation and mixing (Özsoy and Ünlüata, 1997). To model the two layer flow, a single boundary set (a single grid point) is defined along with a boundary condition. The boundary condition is comprised of a barotropic solution (sea surface height and barotropic velocities), baroclinic velocities and active tracers (salinity and temperature). The width of the Bosporus in the model is 3 km due to the horizontal resolution of the model and the total depth is 70 m, thereby defining the top 40 m for the upper layer and the lower 30 m for the lower layer.

Monthly mean velocity data for the Bosporus upper and lower layers is defined by using a parameterization of Bosporus transport for 30 years from 1985 to 2014 based on Peneva et al., (2001), which calculates the steady state of the two-layer exchange using the theory of Dalziel (1991) and Lane-Serf et al. (1997). With this method the upper layer flux (Q1*) is calculated as:

$$Q_1^* = Q_0 \frac{1 + \sqrt{1 - \left[1 + \left[\frac{H_I}{H-H_I}\right]^3\right]\left[1 - \left[\frac{H_I}{H_C}\right]^3\right]}}{\left[1 + \left[\frac{H_I}{H-H_I}\right]^3\right]} \tag{9}$$

$$Q_2^* = Q_0 - Q_1^* \tag{10}$$

where Q_0 is the freshwater flux in the Black Sea, H is the sea level height of the Black Sea and its anomalies represent Black Sea volume variation (Peneva et al., 2001), and H_I the height of the interface between the two layers which is the height above the sill (Lane-Serff et al., 1997) located at the mouth of the Bosphorus and is calculated as:

$$H_I = \frac{1}{2} H \left[1 - \frac{H_C}{H} \right]^{\frac{3}{2}} \qquad (11)$$

with $H_C = \left[Q_0^2 / g' w^2 \right]^{1/3}$ being the critical height for the sea level over which the exchange between the Black Sea and Marmara Sea becomes two layered (Peneva et al., 2001) and w being the width of the Bosphorus and $g' = 0.03g$ is the reduced gravity acceleration. Sea level needs to rise to H_C approximately 11 m above the sill according to (Lane-Serff et al., 1997) and in the present thesis study calculations it is 13 m to make the character of the sill flow change into a two layer exchange otherwise, it will remain a one layer flow from Black Sea to the Mediterranean (Lane-Serff et al., 1997). Q_1^* is the upper layer outflow from Black Sea and Q_2^* is the lower layer Mediterranean inflow to the Black Sea.

Owing to the fact that the model resolution is 3 km in the horizontal and one grid point has been allocated for the open boundary, calculations have been considered in a way to conserve mean annual in/outflow to/from the Bosphorus as mentioned by Özsoy and Ünlüata (1997) and Oguz et al., (2005) which produces monthly mean values of the flow velocity of both layers as given in Table 4. Özsoy and Ünlüata (1997) and Oguz et al. (2005) highlight that the freshwater excess of 300 km^3 yr^{-1} is balanced by the difference between the transport of the lower layer (inflow) and outflow (upper layer), and hence calculations for annual balance between the inflow and outflow through the Bosphorus in the model satisfies this difference (Figure 12). The salinity and temperature monthly mean climatological data of the Bosporus in- and outflow (Table 5) was calculated from salinity and temperature data obtained from Altiok and Kayisoglu (2015).

Table 4. Monthly mean values of the depth averaged Bosphorus upper and lower layer current velocity in the north-south direction (m/s). Positive values indicate the north direction.

	Upper Layer Velocity	Lower Layer Velocity
Month	Mean current (m/s)	Mean current (m/s)
Jan.	-0.1635	+0.0928
Feb.	-0.2120	+0.1168
Mar.	-0.2127	+0.1201
Apr.	-0.2115	+0.1187
May	-0.2327	+0.1316
Jun.	-0.2238	+0.1266
Jul.	-0.1819	+0.1031
Aug.	-0.1434	+0.0819
Sept.	-0.1162	+0.0664
Oct.	-0.1109	+0.0634
Nov.	-0.1324	+0.0761
Dec.	-0.1371	+0.0783
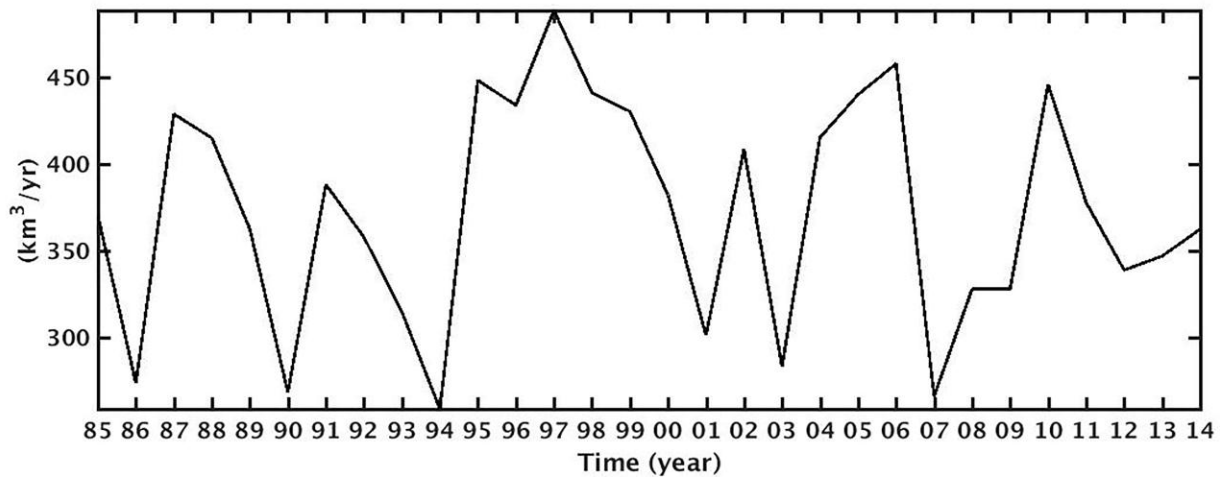
Figure 12: Net outflow through the Bosporus Strait defined as the difference between the transport of the upper (outflow) and lower (inflow) layer.

Table 5. Monthly mean values of the depth averaged Bosporus upper and lower layer salinity and temperature at the Bosporus exit of the Black Sea.

Month	Salinity		Temperature	
	Upper Layer	Lower Layer	Upper Layer	Lower Layer
Jan.	17.84	32.71	7.73	12.74
Feb.	17.77	33.00	6.60	12.72
Mar.	17.77	33.43	7.08	12.73
Apr.	17.64	34.25	8.40	13.70
May	17.64	34.69	11.79	14.31
Jun.	17.90	33.58	14.68	14.01
Jul.	17.68	34.12	16.24	14.20
Aug.	17.99	33.36	19.04	14.39
Sept.	18.16	34.16	18.31	15.15
Oct.	17.81	32.94	17.96	15.69
Nov.	18.05	33.66	13.85	15.08
Dec.	17.73	33.14	10.28	14.45

2.2.10 Tracer Damping – Nudging

The Ocean's vertical structure is conceptually defined as several seawater layers on top of each other with different properties exhibiting different levels of uniformity (Maes and O'Kane, 2014). At the surface the mixed layer is generated as a result of wind buoyancy fluxes through active mixing and energy dissipation. The mixed layer exhibits a uniform vertical structure due to possessing a uniform density profile. Below the mixed layer, stratification occurs leading to the formation of seasonal and permanent pycnocline where vertical density gradients reach its maximum. The reason for the strong pycnocline in the Black Sea is the well-established two-layer density structure (Oguz and Besiktepe, 1999). As the two-layer flow of the Bosphorus plays a big part in this and including realistic Bosphorus dynamics is difficult and limited by available data, it is rather difficult to maintain the permanent pycnocline in a Black Sea model. Below the pycnocline salinity is remarkably constant throughout water column and temperature continues to decrease to the bottom but with a much slower rate and can be considered nearly isothermal, called the deep layer. Accurate simulation of the state of the ocean density field is a major problem in climate and ocean modeling and it is common to observe density drifts (Cummins, 1991). To conserve ocean properties (salinity, temperature and

hence, density) as much as possible a Newtonian damping term is added into temperature and salinity below 207 m with the following equation (12 and13) (Madec, 2015):

$$\frac{\partial T}{\partial t} = \cdots - \frac{1}{\beta}(T - T_0) \qquad (12)$$

$$\frac{\partial S}{\partial t} = \cdots - \frac{1}{\beta}(S - S_0) \qquad (13)$$

where β is the time scale parameter, and T_0 and S_0 are climatology for initial temperature and salinity. Nudging is applied below 207 m (below CIL and consequently, below seasonal and permanent thermocline) in which the β parameter is set to 10 days. No damping is applied within the mixed layer in an effort to provide free evolution of the ocean upper layer.

2.3 Black Sea Model Validation Approach

To validate the model presented in this study, univariate and multivariate metrics are calculated and examined as detailed below. When calculating univariate metrics (section 2.3.1) model output is compared to in-situ data of Black Sea water temperature and salinity obtained through CTD casts, remotely operated gliders and etc. The in-situ data for this comparison are obtained from Black Sea Temperature and salinity observation collection V2 (Black Sea 2015; Simoncelli et al., 2015) provided by the Institute of Marine Sciences, Middle East Technical University. It is publicly available at sextant.ifremer.fr as http://doi.org/10.12770/227e9f7b-ddfc-4004-b0e5-f4785d36d43f. In-situ data coverage changes over 30 years. During 1985-1989 and 1990-1994 the dataset has a good coverage in the NWS, western and northern Black Sea, while in the interior basin and southern Black Sea data coverage is poor. Little data is available from 1995-1999, and that only in northern Black Sea. Almost no data is available from 2000-2004 and 2005-2009. The interior basin is covered in 2010-2014 but there is no data in the NWS. To overcome this data coverage problem, the whole period from 1985 to 2014 is separated into five warming (two: 1993-2000 and 2008-2010) and cooling (three: 1985-1992, 2001-2007 and 2011-2014) periods based on winter SST changes to be better able to compare the model to in situ data.

When calculating multivariate metrics (section 2.3.2) model output is compared to satellite data of SST and sea surface height (SSH) due to the high spatial and temporal coverage of these

datasets. Specifically, the satellite SST data generated at 4 km resolution using advanced very high resolution radiometer (AVHRR) instruments aboard NOAA polar-orbiting satellites going back to 1981 – its Pathfinder version 5.3 AVHRR data available at: http://marine.copernicus.eu/services-portfolio/access-to-products/?option=com_csw&view=details&product_id=SST_BS_SST_L4_REP_OBSERVATIONS_010_022 is used for validation of SST. For the validation of SSH two type of data sets, AVISO and Copernicus. AVISO sea level anomaly (SLA) data provides the period 1985-1992 with a weekly period obtained from NASA at https://podaac-tools.jpl.nasa.gov/drive/files/SeaSurfaceTopography/recon_sea_level/preview/L4/tg_recon_sea_level. SLA data for the period 1993-2014 is provided by the Copernicus Marine Environment Monitoring Service (CMEMS) available at http://marine.copernicus.eu/services-portfolio/access-to-products/?option=com_csw&view=details&product_id=SEALEVEL_BS_PHY_L4_REP_OBSERVATIONS_008_042. Satellite SSH data is calculated by adding satellite SLA and mean dynamic topography (MDT). MDT data for the Black Sea is coarse (19.8 km × 14 km) and interpolated to satellite grid points to calculate satellite SSH. The sum of SLA and ADT then gives satellite SSH. For the 1985-1992 period a temporal interpolation is performed to estimate daily SSH from weekly satellite SSH data. Spatial interpolation of MDT, temporal interpolation of SSH, and SLA contaminated by land and complex coastal topography results in less accurate and sparse measurements near the coast. These are the main challenges with SSH data leading to a deviation of model computed SSH from satellite SSH.

2.3.1 Univariate Metrics

To assess the skill of the model in reproducing the actual state of the Black Sea, various univariate methods are used. Simple quantitative metrics such as mean absolute error (*MAE*), mean bias error (*MBE*), Nash Sutcliffe model efficiency (*NSME*), percentage model bias (P_{bias}), root mean square deviation (*RMSD*), correlation coefficient (*r*) and standard deviation (*STD*) are used to evaluate model performance (Stow et al., 2009).

MAE is the most common measure of continuous variables' accuracy. *MAE* measures the average magnitude of the error without considering its direction:

$$MAE = \frac{1}{n}\sum_{i=1}^{n}|M_i - D_i| \tag{14}$$

where M is model computed variable values, D is observation data, and n is the number of samples to be compared.

MBE indicates the average model bias and it represents the systematic error of model for under- or overestimation of the intended variable and is defined as:

$$MBE = \frac{1}{n}\sum_{i=1}^{n}M_i - D_i \tag{15}$$

where M is model computed variable values and D is observation data. In general, *MBE* captures the average bias of the model.

NSME or model efficiency of a model variable is a measure of the ratio of the model error to the variability of the data and is a metric to investigate how well the model measures tracers (temperature and salinity) relative to the average of the observations. It is given by:

$$ME = 1 - \frac{\sum_{n=1}^{N}(D_n - M_n)^2}{\sum_{n=1}^{N}(D_n - \overline{D})} \tag{16}$$

where, D is observational data, M is corresponding model output and the overbar indicates the mean of dataset for the chosen variable. The following values for ME should be considered:

$ME > 0.65$ excellent,

$0.5 < ME < 0.65$ very good,

$0.2 < ME < 0.5$ good,

$ME < 0.2$ poor match.

$ME \cong 1.0$ indicates a very close match between observational data and model values.

To understand whether the model is systematically underestimating or overestimating the observation data, the percentage model bias (P_{bias}) is used. This metric is defined as:

$$P_{bias} = \frac{\sum_{n=1}^{N}(D_n - M_n)}{\sum_{n=1}^{N} D_n} \times 100 \qquad (17)$$

where the following values for P_{bias} are of importance:

$|P_{bias}| < 10$: excellent,

$20 < |P_{bias}| < 10$: very good,

$20 < |P_{bias}| < 40$: good, and

$|P_{bias}| > 40$: refers to as poor accuracy of model simulation.

The optimal value of P_{bias} is 0.0, with low-magnitude values indicating accurate model simulation.

RMSD, *r* and *STD* are further measures used as univariate metrics to evaluate model performance. These three metrics are often presented in the form of Taylor diagram for a better overview. A Taylor diagram is a tool which provides a graphically summary of the match between model and observation. The similarity between two data sets in terms of their *r*, *RMSD* and *STD* Taylor diagrams are useful in evaluating multiple aspects of complex models. *RMSD*, *r* and *STD* are defined as:

$$RMSD = \sqrt{\frac{1}{N}\sum_{i=1}^{N}(D_i - M_i)^2} \qquad (18)$$

RMSD provides a useful measure of the goodness of fit between model (*M*) and data (*D*). The closer the *RMSD* to zero the better the fit. It is a measure for the difference between values computed by the model and the values observed.

Correlation coefficient r gives the strength of the relationship between model and data values. The values for r range between -1.0 and +1.0. A correlation of -1.0 shows a perfect negative correlation, while a correlation of +1.0 shows a perfect positive correlation and a correlation of 0.0 means no relationship between the two data sets. r is calculated as:

$$r = \frac{\sum_{i=1}^{N}(M_i - \bar{M})(D_i - \bar{D})}{\sqrt{\sum_{i=1}^{N}(M_i - \bar{M})^2}\sqrt{\sum_{i=1}^{N}(D_i - \bar{D})^2}} \tag{19}$$

STD quantifies the amount of variation of a set of data values. A low STD indicates that the data points tend to be close to the mean of the data set and a high STD shows that the data points are spread out over a wider range of values and is defined as:

$$STD = \sqrt{\frac{\sum_{i=1}^{N}(x_i - \bar{x})^2}{N-1}} \tag{20}$$

where x_i is the value of the ith data point (model or data), $\bar{x}$ is the mean value of the dataset and N is the number of data points in the data set.

2.3.2 Multivariate Metrics – Quantile Analysis

Multivariate approaches such as quantile analysis and empirical orthogonal function (EOF) analyses that are capable of examining spatial and temporal variability of models play a major role in the assessment of model skill. These approaches enable comprehensive evaluation of complex relationships existing between observations and model data.

Quantile analysis technique calculates the model skill score over a range of spatial scales for SST and SSH. The match of two-dimensional representations of model and satellite SST/SSH data at distinct spatial scales through wavelet decomposition is evaluated using the two-dimensional binary difference maps (Casati et al., 2004; Shutler et al., 2011). The result of the two input datasets

(model and satellite SST/SSH) difference is achieved in the form of binary maps. The steps of this process for a particular threshold are as follows:

1. Binary fields' computation for the two input datasets. For a given threshold t and a data field D, the binary image I is defined as:

$$\begin{cases} I = 1, & D \geq t \\ I = 0, & D < t \end{cases} \tag{21}$$

2. The binary difference map computation: subtraction of the corresponding binary fields ($z = I_Y - I_X$), where X and Y refer to model and data, respectively.

3. 2-D Haar wavelet decomposition performance on the binary difference map. A weight image ξ_0 defined as:

$$\xi_0 = \begin{cases} 1, & for\ valid\ data \\ 0, & for\ missing\ data \end{cases} \tag{22}$$

is introduced into the wavelet decomposition which is used to reduce the impact of heavily occluded areas on the difference metrics. The Haar wavelet decomposition is performed by spatially averaging over a $2^l \times 2^l$ pixel region, where l is the level of decomposition.

4. The mean square error and skill score computation for each level of decomposition.

A Skill Score (SS) is calculated as a function of mean square error (MSE) as:

$$SS = 1 - \frac{MSE}{2\varepsilon(1 - \varepsilon)} \tag{23}$$

where ε is the fraction of data contained in each quantile. Skill Score ranges from 0 to 1, with 1 corresponding to a perfect fit. A more comprehensive description of method can be found in Picart et al., (2012).

2.3.3 Multivariate Metrics – EOF Analysis

To study possible patterns of climate variability and how these patterns change with time EOF (empirical orthogonal function) analysis is often used. The EOF analysis enables visualization of all complicated variability in a data set. The data is partitioned into mathematically orthogonal (independent) modes interpreted as oceanographic modes. The EOFs are derived by computing the eigenvectors of a spatially weighted anomaly covariance matrix, and the corresponding eigenvalues. The eigenvalues imply a measure of the percent variance explained by each mode.

$$z(x,y,t) = \sum_{k=1}^{N} PC(t)EOF(x,y) \qquad (24)$$

where $z(x,y,t)$ is the original time series (data set) as a function of time t and space (x,y). $EOF(x,y)$ shows the spatial structures (x,y) of the major factors that can account for the temporal variations of z and $PC(t)$ is the principal component that tells how the amplitude of each EOF varies with time.

EOF analysis is actually re-expressing the original data set in terms of a variance basis. The EOF method finds both time series and spatial patterns and has been extensively used to examine variability of scalar fields such as SST, sea level pressure (SLP), etc. Each EOF mode is an eigenvector associated with the biggest eigenvalue and the one associated with the second biggest eigenvalue is the second mode. Since the first few EOF modes explain the most variance and are scientifically meaningful, they are often of concern. Spatial mode representation of EOF modes shows their relation to the geographical features. Temporal mode of EOFs introduces amplitude of variability in the data set (e.g. warming/cooling periods for SST data).

In this study the Data Interpolating Empirical Orthogonal Functions (DINEOF) tool is used to perform EOF analysis (Alvera Azcarate et al., 2009). DINEOF calculates spatial and temporal EOF modes and their variances and has been applied to the SST, chlorophyll and wind satellite fields (Alvera Azcarate et al., 2011). It is also a technique for reconstruction of missing data based on EOFs in geophysical fields (Alvera Azcarate et al., 2009). DINEOF uses EOFs to infer the missing data through singular value decomposition (SVD) representation of the data defined as in equation (22) (Beckers et al., 2006). The SVD decomposition is then truncated into the first EOF mode. The first spatial mode is multiplied by the first temporal mode and SVD is applied again until convergence is

reached. DINEOF is available at http://modb.oce.ulg.ac.be/mediawiki/index.php/DINEO (Alvera Azcarate et al., 2011).

2.4 Eddy Statistics Analysis

Statistical analysis of the ocean eddies is a major part of mesoscale ocean eddy studies which requires accurate, automated and scalable eddy detection algorithm. To identify closed contour SSH features an iterative-thresholding approach is used. Features are filtered based on their minimum eddy size of 9 pixels (27 km), maximum eddy size of 1000 pixels (3000 km), and minimum amplitude of 1 cm. The connected component contains at least one minimum or maximum and the connected component has a predefined convex hull ratio as a function of the latitude of the eddy (Faghmous et al., 2012). If the feature contains these criteria it is determined that the feature is an eddy. EddyScan's open-source implementation in MATLAB is available at https://github.com/jfaghm/ClimateCode.git.

2.5 Kinetic Energy Analysis

The energy of the total surface geostrophic flow is represented by the total kinetic energy (TKE) (Juza et al., 2016). The mean kinetic energy (MKE) is the energy induced by the mean current and is used to describe the basin-scale variability on different time scales (Juza et al., 2016; Kubryakov et al., 2016). Eddy kinetic energy (EKE) is used to describe mesoscale variability and provides identification of regions with high variability such as meanders, fronts and eddies (Menna and Poulain, 2013; Juza et al., 2016). To quantify these kinetic energy levels of the simulated circulation, TKE, MKE and EKE are calculated. To calculate energy metrics, the velocity field (u, v, w) is split into a time independent component (U, V, W) and a time dependent component $(\acute{u}, \acute{v}, \acute{w})$ (Sorgente et al., 2011) defined as:

$$
\begin{aligned}
u &= U + \acute{u}, \\
v &= V + \acute{v}, \\
w &= W + \acute{w}.
\end{aligned}
\tag{25}
$$

where the temporal averaging over a given interval m (annual or monthly) gives the time independent part (Sorgente et al., 2011) as:

39

$$U = \frac{1}{m}\sum_{i=1}^{m} u_i,$$

$$V = \frac{1}{m}\sum_{i=1}^{m} v_i, \tag{26}$$

$$W = \frac{1}{m}\sum_{i=1}^{m} w_i.$$

Hence, the TKE is expressed as:

$$TKE = \frac{1}{2}(u^2 + v^2), \tag{27}$$

and MKE is obtained from:

$$MKE = \frac{1}{2}(U^2 + V^2). \tag{28}$$

and EKE is calculated as:

$$MKE = \frac{1}{2}(ú^2 + ´v^2). \tag{29}$$

2.6 Ekman Pumping Velocity

Coastal divergence, as a result of offshore Ekman transport due to the wind stress curl leads to Ekman pumping or upwelling. It is believed that two mechanisms control basin scale circulation of the Black Sea; wind forcing that is driving the Rim Current and Ekman pumping, which results in transport of nutrients through upwelling. Ekman pumping can lead to nutrient enrichment of the euphotic layer and the occurrence of winter phytoplankton blooms. To investigate the role of this mechanism Ekman pumping velocity is calculated using wind stress as:

$$W = \frac{1}{\rho \times f}\nabla \times \tau. \tag{30}$$

where ρ is seawater density, f is the Coriolis parameter and τ is the wind stress,.

CHAPTER 3

MODEL VALIDATION

In this chapter an extensive model-data comparison is presented and the ability of the model to conserve the pycnocline structure during the 30 year (1985-2014) model run is examined. Sea surface temperature (SST), sea surface height (SSH), water column temperature and salinity are compared with the available satellite and in-situ data, for 30-year model run period, 1985-2014, respectively.

3.1 Model - Data comparison

To begin this section on model-data comparison the evolution of basin-averaged density, salinity, and temperature profiles with depth (Figure 13) from initial conditions provided to the model from WOA (red line) over the 30 year model run is examined. Drifts from the initial conditions prescribed are always present in models as a result of intrinsic model errors. Here, the initial condition applied for the 30-year simulation is obtained from January mean of the Decadal Monthly Mean Climatology (1955-2012) data set from the World Ocean Atlas 2013 (Locarnini et al., 2013; Zweng et al., 2013) (see Figure 6) and hence drifts from the actual initial condition (density, temperature and salinity) are expected. The evolution of density profiles (Figure 13a) shows that after 30 years the mean drift from initial conditions density in the mixed layer is 0.0748 (kg/m^3) and in the intermediate layer it reaches 0.2455 (kg/m^3) and in the deep layer it is 0.0113 (kg/m^3). However, the fact that density profiles deviate over time and then drift back towards the initial conditions indicate conservation of density after 30 year model run. Salinity profiles (Figure 13b) reveal that the basin-averaged salinity distribution is captured well by the model and even though salinity in the surface layer increases by 0.2 at the end of 1989, it decreases similarly strong by the end of 1994 and maintains the salinity until 1999. It can be seen that the density profile follows salinity changes despite large annual variations in sea temperature. However, large variations in temperature (Figure 13c) elucidates that model is able to reproduce cooling/warming periods and while at the same time through the water budget balance (precipitation + river + Bosphorus inflow = evaporation + Bosphorus outflow) salinity is conserved. Considering the fact that below 207 m depth tracer nudging (temperature and salinity) −as explained in 2.2.10- is applied to maintain pycnoline below CIL, density changes follow salinity variations leading to conservation of density throughout water column. This way it is ensured that the model is capable of maintaining the pycnocline while at the same time is able to simulate

seasonal and interannual changes in the upper vertical structure of the Black Sea including related physical and hydrodynamic properties.
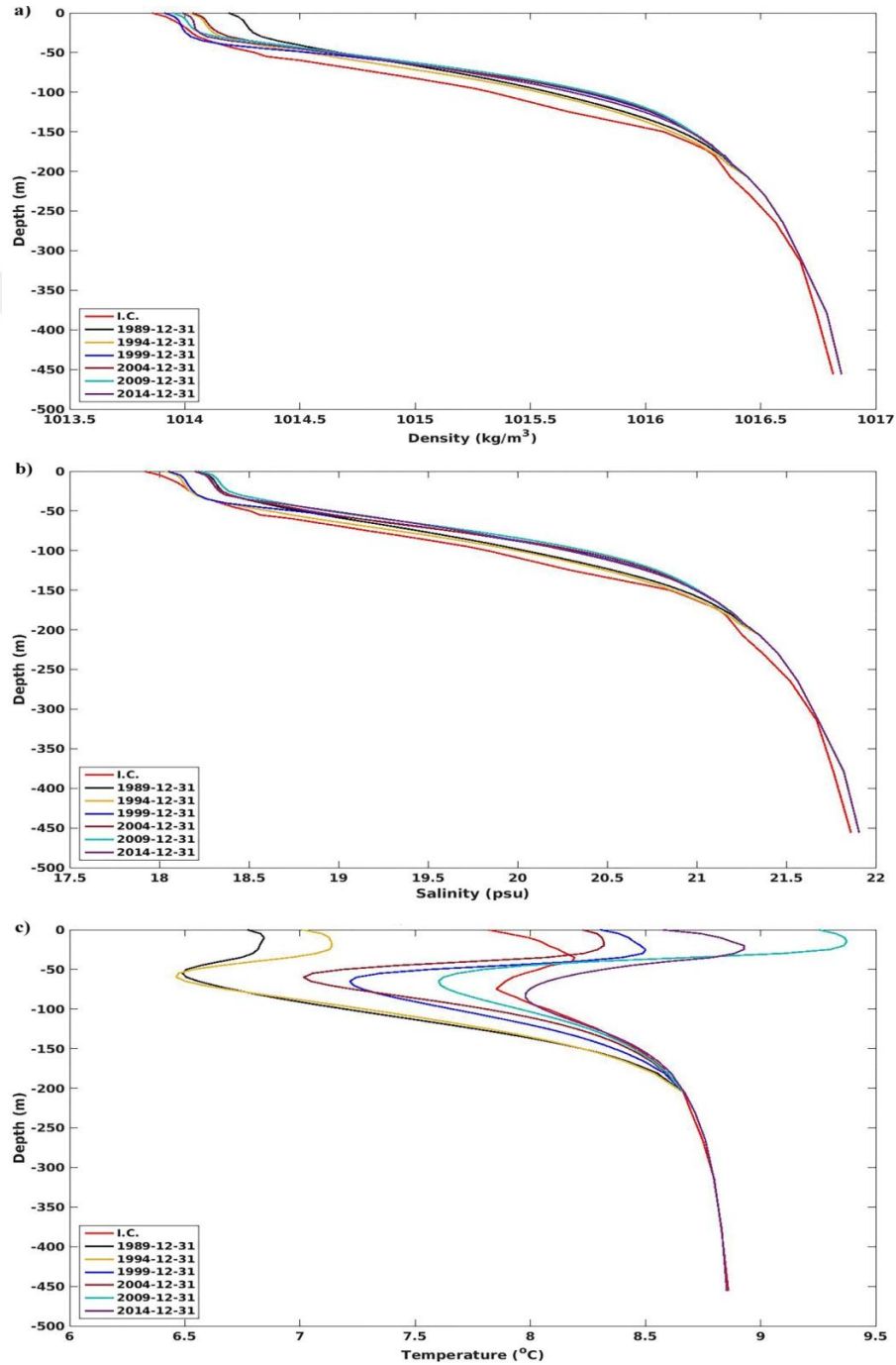
Figure 13: Basin-averaged density (a), salinity (b) and temperature (c) profiles depicting variations from the WOA 2013 data (Locamini et al., 2013; Zweng et al., 2013) used as initial conditions (I.C.) on 01 January 1985 until 31 December 2014 in five year intervals to evaluate pycnocline stability during 30 year simulation (model run).

3.1.1 Sea Surface Temperature Model - Satellite Comparison

Model (red line) and satellite (blue line) SST comparison (Figure 14a) shows that model SST variations are nearly identical to satellite measured SST. The reason for such a high accuracy in model produced SST is SST restoring described in 2.2.7. Restoring SST enables model to reduce atmospheric forcing heat flux error due to coarse resolution of ECMWF Era-Interim reanalysis data (resolution of 79 km interpolated to a 14 km grid points by provider). For a more detailed investigation of model and satellite SST difference, Figure 14b shows how model SST deviates from satellite measured SST. Mean satellite model SST difference ($\overline{SST_{sat} - SST_{model}}$) is 1.3272 °C showing that model underestimates SST overall. One important and most possible reason for this difference may be the factor used for evaporation (rn_efac = 0.35) which is applied to calculate evaporation in the model. It results in the amount of latent heat calculated by model itself in the CORE bulk formulae, and the small evaporation factor chosen to conserve density changes in the mixed and intermediate layers may lead to an underestimation of model SST. Mean annual sea surface temperature spatial distribution (1985-2014) for the entire basin shows (Figure 15a) SST increase in northwest to southeast direction which follows mean annual satellite SST distribution (Figure 15b) indicating model's capability in representing long term SST distribution. Mean model climatology bias compared to satellite SST climatology (Figure 15c) is -1.27 representing underestimation of model which is close to the mean basin averaged SST difference mentioned in the above.
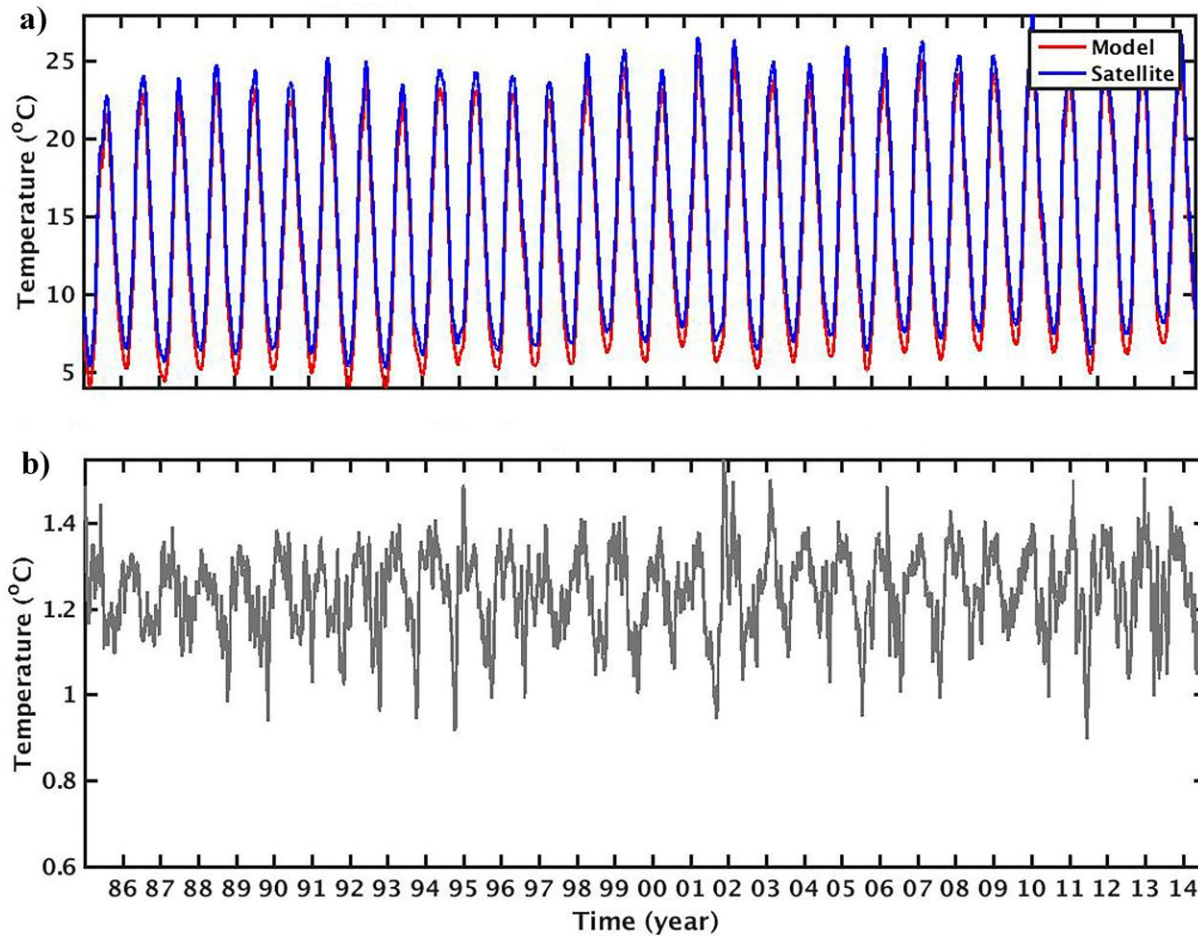
Figure 14: Model (red line) and satellite (blue line) basin averaged sea surface temperature (SST) comparison (a). Deviation of model computed SST from satellite measured SST values (b), (1985 - 2014).
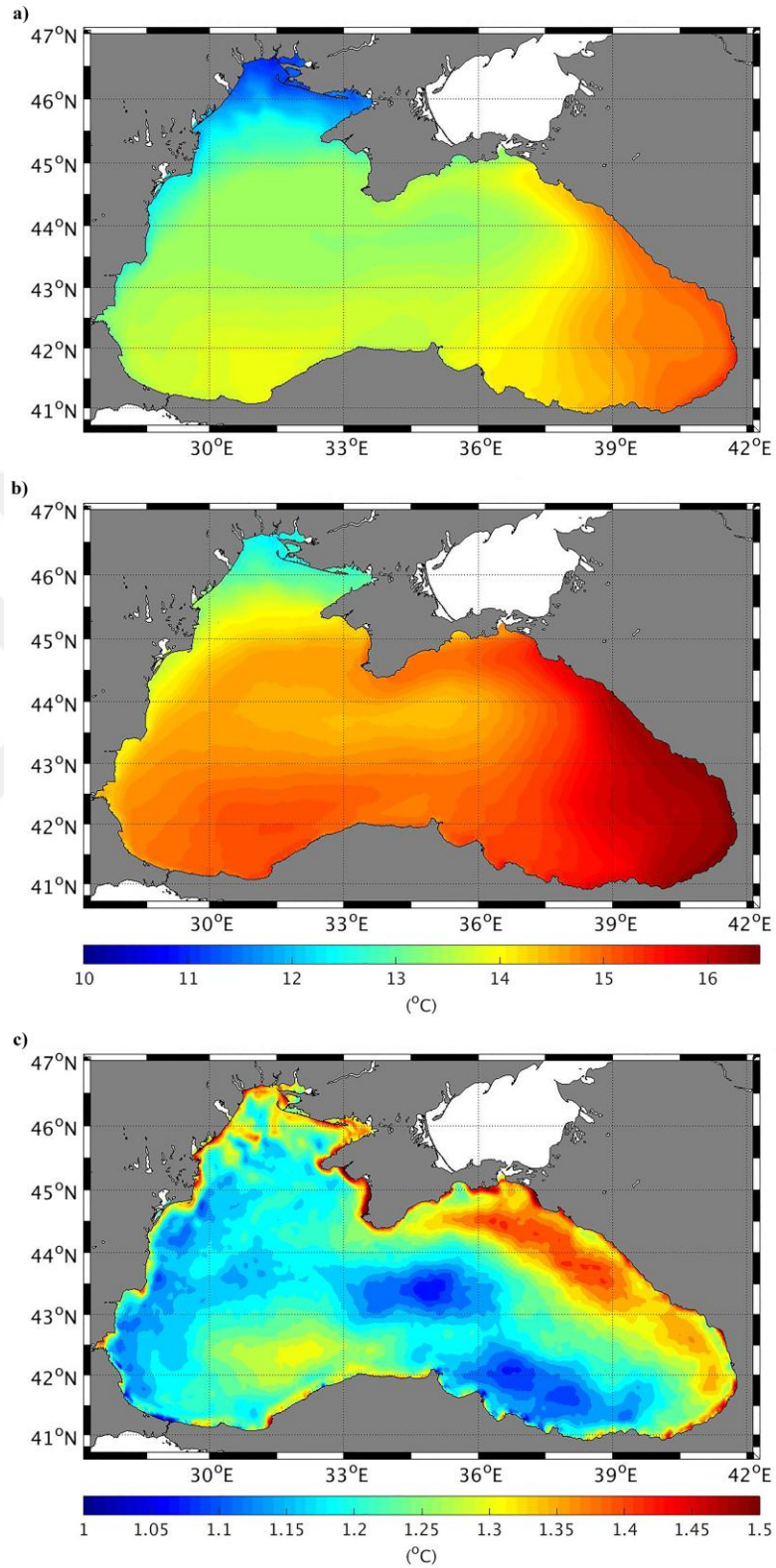
Figure 15: Annual mean model (a) and satellite measured (b) sea surface temperature (SST) distribution (1985-2014). Mean satellite measured and model computed SST difference (c), (1985 - 2014).

3.1.2 Water Column Temperature, Salinity and Density Changes and Mixed Layer Depth

Reproduction of the Black Sea water column structure through modeling is of paramount importance. As a result of periodic cooling/warming of surface waters during winter/summer, subsurface water temperature changes and leads to the formation/disappearance of distinct subsurface water masses and MLD variation. The most well-known subsurface water mass in the Black Sea is the Cold Intermediate Water/Layer (CIW/CIL) identified by temperatures less than 8 °C with its vertical extension limited to the upper 100 m (Oguz et al., 1993; Özsoy and Ünlüata, 1997), corresponding typically to ~15.4 kg m^3 (Akpinar et al., 2017). To evaluate model efficiency in producing vertical structures (temperature, salinity and density distribution, CIL depth and formation and MLD) of the Black Sea a grid point in the center of the basin (Figure 1) is chosen for evaluation of temperature and salinity (Figure 16). During winter, cold and dense water is formed and summer thermal stratification is broken down resulting in the formation of a mixed layer above the halocline (Capet et al., 2014). The time series plot of model temperature (Figure 16a) reveals that the model reproduces temporal temperature variations in water column and CIW formation in winter with temperatures less than 8°C leading to formation of CIL between depths of 18.7 m and 134.5m (Figure 16a) which agrees with findings of Akpinar et al., (2017) measured using Argo floats data and Stanev et al., (2018).

The minimum temperature value computed for bottom boundary of the CIL is 5.9737°C. Extension of CIL to 85 m is equivalent to corresponding density of 15.3 kg/m^3, which is in agreement with 15.4 kg/m^3 isopycnal conventionally used for identification of the CIL (Akpinar et al., 2017). Deep replenishment of CIL down to 100 m in 2010 found by Akpinar et al., (2017) is captured by the model indicating the model is capable of simulating the cold water mass formation in the Black Sea.
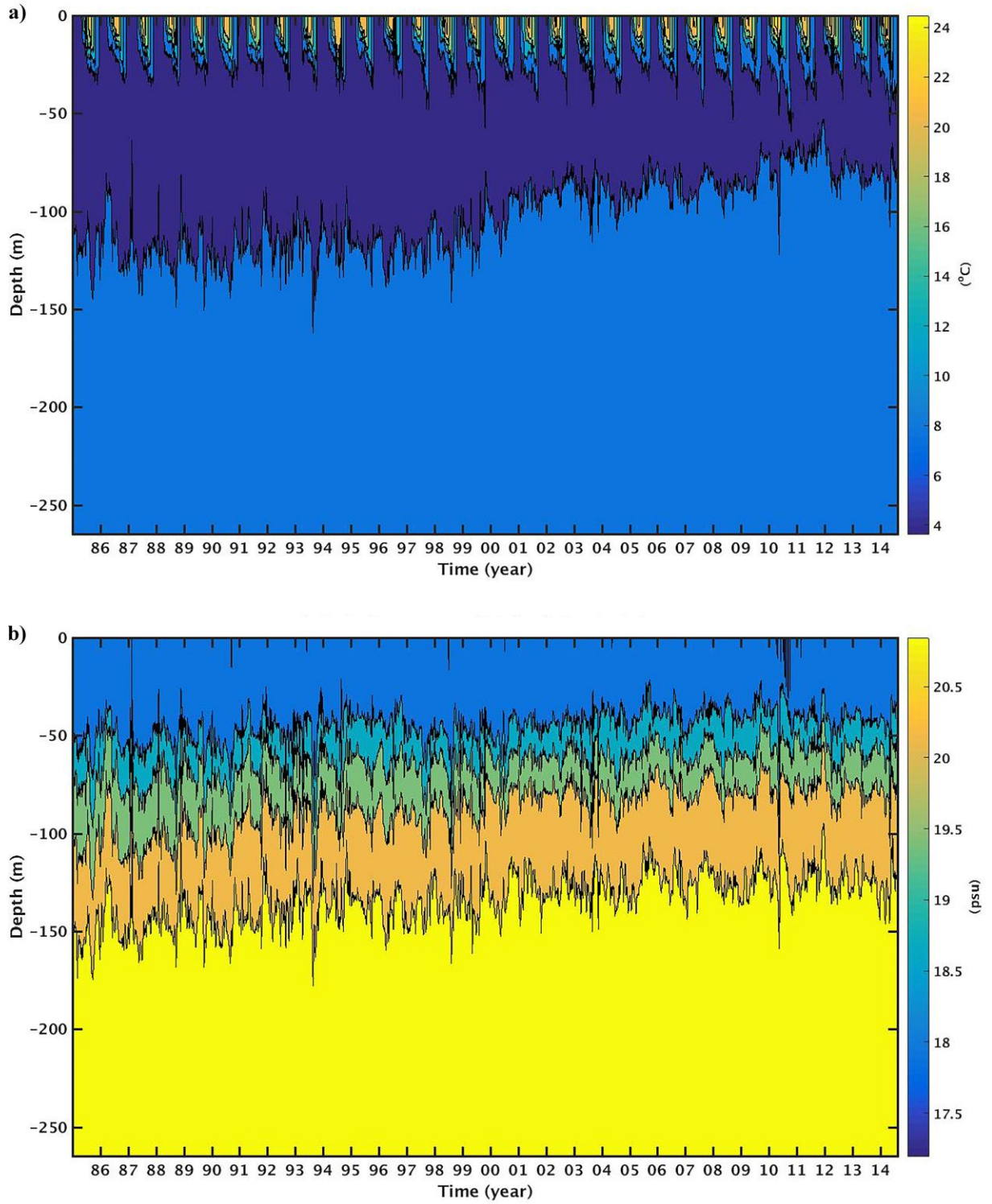
Figure 16: Contour plots of temperature (a) and salinity distribution (b) variations at a grid circle in the center of the Black Sea (White point in Figure 1), (1985 - 2014).

Model simulations show that salinity (Figure 16b) increases smoothly with depth from a surface value of 18.26 psu to 22.32 psu at the bottom of the basin. An abundant supply of fresh water through rivers flowing into the Black Sea makes the upper layers less dense than the underlying saltier layers resulting in strong stratification. The stratified water column weakens during winter as a result of prevailing strong winds presence and mixing occurs in upper layers. Maximum daily basin averaged mixed layer depth of model simulations is 41.51 m in February 2008 and the minimum is 9.62 m in June 1993) (Figure 17). These values are in agreement with findings of Capet et al., (2014) with a minimum depth of <10 m and a maximum value of about 40 m over the period of 1955-2011.

3.1.3: Sea Surface Height Model - Data Comparison

To evaluate model performance in reproducing Sea Surface Height (SSH), basin averaged sea surface height is compared to satellite measured SSH calculated from satellite sea level anomaly (SLA). Generally, model produced basin averaged SSH is slightly different than satellite SSH (Figure 18a) which is expected considering the high spatial variability over the basin with a mean overestimation of model by 0.14 m (Figure 18). Mean satellite SSH is +0.029 m while model calculated mean SSH is +0.176 m. Root mean square deviation as an indicator of differences between model predicted values and satellite measured SSH is 0.075 m meaning that the magnitude of model error is about 7.5 cm. Correlation coefficient between model produced SSH and satellite measured SSH is 0.57 which is satisfactory for calculation of SSH. Since SLA data for the period of 1985-1992 as mentioned in 2.3 is obtained in the form of weekly data and model SSH is required to be compared to satellite data in daily format, temporal interpolation is applied to satellite data in the interval 1985—1992. This has led to imprecise daily satellite SSH data and results in large differences between model and satellite SSH before 1993 (Figure 18a). A more detailed analysis of the performance of the model in respect to the SSH will be presented in Chapter 3 where EOF analysis is performed on both model output and satellite data that reveals temporal and also spatial differences.
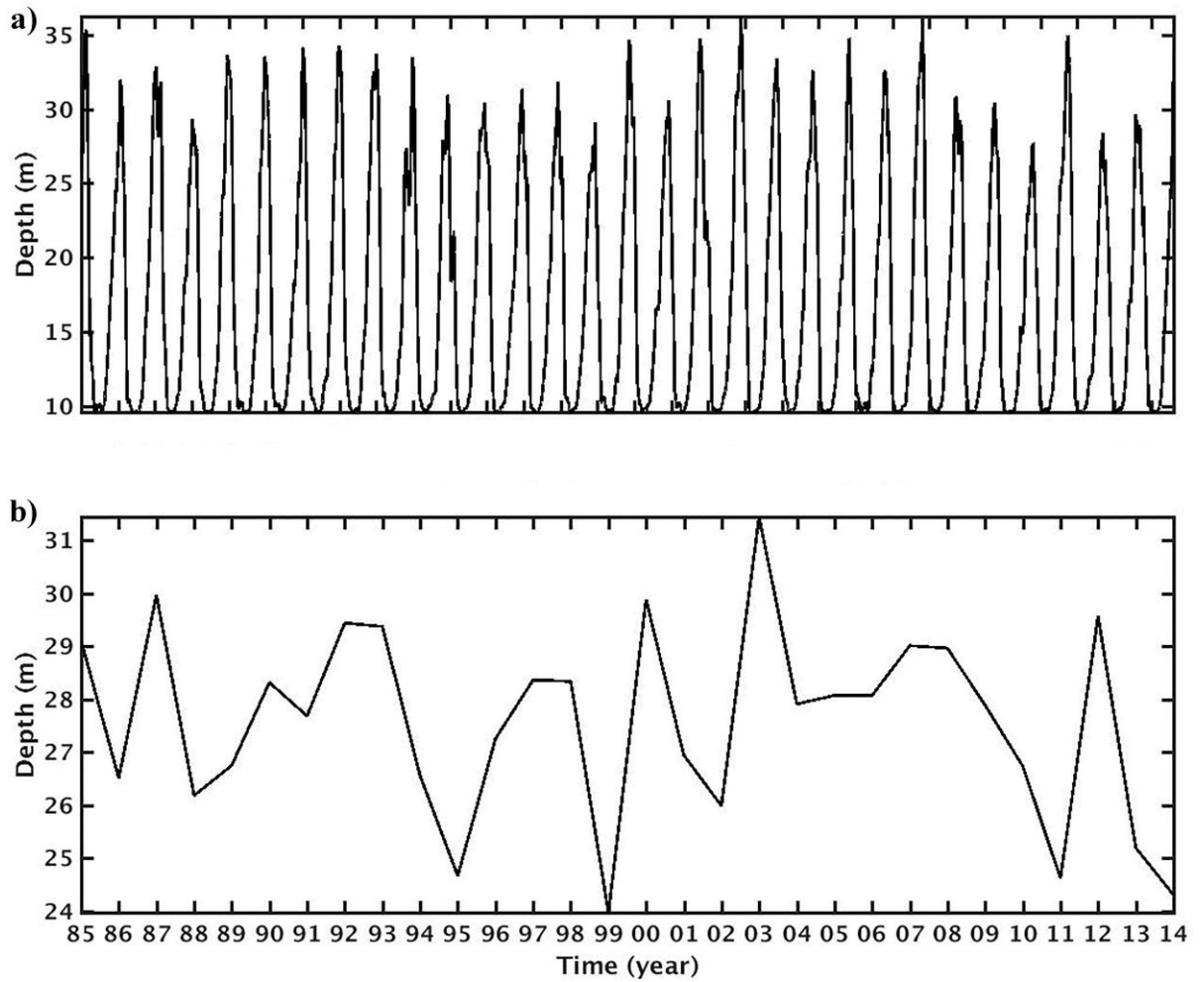
Figure 17: Daily basin averaged mixed layer depth (a) and winter (January-March) basin averaged mixed layer depth (b) from 1985 to 2014.

49
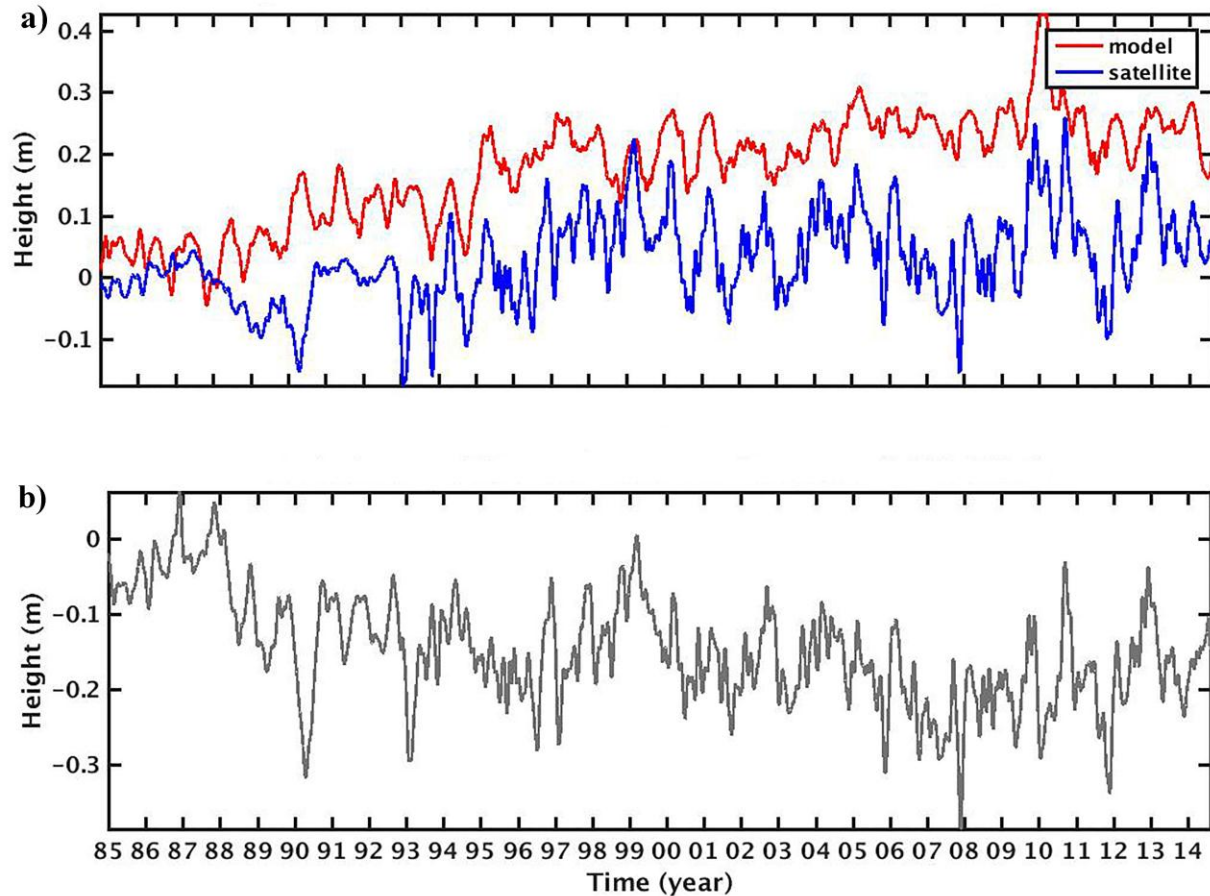
Figure 18: Model (red line) and satellite (blue line) basin averaged sea surface height (a) and basin averaged satellite model SSH difference (b) (1985-2014).

3.1.4: Sea Surface Circulation

Surface circulation system of the Black Sea in all observational and modeling studies possesses a permanent upper layer feature, the Rim Current, with an average current speed of up to approximately 40 cm/s and higher based on limited observations (Oguz et al., 1993; Kara et al., 2005). The fact that the choice of the atmospheric forcing largely influences sea surface circulation features' simulation of the Black Sea (Kara et al., 2005) reveals the importance of atmospheric forcing to achieve an accurate and realistic circulation features. The simulated mean upper layer circulation of the model (Figure 19a) and observational circulation derived from SSH calculated horizontal geostrophic velocities (Figure 19b) comparison shows that the simulated general circulation is able to generate the Rim Current, its location and its related features. In comparison to Figure 19b model upper layer circulation is stronger than satellite measured geostrophic velocities. Model generated Rim Current

50

is narrower in comparison to satellite data derived Rim Current. In the south part of the eastern Black Sea the mean Rim Current velocity is weaker while it is stronger in the western Black Sea. Overall, mean annual upper layer circulation pattern generated by the model indicates that model is capable of reproducing the general circulation features of the Black Sea dynamics consistent of the Rim Current and major semi-permanent eddies (Batumi, Sevastopol, Sinop and Kizilirmak eddies).
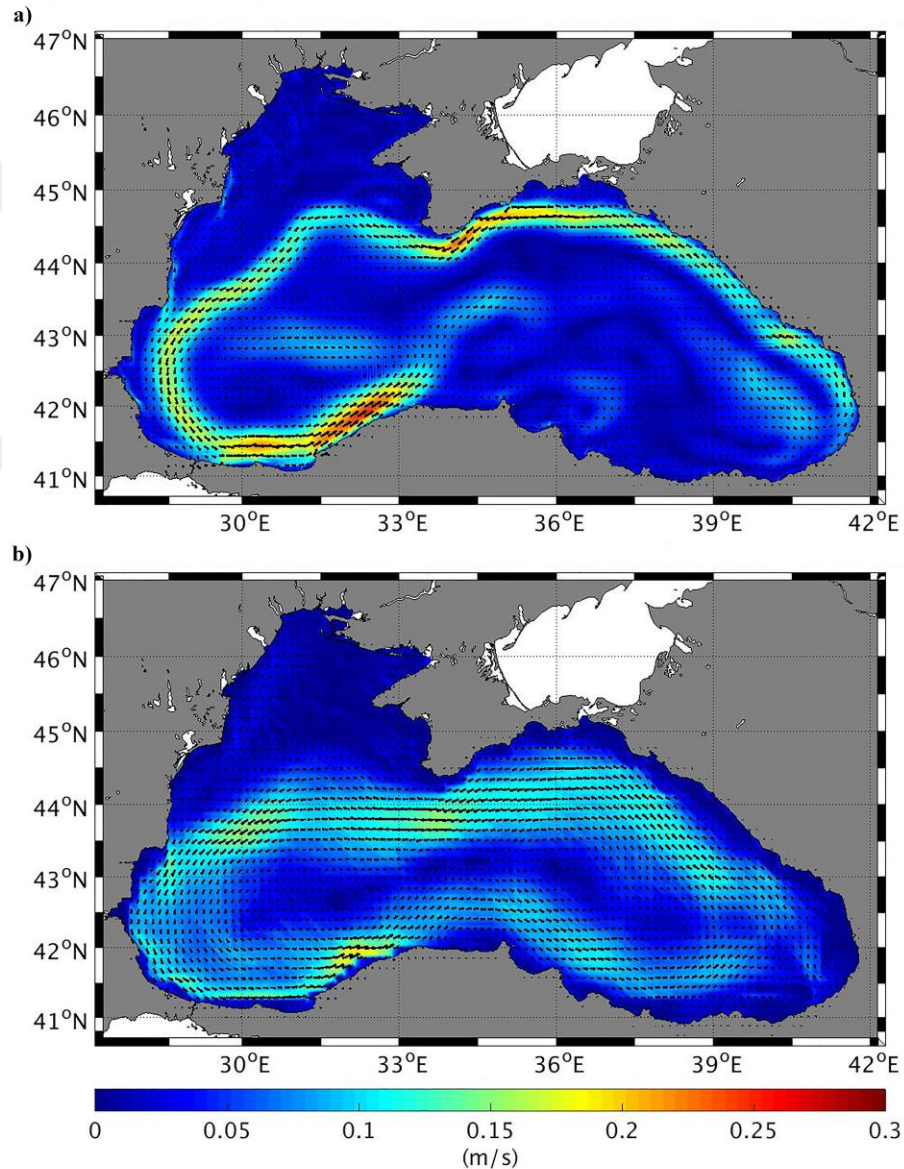
Figure 19: Mean sea surface circulation of model computed velocity (a) and geostrophic velocities derived from satellite SSH (b), (1993-2014).

51

3.1.5 Eddy Statistics and Kinetic Energy Calculations

To assess model skill in reproducing mesoscale phenomena, Eddyscan algorithm that utilizes thresholding to detect eddies in SSH data, for both model and satellite SSH data is used. Results of the eddy statistics analysis reveal that during 1985-2014 mean total 47 eddies are detected from satellite SSH comprised of 22 and 25 cyclonic and anticyclonic eddies, respectively. Mean total number of eddies for model computed SSH data is 95 consist of 50 and 45 cyclonic and anticyclonic eddies, respectively. While the algorithm detects about double the amount of eddies in the model than in the satellite data, the time series of model eddy abundance follows a similar temporal pattern than the satellite detected eddy abundance (Figure 20a) with a correlation of 0.28, indicating that the model is able to capture the general temporal dynamics of the mesoscale variability. The model is partially able to follow cyclonic eddy variability (Figure 20b) (r = 0.09) but for anticyclonic eddies visually there is a good match between model and satellite eddy variability (Figure 20c) (r = 0.16). The total number of modeled eddies (cyclonic and anticyclonic eddies) is double the total number of eddies detected from satellite data. One and the main reason for the mismatch between model and satellite detected eddy abundance is the coarse resolution of satellite data for the Black Sea (0.125° × 0.125° – 13.875 km × 13.875 km) in comparison to the model (3 km × 3 km) which results in a lower number of detected of mesoscale eddies. In addition, the satellite SSH data from 1985 to 1992 being weekly averages, compared to the daily data after 1993. This results in a smoothed SSH field and hence detection of eddy variability in that time. For this reason the model-data comparison before 1993 is omitted in this analysis.

Spatial comparison of the total amount of cyclonic eddies in the Black Sea in 2014 from model computed (Figure 21a) satellite SSH (Figure 21b) show that cyclonic eddies are mostly abundant in the middle of the basin, however, they are spread in the continental shelf and coastal areas. Unlike cyclonic eddies anticyclonic eddies in both model (Figure 22a) and in satellite data (Figure 22b) are abundant in coastal areas and continental shelf, mostly between the Rim Current path and the continental shelf. Thereby the presence of anticyclonic eddies in the inner basin occurs mainly in summer time as the Rim Current weakens and vanishes while cyclonic eddies are present mostly in the inner Black Sea and are transported toward the coastal areas.
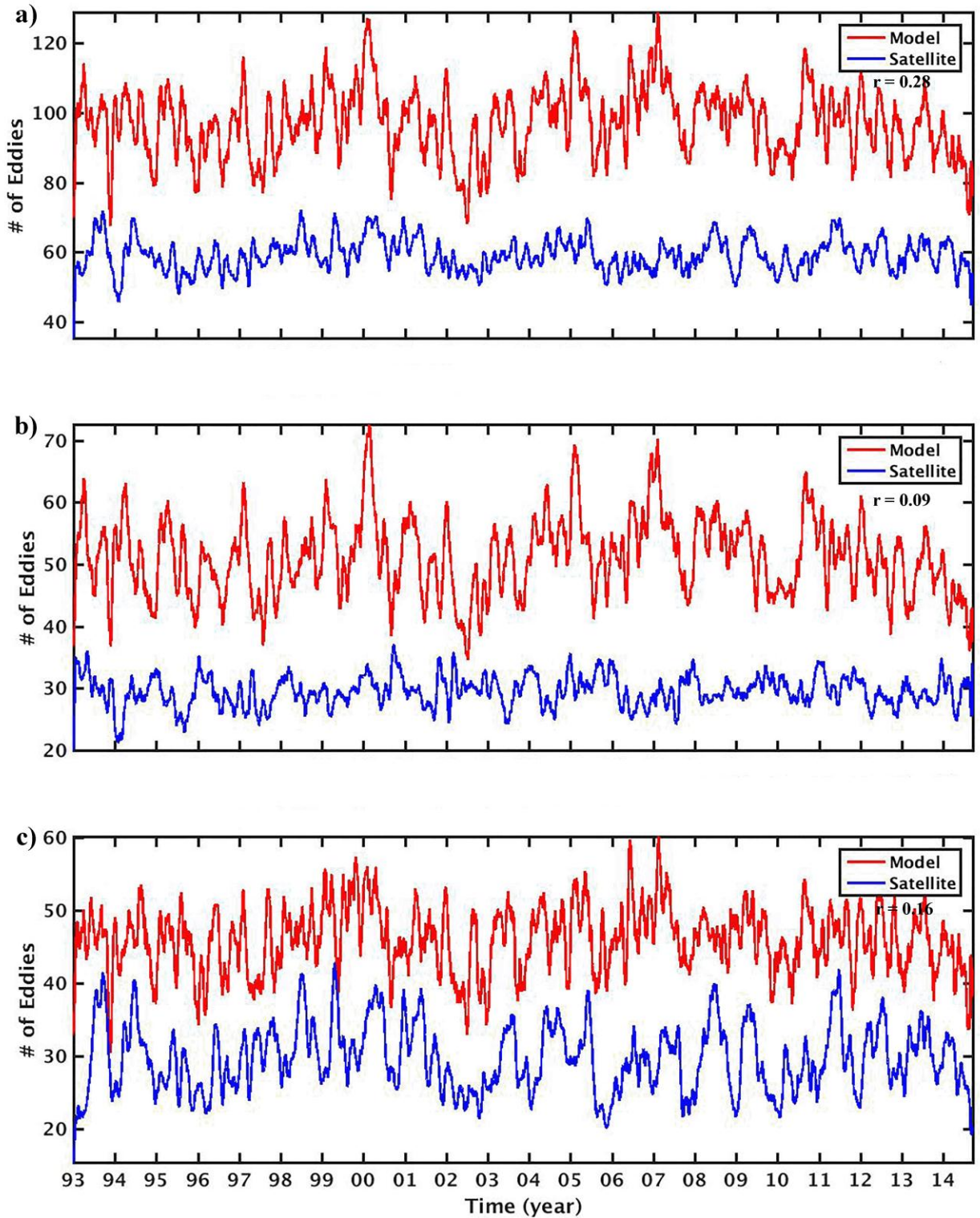
Figure 20: Model (red line) and satellite (blue line) SSH assessed data for eddy statistics analysis. Total number of eddies detected from model and satellite SSH data (a), total number of cyclonic eddies (b) and anticyclonic eddies (c) from model (red line) and satellite (blue line) SSH data.

53
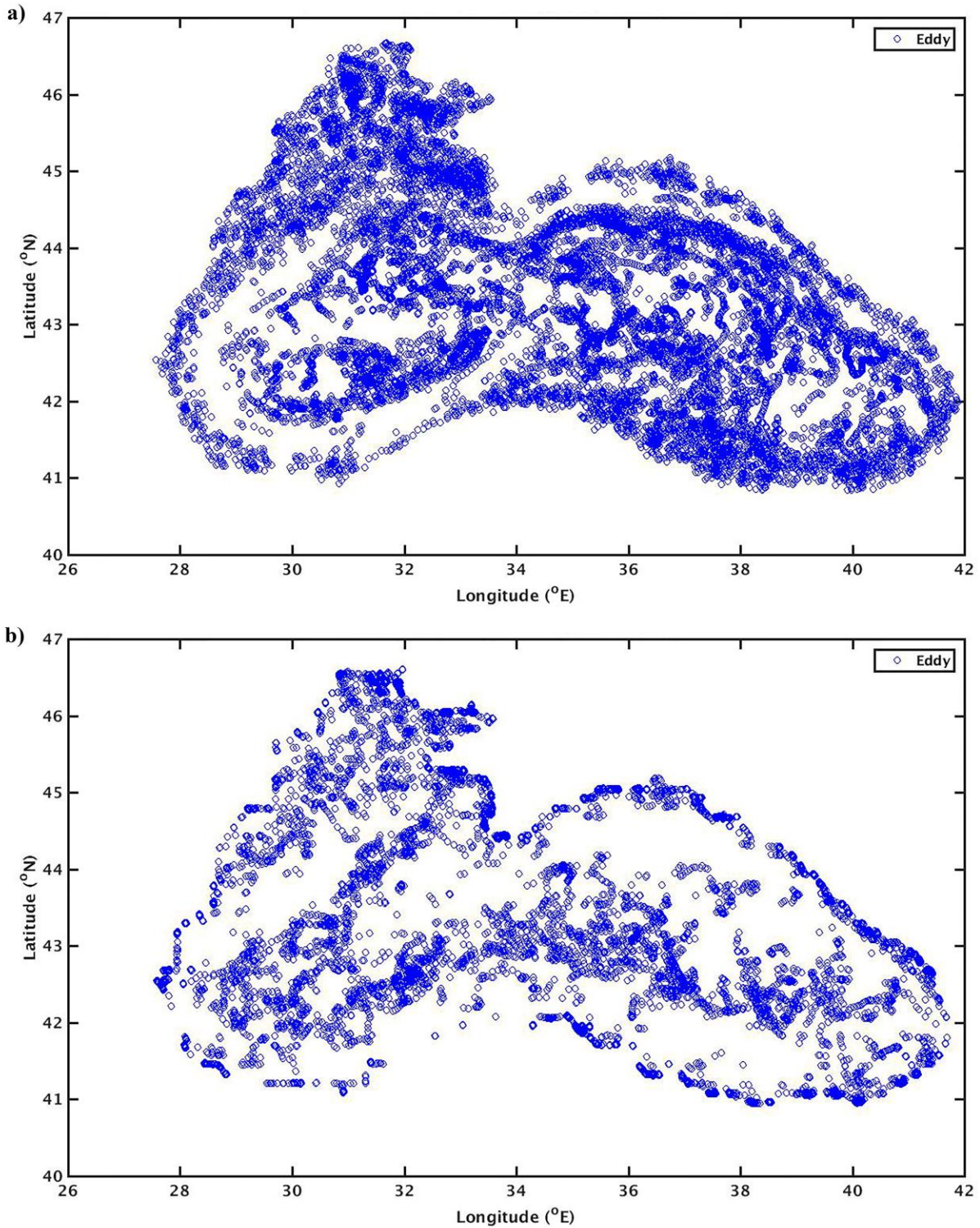
Figure 21: Eddy density map illustrating concentration of cyclonic eddies in the Black Sea captured from model computed SSH scan (a) and satellite SSH data scan (b).
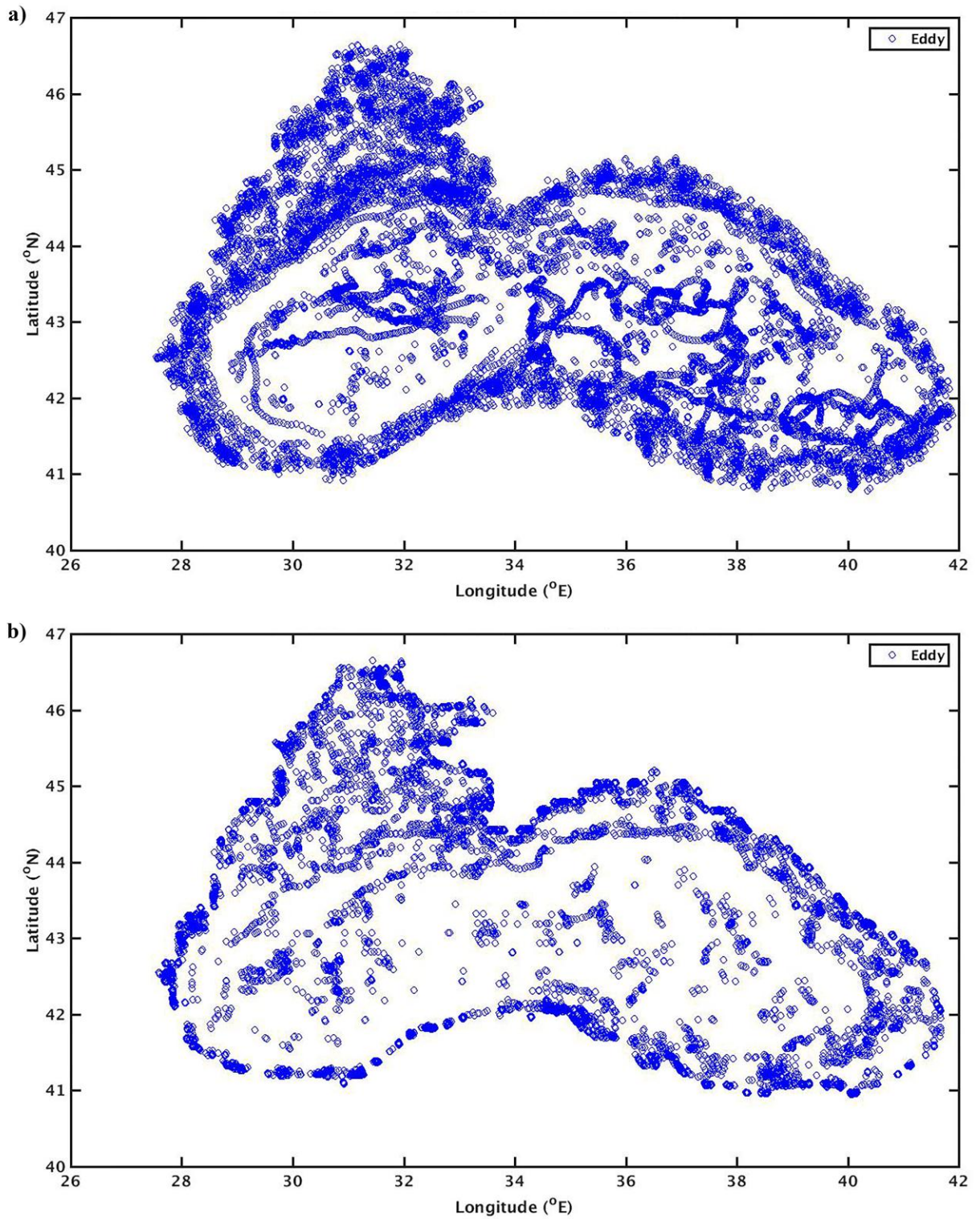
Figure 22: Eddy density map illustrating concentration of anticyclonic eddies in the Black Sea captured from model computed SSH scan (a) and satellite SSH data scan (b).
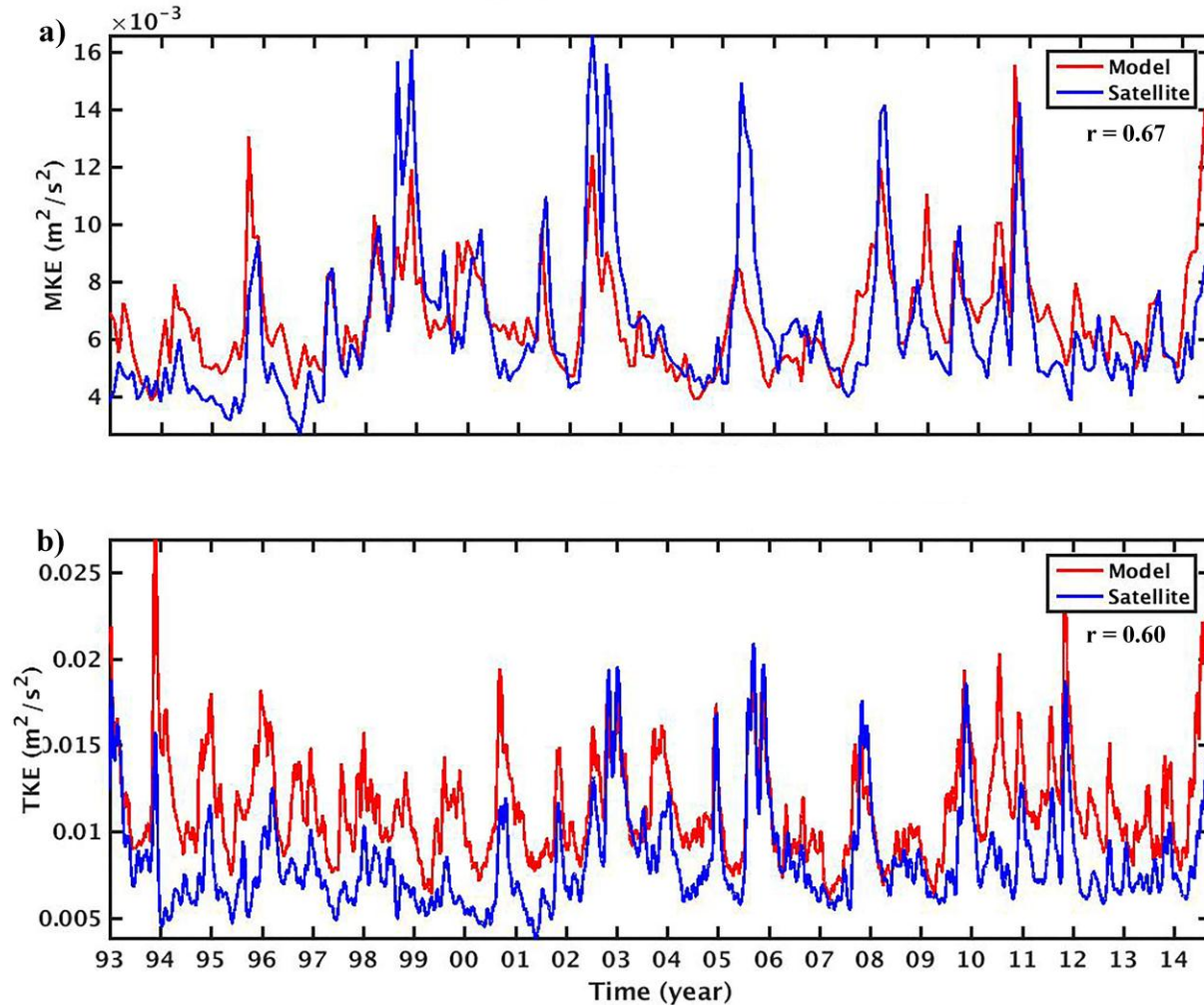
Figure 23: Model and satellite MKE (a) and TKE comparison (1993-2014).

Comparison of model calculated MKE and TKE with satellite derived MKE and TKE over 26 years shows high agreement between both (Figure 23). Satellite derived TKE shows a shift towards higher values following 2002 which is not detected by model. This is most likely due to the atmospheric forcing data, specifically, the wind data used in forcing the model. Previous studies show that in an increase in wind stress curl a shift is observed in other wind data such as SeaWinds data for the Black Sea at the same time as the shift in TKE and have hypothesized it may have caused a shift in TKE in the Black Sea (Arkin et al., 2016). Such a change in wind stress curl is not observed in the ERA Interim data used to force the model in this study (Figure 24). However, correlation coefficient for MKE and TKE is 0.67 and 0.60, respectively, indicating that overall model performance is good.

56
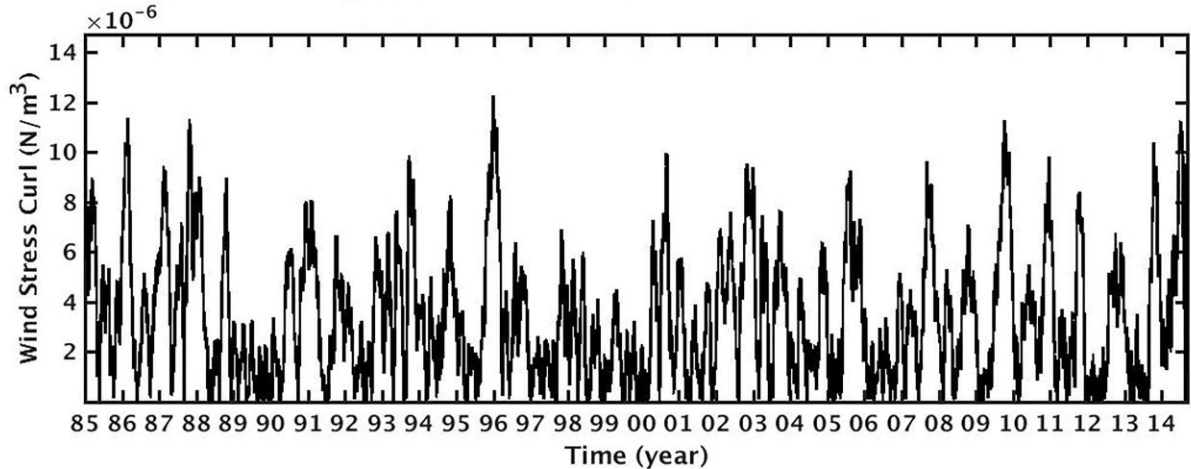
Figure 24: Wind stress curl calculated from Era-Interim 10 m wind data from 1985 to 2014 for the Black Sea.

3.2 Model Validation Part I: Univariate Analysis

The univariate validation techniques applied in this chapter provide an understanding of model skill. The in-situ data used for this model-data comparison, the Black Sea - Temperature and salinity observation collection V2 covers the same period (30 years) as the model run. However, some periods of this time span, specifically 2000 – 2009, contain only limited in situ data which make a direct year-by-year comparison difficult. Hence, the 30-year model simulation is divided into warming and cooling periods by analyzing the temperature distribution and univariate validation techniques are applied to each period separately, ensuring sufficient observations for comparison. To identify different periods the simulated winter SST is used, cooling and warming trends are determined applying linear regression analysis following Oguz (2005) and Oguz and Gilbert (2007), as it is the most important physical property reflecting climate variability. Three cold cycles (denoted by C1, C2 and C3) and two warm cycles (denoted by W1 and W2) are determined this way (Figure 25). The period from 1985 to 1993 (C1) is characterized by the range of winter SST variations between 8.7 and 6.4 °C and is followed by a warming period from 1994 to 2001 with warming phase (W1) ranging from 6.4 to 9.13 °C showing a high temperature increase. A new cooling phase (C2) is identified from 2002 to 2007 with ~1.04 °C SST decrease. Thereafter, another warming period (W2) with a sharp temperature increase of ~1.4 °C from 2008 to 2010 occurs. From 2011 to 2014 the third cooling phase (C3) with ~1 °C winter SST decrease is identified.
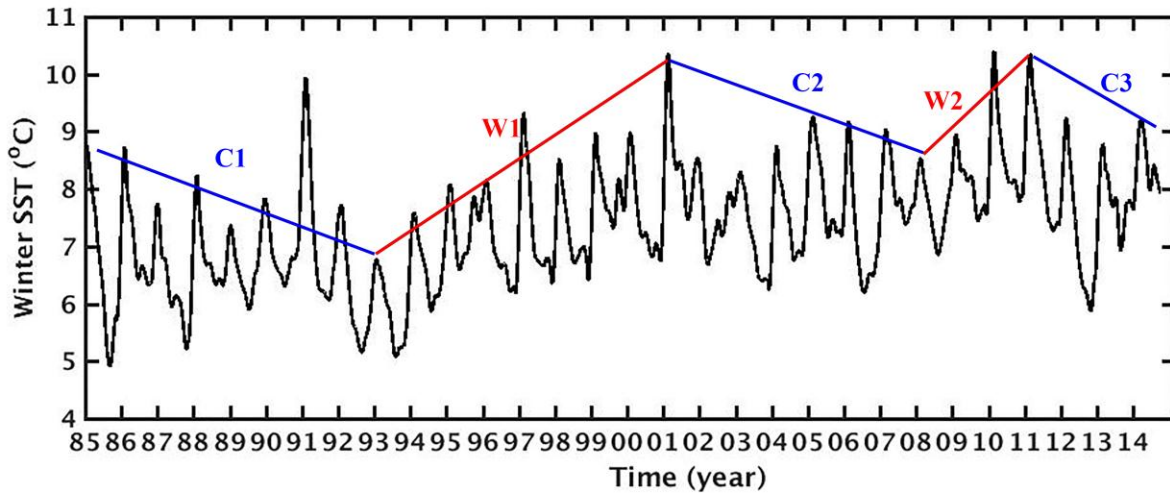
Figure 25: Long term variations of simulated winter (January - March) mean sea surface temperature (°C) averaged over entire basin to define cold and warm cycles.

3.2.1 Water Column Temperature and Salinity Model – In-Situ Data Comparison

Univariate validation of the model with in-situ observations of temperature and salinity are performed considering cold and warm years (Table 6, Table 7 and Table 8). Model produced water temperature and salinity and in-situ data is compared considering the nearest model grid to the observation data and model computed values are interpolated to observation data grid points and depth. Model computed temperature and salinity in almost all cooling/warming periods is highly correlated with in-situ data. However, in the last period, 2012-2014 temperature correlation coefficient is less than the other periods which is in part due to the scarce in-situ data available for comparison of model output and data. But overall performance of model in comparison with in-situ data is good (Table 6). The periods 1985-1993 and 2009-2011 best resolve temperature and salinity with higher correlation coefficients (Table 6 and Table 7). The mean absolute error (*MAE*) for temperature and salinity gives the absolute difference between model results and in-situ observation data which is equal to 0.91°C and 0.43 psu (Table 8), respectively, which is in a good agreement with measured values over the water column. The mean bias error (*MBE*) describes the direction of the error bias, whereas a positive *MBE* indicates that model results are greater in value than observations. Accordingly, the values of 0.80 °C and -0.61 psu reveal overestimation of model in comparison to observations for temperature and underestimation for salinity (Table 8).

The obtained values for model efficiency (*NSME* or *ME*) index introduced in 2.3.1 is 0.65 for temperature and 0.74 for salinity meaning that model efficiency for temperature and salinity is in excellent match with in-situ data as described in 2.3.1. Obtained values for temperature and salinity P_{bias} are 8.30 and 0.88, respectively, indicating lower magnitude (in excellent range) values for the model simulation (Table 8).

Univariate skill assessment metrics *STD, RMSD* and *r* presented in Tables 7 and 8 are visualized in the form of Taylor diagrams for temperature and salinity in the five different time periods chosen above (Figure 26, Figure 27). Interpolation of model computed values onto observation grid points is a source of error which leads to a decrease in model efficiency during model-data comparison. However, *STD* for salinity computed by the model is close to observations which reveals a high model efficiency (model: 1.63 psu, data: 1.95 psu) (Table 8). There is about 0.62 difference between model (2.93 °C) and in-situ data (3.55 °C) for water temperature *STD* which shows that model captures water temperature seasonality with a small difference from measured data; the model is producing colder temperatures. Root mean-square deviation (*RMSD*) of temperature and salinity is 1.76 °C and 0.98 psu, respectively. This indicates that model is able to detect seasonality (warming and cooling) and it reacts to freshwater discharge in spring leading to ~1 psu deviation of salinity from the mean. Correlation coefficient for temperature is 0.84 and for salinity is 0.86, showing that the model fits data well (Table 8).

The model's performance in computing SSH in the form of Taylor diagram (Figure 28) for the entire model run of 30 years in which satellite data is available reveals that the correlation coefficient is 0.57 which is acceptable for SSH. *STD* and *RMSD* obtained from model and satellite data comparison are 0.075 and 0.085, respectively.

Table 6. Statistical metrics describing model performance in comparison to in-situ observational temperature data.

Temperature	Model								In-Situ Data			
	Mean	MAE	MBE	NSME	P_{bias}	STD	RMSD	r	Mean	STD	RMSD	r
1985-1993	9.16	0.76	+0.67	0.77	6.85	2.96	1.59	0.90	9.84	3.62	-	1
1994-2001	8.80	0.77	+0.67	0.68	7.08	2.86	1.77	0.85	9.47	3.36	-	1
2002-2008	10.35	1.17	+1.03	0.79	9.08	4.14	1.99	0.91	11.38	4.93	-	1
2009-2011	9.06	0.59	+0.52	0.76	5.51	2.53	1.43	0.89	9.59	3.15	-	1
2012-2014	7.65	1.30	+1.14	0.26	13.01	2.18	2.02	0.67	8.80	2.71	-	1

Table 7. Statistical metrics describing model performance in comparison to in-situ observational Salinity data.

Salinity	Model								In-Situ Data			
	MEAN	MAE	MBE	NSME	P_{bias}	STD	RMSD	r	MEAN	STD	RMSD	r
1985-1993	20.67	0.34	+0.03	0.78	0.17	1.63	0.86	0.88	20.70	1.86	-	1
1994-2001	20.71	0.33	-0.05	0.82	0.26	1.57	0.74	0.91	20.65	1.78	-	1
2002-2008	19.94	0.79	-0.63	0.56	3.26	1.88	1.78	0.79	19.31	2.86	-	1
2009-2011	20.64	0.35	+0.05	0.75	0.27	1.50	0.84	0.86	20.70	1.68	-	1
2012-2014	19.68	0.38	-0.09	0.79	0.48	1.60	0.71	0.89	19.59	1.59	-	1

Table 8. Overall mean statistical metrics describing model performance for temperature and salinity in 1985-2014.

	Model	MEAN	MAE	MBE	NSME	P_{bias}	STD	RMSD	r
1985-2014	Temperature	8.04	0.91	+0.80	0.65	8.30	2.93	1.76	0.84
	Salinity	20.32	0.43	-0.61	0.74	0.88	1.63	0.98	0.86
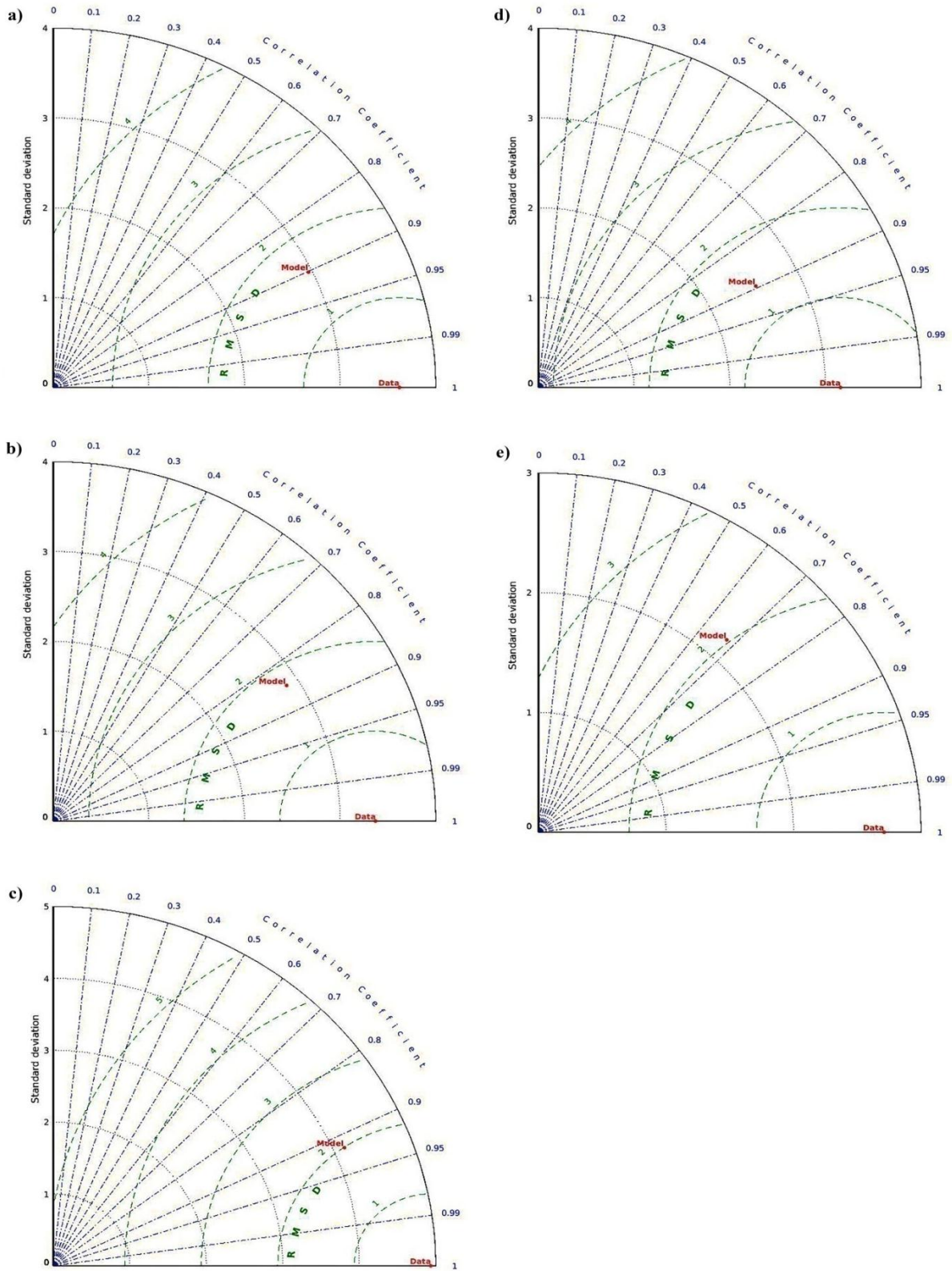
Figure 26: Taylor diagram illustrating model performance in temperature in 1985-1993 (a), 1994-2001 (b), 2002-2008 (c), 2009-2011 (d) and 2012-2014 (e).
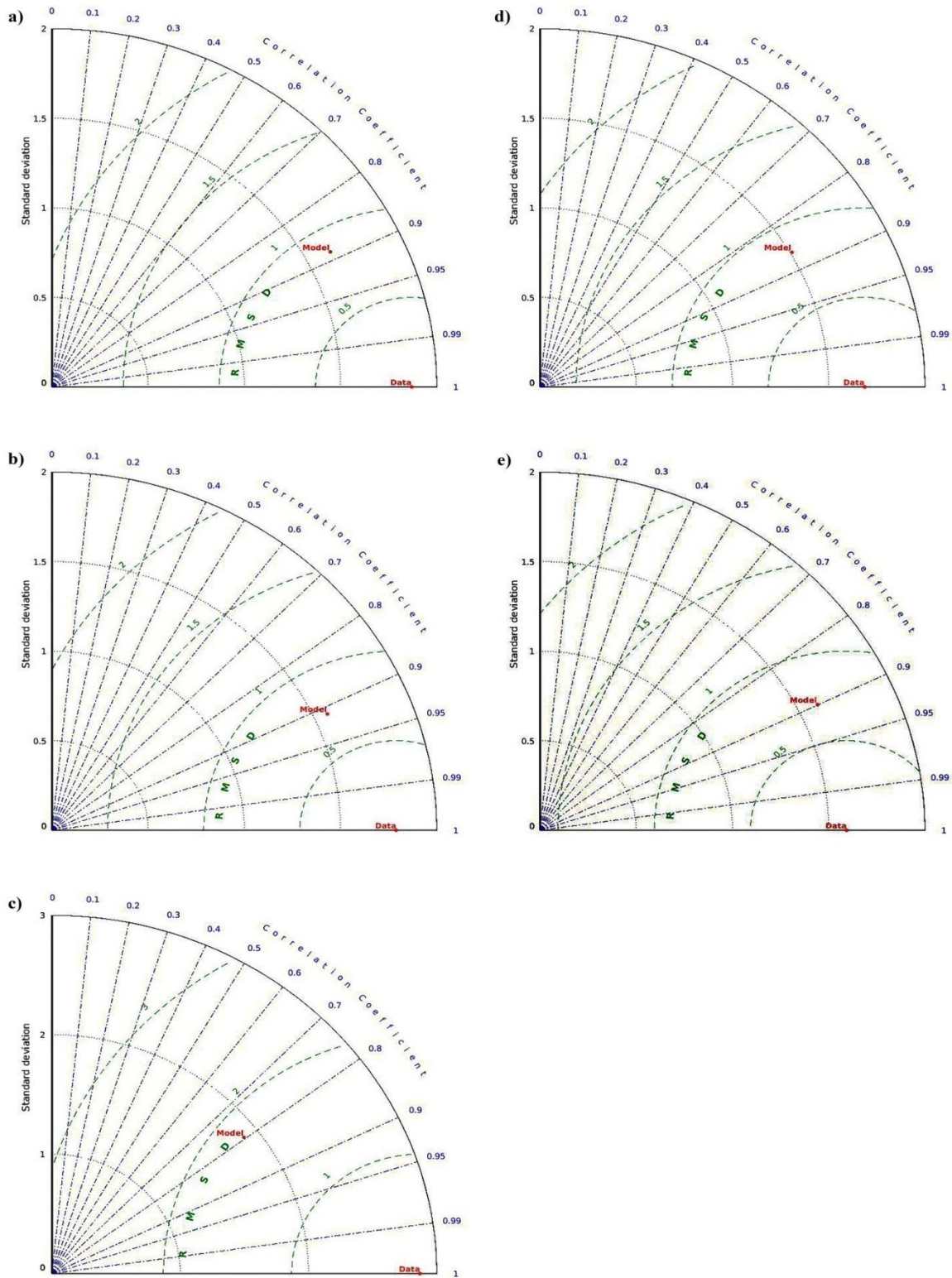
Figure 27: Taylor diagram illustrating model performance in salinity in 1985-1993 (a), 1994-2001 (b), 2002-2008 (c), 2009-2011 (d) and 2012-2014 (e).
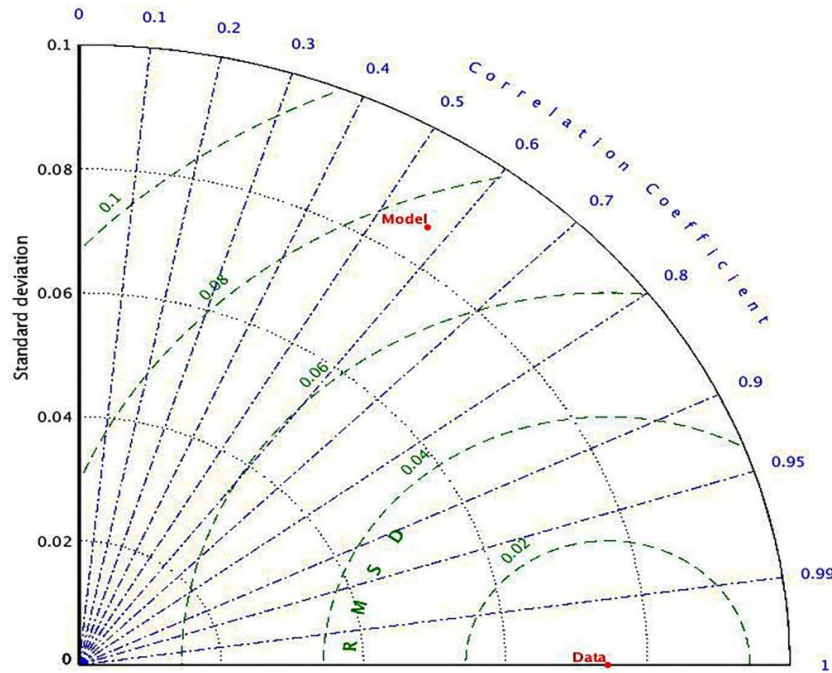
Figure 28: Taylor diagram illustrating model performance in sea surface height (1985-2014).

3.3 Model Validation Part II: Multivariate Analysis

To further assess model performance in computing SST, model SST is compared with satellite SST data using multivariate analysis. The results of quantile analysis described in 2.3.2 reveal that the skill score of the model is nearly about 0.81 at small scales (6 km) and increases at large scales to about 0.95 for SST (Figure 29) (Table 9). Higher model skills are achieved for the lowest and the highest quartiles at all spatial scales. Skill score of greater than 0.8 for SST indicates that model computed values for SST fits satellite measured SST well. The tracer restoring described in 2.2.10 plays a major role in achieving high accurate SST.

Model SSH comparison to satellite measurements through quantile analysis shows that smaller spatial scales have lower skill score values in comparison to larger spatial scores (Figure 30), as seen in the SST analysis. The 5th quantile corresponds to the upper range of SSH meaning that model is able to capture large scale dynamics of the Black Sea. Minimum mean skill score belongs to small scales and is 0.567 indicting that model is not able to locate meso and sub-mesoscale features as in satellite data but as the spatial scale becomes larger model performance improves and mean skill score is 0.962. Detailed skill score of model is given in Table 10.
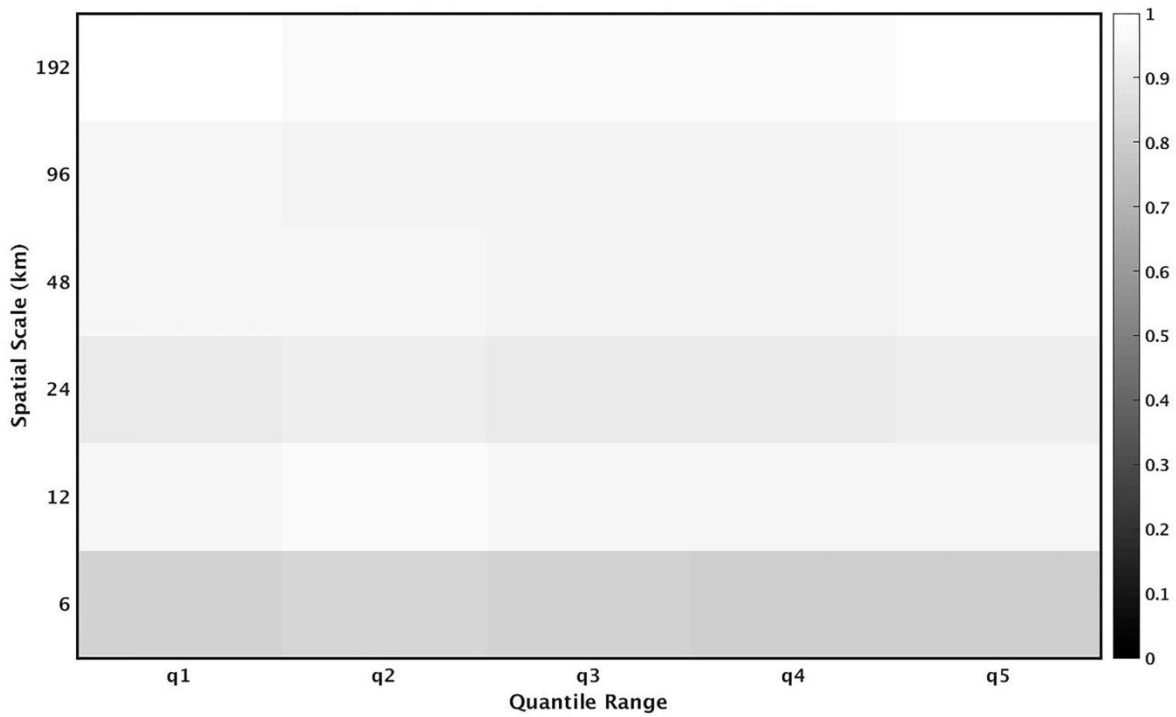
Figure 29: Spatial scales versus quantile ranges plots for the period 1985-2014 sea surface temperature skill scores.

Table 9: Model SST skill score values obtained through quantile analysis. Mean skill score at a smaller spatial scale (6 km) is 0.815 and in the largest spatial scale (192 km) is 0.985.

Quantile		q1	q2	q3	q4	q5
	6 km	0.816	0.837	0.821	0.805	0.799
	12 km	0.959	0.968	0.966	0.967	0.966
Skill Score	24 km	0.917	0.922	0.916	0.919	0.925
	48 km	0.958	0.953	0.950	0.952	0.957
	96 km	0.965	0.952	0.946	0.948	0.961
	192 km	0.990	0.983	0.982	0.983	0.989
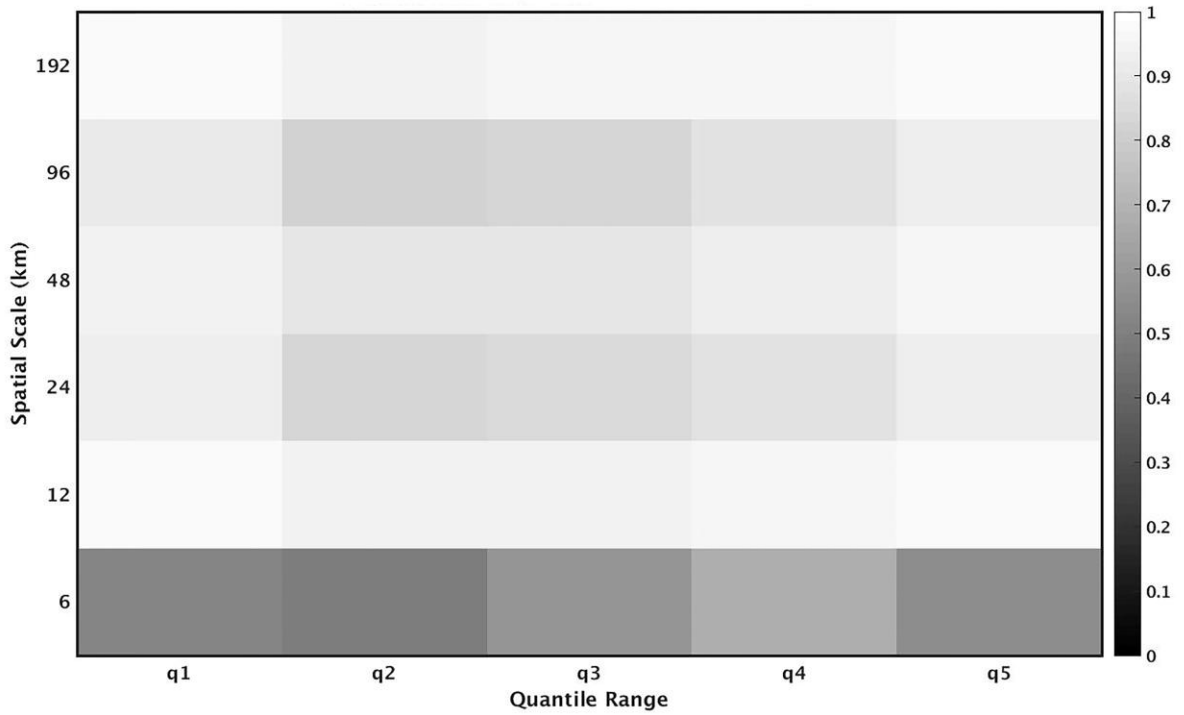
Figure 30: Spatial scales versus quantile ranges plots for the period 1985-2014 sea surface height skill scores.

Table 10: Model SSH skill score values obtained through quantile analysis. Mean skill score at a smaller spatial scale (6 km) is 0.567 and in the largest spatial scale (192 km) is 0.962.

Quantile		q1	q2	q3	q4	q5
	6 km	0.515	0.493	0.592	0.680	0.553
	12 km	0.976	0.949	0.951	0.960	0.979
Skill Score	24 km	0.922	0.834	0.848	0.883	0.935
	48 km	0.950	0.894	0.903	0.9242	0.955
	96 km	0.910	0.817	0.843	0.884	0.928
	192 km	0.975	0.950	0.954	0.960	0.969

3.4 Model Validation Part III: EOF analysis

In this section modeled and satellite derived SST and SSH decomposed into their main first three EOF modes are described and the results of model and satellite EOF analyses are compared. Correlations between temporal EOF modes associated to SST and SSH are investigated. Total variances related to SST and SSH EOF modes are presented.

3.4.1 Sea Surface Temperature

SST fields measured by AVHRR instruments aboard NOAA polar-orbiting satellites every 5 days are compared with model SST. The first EOF mode corresponds to a basin-wide increase/decrease of the SST anomaly explaining over 97% of the variability for both model and satellite (Figure 31a). Associated spatial and temporal EOF mode 1 correlation is 0.99 (Figure 31a and Figure 32a). The good match between model reproduced SST and satellite SST is mainly due to SST restoring described in 2.2.10. Lower magnitude SST values are seen in the NWS, higher magnitudes are observed in the coastal areas and the continental shelf and medium magnitudes in the inner basin where western and eastern gyres along with the Rim Current are located (Figure 31a). Turkish coasts, Batumi, Caucasian and Crimean coasts and Sevastopol have higher magnitudes. First temporal EOF mode shows a seasonal cycle with positive values representing summer and negative values representing winter SST (Figure 32a). In general, model underestimates SST in comparison to satellite data and this difference is shown in EOF analysis as well as univariate assessment results. The second and third spatial modes explain nearly 1.5% and 0.22% of the variability and correspond to zonal and meridional gradient of SST anomaly, respectively (Figure 31b and c). Spatial and temporal correlations between model and satellite SST mode 2 is 0.99 and 0.97and this correlation for mode 3 is 0.97 and 0.95 respectively (Figure 31b and c, Figure 32b and c). Model is able to capture temperature difference between the eastern Black Sea with positive values and the NWS with negative values indicating cooler temperatures in the western Black sea and warmer SST in the eastern part (Figure 31b). The third spatial mode of EOF analysis gives a northeast and southwest difference with positive and negative values.
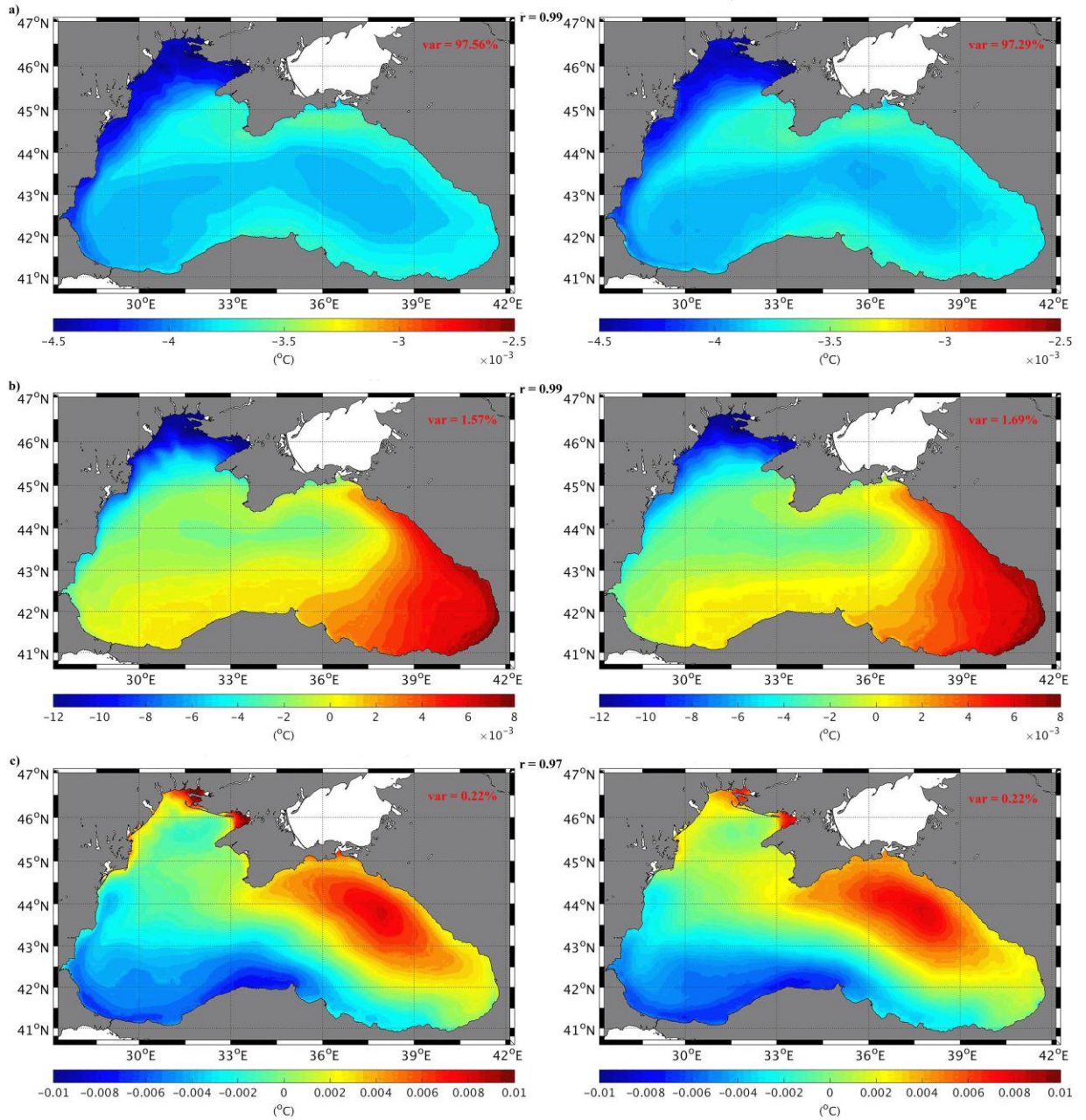
Figure 31: From top to bottom, the first three spatial EOF modes of the SST anomalies (1985-2014), sorted by decreasing order of variability: Mode 1 (a), Mode 2 (b) and Mode 3 (c). From left to right, the spatial structure of the model EOF, the spatial structure of the satellite EOF. The percentages of variability accounted for by modes are indicated on the right corners of the spatial maps.

Figure 32: From top to bottom the first three temporal EOF modes of model (red line) and satellite (blue line) of the SST (1985-2014), sorted by decreasing order of variability: Mode 1 (a), Mode 2 (b) and Mode 3 (c).

68

3.4.2 Sea Surface Height

Daily sea level anomaly (SLA) data is not available from 1985 to 1992, only weekly averaged data is available. Consequently, in order to avoid error in SSH EOF modes analyses, only the period 1993-2014 has been considered to assess model performance. The first spatial mode corresponds to the features associated with changing sea level due to the different water accumulation within the Sea, which is associated with the vertical displacement of water from draining and filling this estuarine basin (Figure 33a). This has been confirmed by other studies (Grayek et al., 2010; Capet et al., 2012). The first SSH EOF mode accounts for 76% and 62% of SSH variability in the model and satellite data, respectively. As shown in Figure 33a, the first spatial satellite and model derived mode are highly correlated with r = 0.99, meaning that the model is able reproduce the water budget dynamics and mean sea surface height in the Black Sea well.

In Figure 33b, the second spatial EOF mode, higher magnitude anomalies are observed in the periphery and lower magnitude values are seen in basin interior, perceiving that there is a border between the inshore and offshore which is the main characteristic of the Rim Current. It is inferred that the second spatial EOF mode represents major characteristic feature of the Black Sea consisting of the strong Rim Current and permanent eddies (Batumi, Kizilirmak and Sinop), features associated to the variability of the sea surface curvature (Figure 33b) (Grayek et al., 2010; Capet et al., 2012). The second SSH EOF mode accounts for ~15% and 28% of SSH variability in the model and satellite data, respectively. It can be seen here that the model is not able to reproduce the distinct feature of the Rim Current at the southeastern coast exactly but flow in the model is more influenced by eddies in this region. However, the second spatial satellite and model derived mode are correlated with r = 0.69 (Figure 33b), meaning that the model is able reproduce the large-scale circulation dynamics in the Black Sea.

The third spatial EOF mode represents the mesoscale features in the Black Sea and this mode is representing ~2% and 1.7% of SSH variability in the model and satellite data, respectively. The third spatial satellite and model derived mode are correlated with r = 0.34 (Figure 33c), meaning the model does not represent this mode well. This is most probably because of the rather weak winds from ERA Interim forcing data. This was to be expected and this problem may be fixed when using data assimilation of sea surface height in future versions of this model.
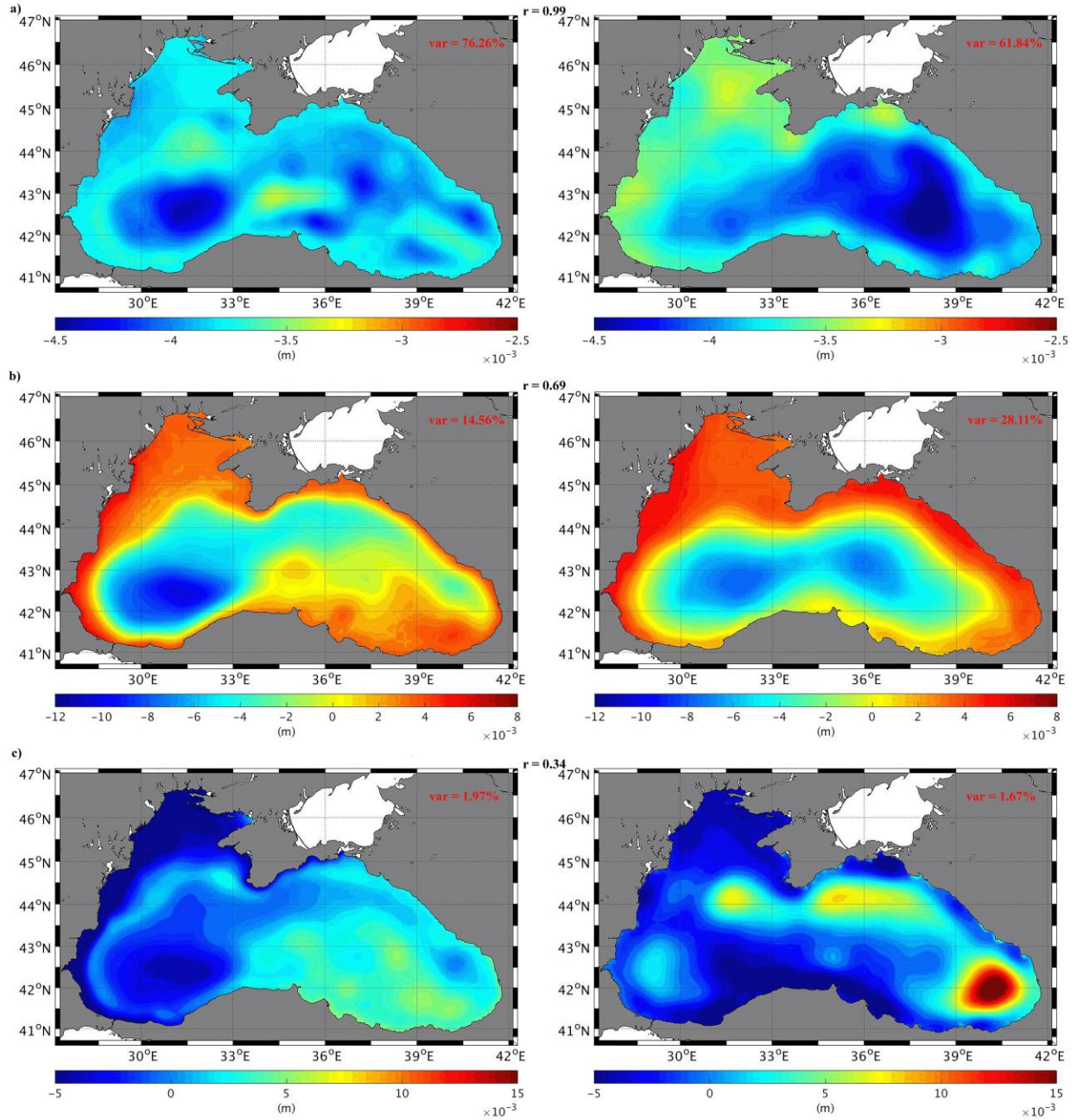
Figure 33: From top to bottom, the first spatial EOF modes of the SSH anomalies (1993-2014), sorted by decreasing order of variability. From left to right, the spatial structure of the model EOF, the spatial structure of the satellite EOF. The percentages of variability accounted for by modes are indicated on the right corners of the spatial maps.

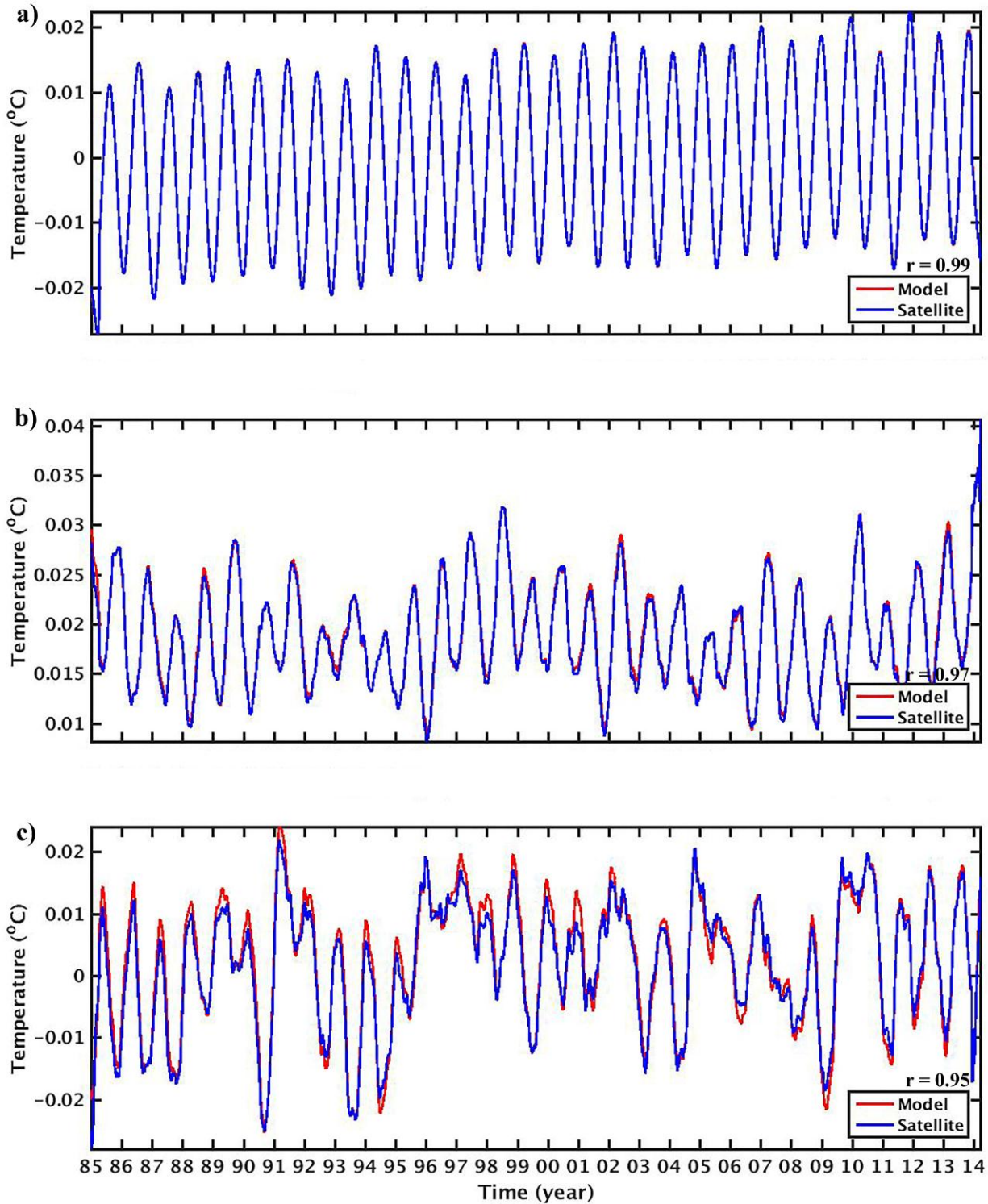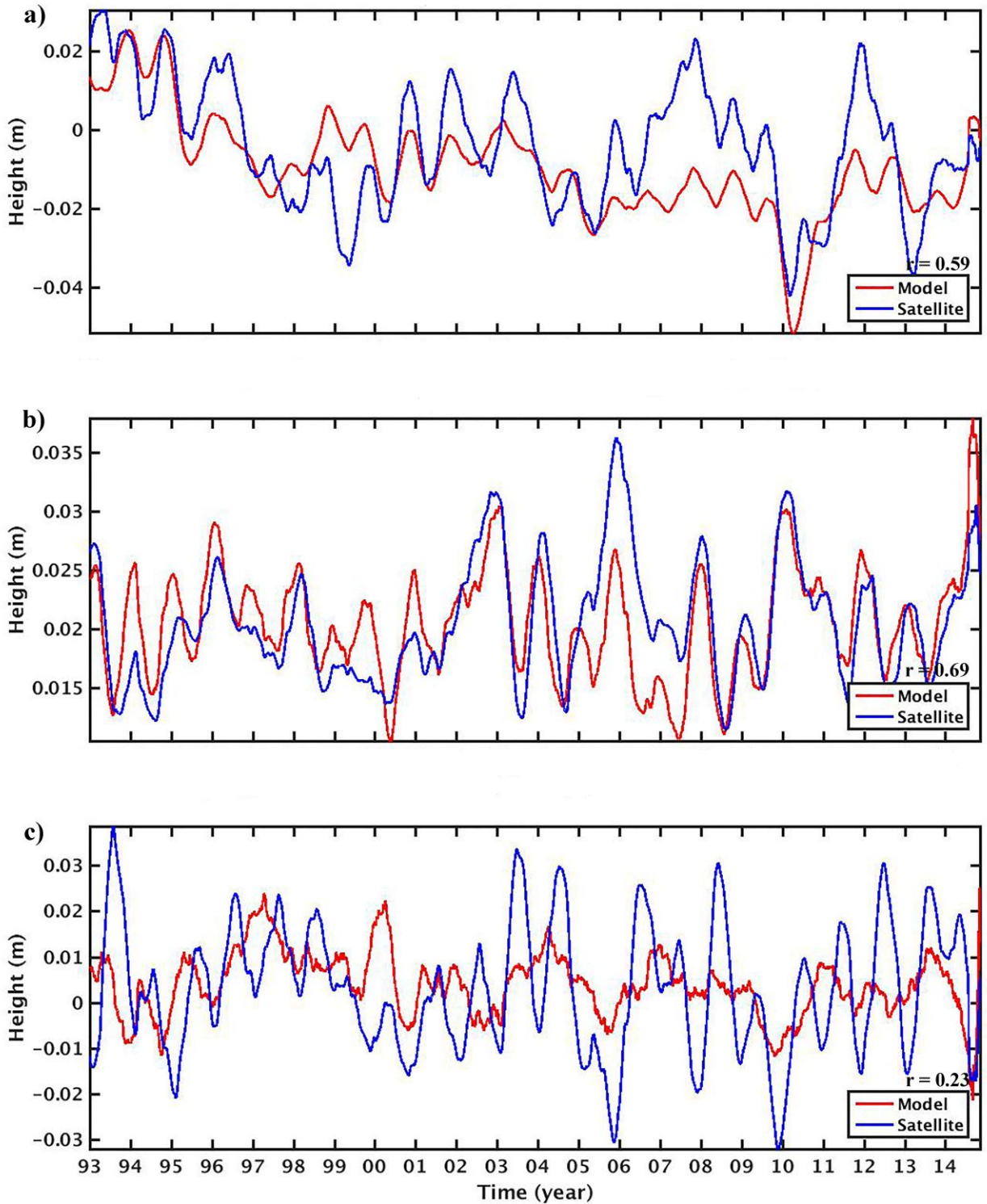**Figure 34:** From top to bottom the first temporal EOF modes of model (red line) and satellite (blue line) of the SSH anomalies (1985-2014), sorted by decreasing order of variability. Model and satellite temporal EOF mode 2 are highly correlated in comparison to mode1 and 3.

The temporal correlation between model and data EOF mode 1 is 0.59 (Figure 34a). Although the model cannot match the amplitude of the oscillations it reproduces SSH variability with a variance of 97% for model simulations (Figure 34a). This implies that model is capable of detecting annual and interannual variability of the water budget of the Black Sea. Supporting the finding that indeed the first temporal SSH EOF model is representing the rise and fall of the water level in the Black Sea a comparison of model basin averaged mean SSH with the first EOF mode (ADT-1) from 1985 to 2014 (Figure 35) shows that model basin averaged SSH follows ADT-1 variations over the whole period (r = 1.0). Further, the total water budget of the Black Sea of the model ADT-1 is correlated with the water budget of the Black Sea (Figure 36), r = 0.54. The mean sea surface height follows the variations of the water budget over the 30 years, other than some exceptional years (e.g. 2008, 2007 and 2008). This confirms that SSH increase and decrease is directly proportional to water fluxes variations. In spring and summer the increase in river fluxes results in increase of SSH.
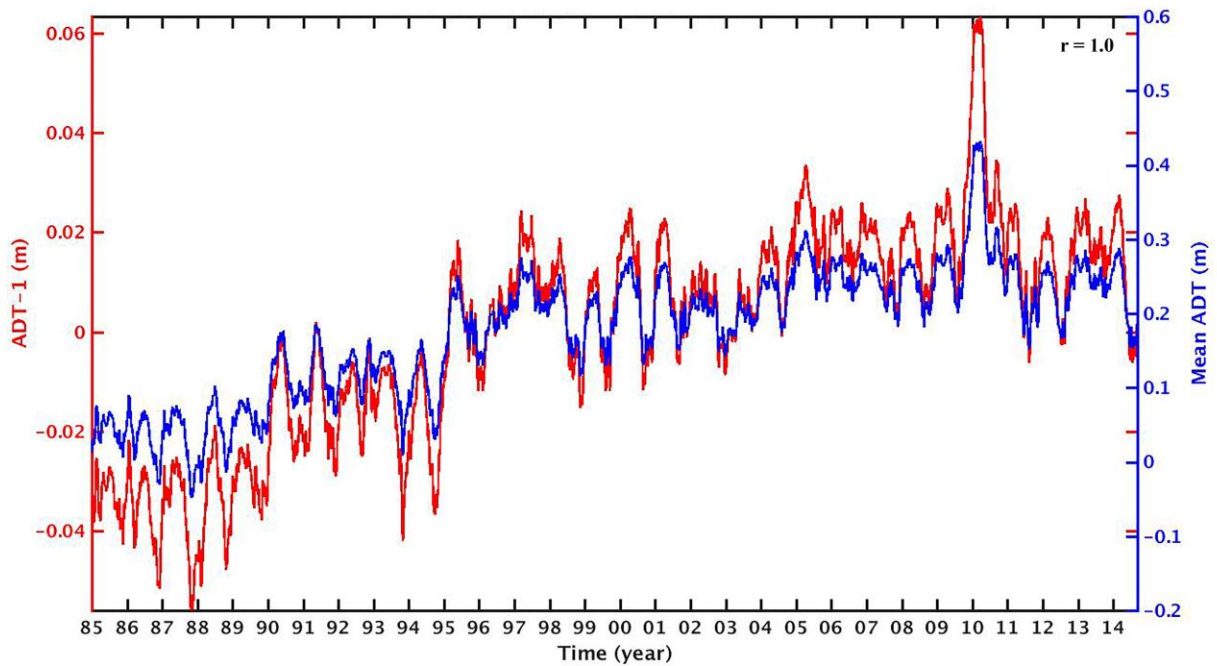
Figure 35: Comparison of mean model SSH (mean model ADT) and EOF mode-1 temporal component (ADT-1) from 1985-2014.
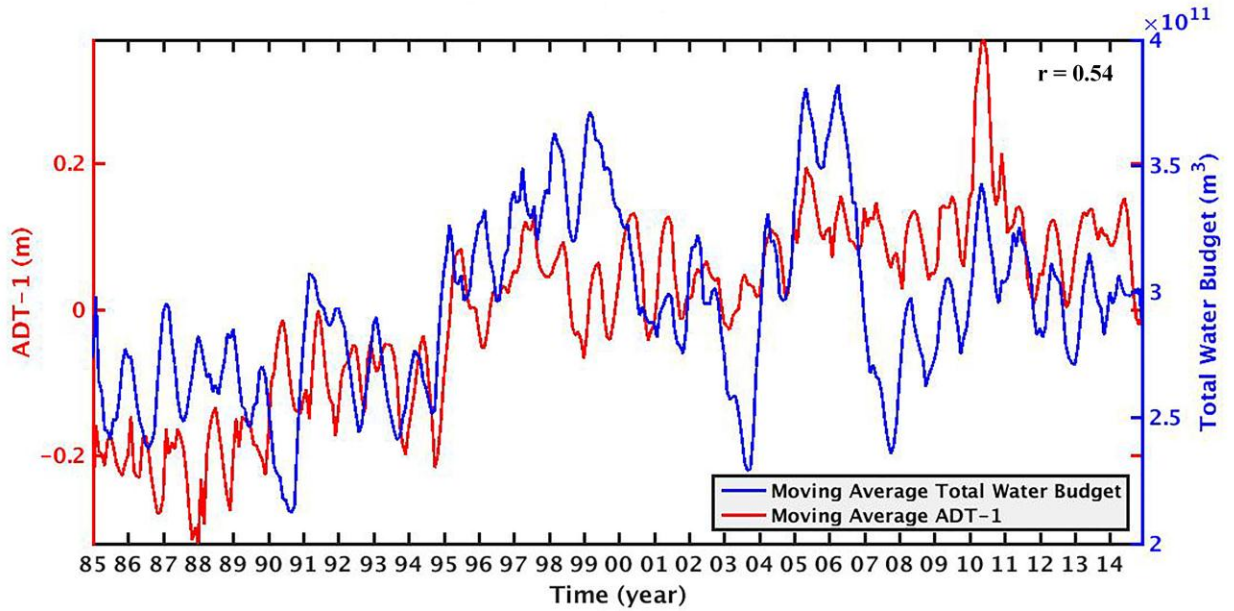
Figure 36: Total water budget and ADT-1 with a positive correlation coefficient, (r = 0.54).

The second temporal mode of model and satellite data are in good agreement with a correlation of 0.69 (Figure 34b). This mode shows the temporal variation of the Rim Current strength in the Black Sea. Its variations are closely related to the wind stress curl, which drives Rim Current strength and will be discussed in more detail in section 4.2 below. The third temporal EOF mode of satellite and model are correlated with r = 0.23 (Figure 34c), indicating that also the temporal variation of eddy variability is not well captured by the model as was to be expected.

CHAPTER 4

MODEL RESULTS

After the extensive model validation in chapter 3, where the skill and credibility of the model in reproducing the observed values was discussed, the variability in the simulated physical properties and upper layer dynamics of the Black Sea from 1985 to 2014 is investigated in this chapter with an emphasis on the effect of mesoscale structures in the cross-shelf transport. In the first part of this chapter long term variability of SST and SSS, CIL, MLD and isopycnal depth at the nitrate maximum are examined to asses if there are any observed trends. In the second part of this chapter the upper layer dynamics of the Black Sea are investigated using eddy statistics analyses, the calculations of kinetic energy and Ekman pumping. Further, in the third part of the chapter, the horizontal and vertical water exchange is studied in detail as this exchange plays a major role in functioning of marine ecosystems through controlling transport of nutrients and biogeochemical elements from the shelf to the interior basin and vice versa, as well as redistribution of nutrients within water column through transport and turbulent mixing.

4.1 Interannual Variability of Physical Properties in the Black Sea

Sea Surface Temperature

Sea Surface Temperature is one of the most important variables used as climate index and a major factor in defining the development of biological productivity, climate change and oceanographic phenomena in the marine ecosystems. Upper layer vertical mixing, stratification and hence, nutrient supply and primary production are controlled by SST variations. In the Black Sea a shallow mixed layer depth and weak vertical mixing leads to quick response of surface layer temperature to atmospheric forcing (Ginzburg et al., 2007) necessitating long term investigation of SST variations. The SST anomaly from 1985 to 2014 (Figure 37) shows a negative anomaly from 1985 to 1997 that turns into a positive anomaly from 1998 to 2014. This reflects to overall 30 year warming trend in the Black Sea of 0.0603 °C/year between 1985 and 2014, and an average increase of 1.81 °C over the 30 year period. Warming trend calculated from model outputs in the present study is close to most recent studies for the Black Sea by von Schuckmann et al. 2018 and Sheppard, 2018 that have calculated warming trend for the Black Sea equal to 0.075 and 0.08 °C/year, respectively.
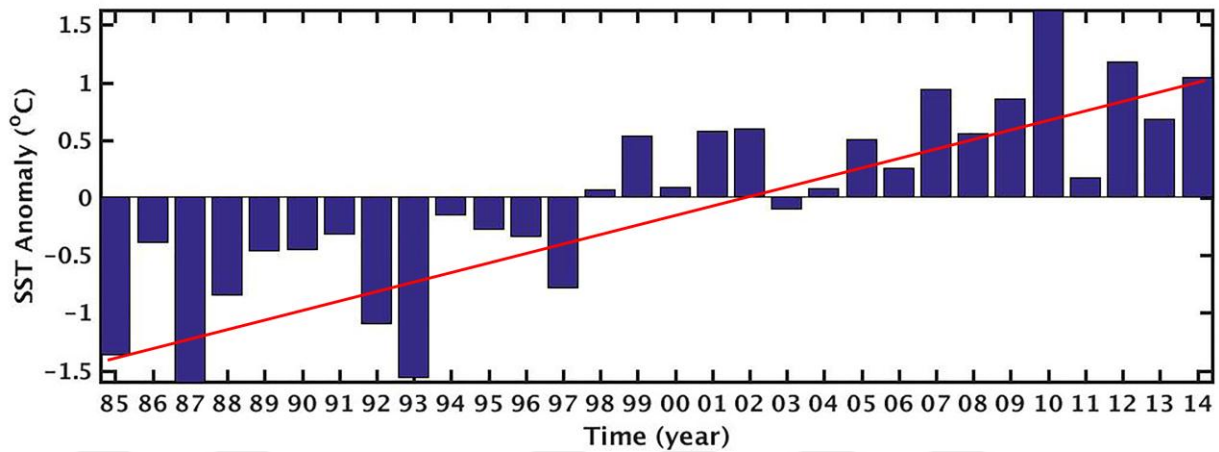
Figure 37: SST anomaly from 1985 to 2014.
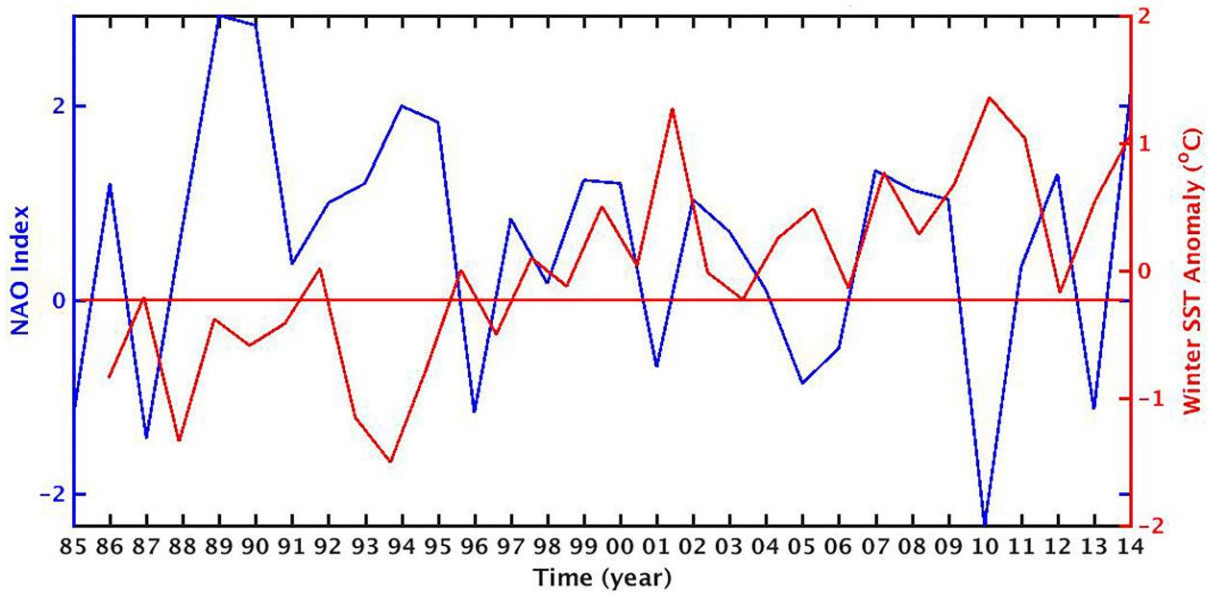
Figure 38: Winter SST anomaly (averaged over the months January-March) and NAO index form 1985 to 2014**.**

Over the whole period there are 14 years with negative SST anomalies and 16 years with positive SST anomalies (46.6% to 53.3%), which are solely an artifact of the presentation of anomalies here. Maximum negative anomalies belong to 1987 (-1.6 °C) and 1993 (-1.5 °C) show cooler years while maximum positive anomalies are seen in 2010 (+1.5 °C) and 2012 (+1.1 °C), marking exceptionally warm years (Oguz et al., 2006; Kazmin et al., 2010; Miladinova et al., 2017).

Studies of Oguz 2005; Ginzburg et al., 2007; Shapiro et al., 2010 show that winter SST anomalies are related to the winter indices of the North Atlantic Oscillation (NAO) which means that cold or warm air masses over the Black Sea influence the winter SST. Positive NAO is characterized by cold and dry air masses over southern Europe and the Black Sea and warm and moist air blowing over the Gulf Stream into northern Europe causing cold and dry winters in southern Europe and the Middle East and mild and wet winters in northern Europe (Oguz et al., 2006). Positive winter NAO index anomalies from 1985 to 1997 (Figure 38, blue line) represent cold and dry winters in the Black Sea that coincide with negative simulated winter SST anomalies (Figure 38, red line). Negative winter NAO index variations in 2001, 2005, 2010 and 2013 have coincidence with positive simulated winter SST anomalies resulting in mild and wet winters (Figure 38). Over the whole period a continuous warming trend of 1.81 °C is observed in the winter SST over 30 years (0.0603 °C/yr) this agrees with findings of Akpinar, (2016) obtained from satellite data (Figure 40, redline).

Cold Intermediate Layer

The effect of severe and cold winters is known to result in deeper mixing of the surface layer leading to deepening of the CIL and can also be observed in modeled CIL (Figure 39). CIL upper boundary changes from 21.2 m in 1985 to 36.2 m in 2014 with a mean upper depth of 25.5 m over the whole period (Figure 39a, blue line). The deepest depth of CIL formation (upper depth) during the period 1985- 2014 is 36.2 m in 2014 and its minimum depth is 18.7 m in 1993 (Figure 39a). Simulated bottom CIL depth varies from 134.5 m in 1985 to 102.9 m in 2014 (Figure 39a, red line). The deepest CIL bottom depth is observed in the years 1988 with a depth of 140 m and its minimum bottom depth is calculated to be at 99.9 m in 2011. Mean CIL bottom depth is 122.5 m. CIL thickness in 1985 is 113.3 m and changes to 66.7 m in 2014. Mean thickness of the CIL is 97.0 m in 30 years with its maximum and minimum in 1987 and 2014, respectively (Figure 39b). It should be noted here that to avoid any drift in the 30 year model run, the model uses temperature and salinity nudging below 207 m as described in 3.1. Hence the surface layer is free in the model and the shoaling of the CIL, as well as the decrease of its thickness is due to the warming trend of SST over the 30 year period. Minimum summer temperature for the CIL over the 30-year time interval reveals that there is a continuous warming trend (Figure 40, blue line), while over the same period a continuous warming trend of 1.81 °C is observed in the winter SST (Figure 40, red line). Minimum summer CIL temperature varies between 5.5 °C in 1985 and 7.0 °C in 2014 and is highly correlated to winter SST

(r = 0.88). This shows that continuous warming is transferred from the surface to subsurface layers influencing stratification and smaller temperature gradients and causing thinner CIL.
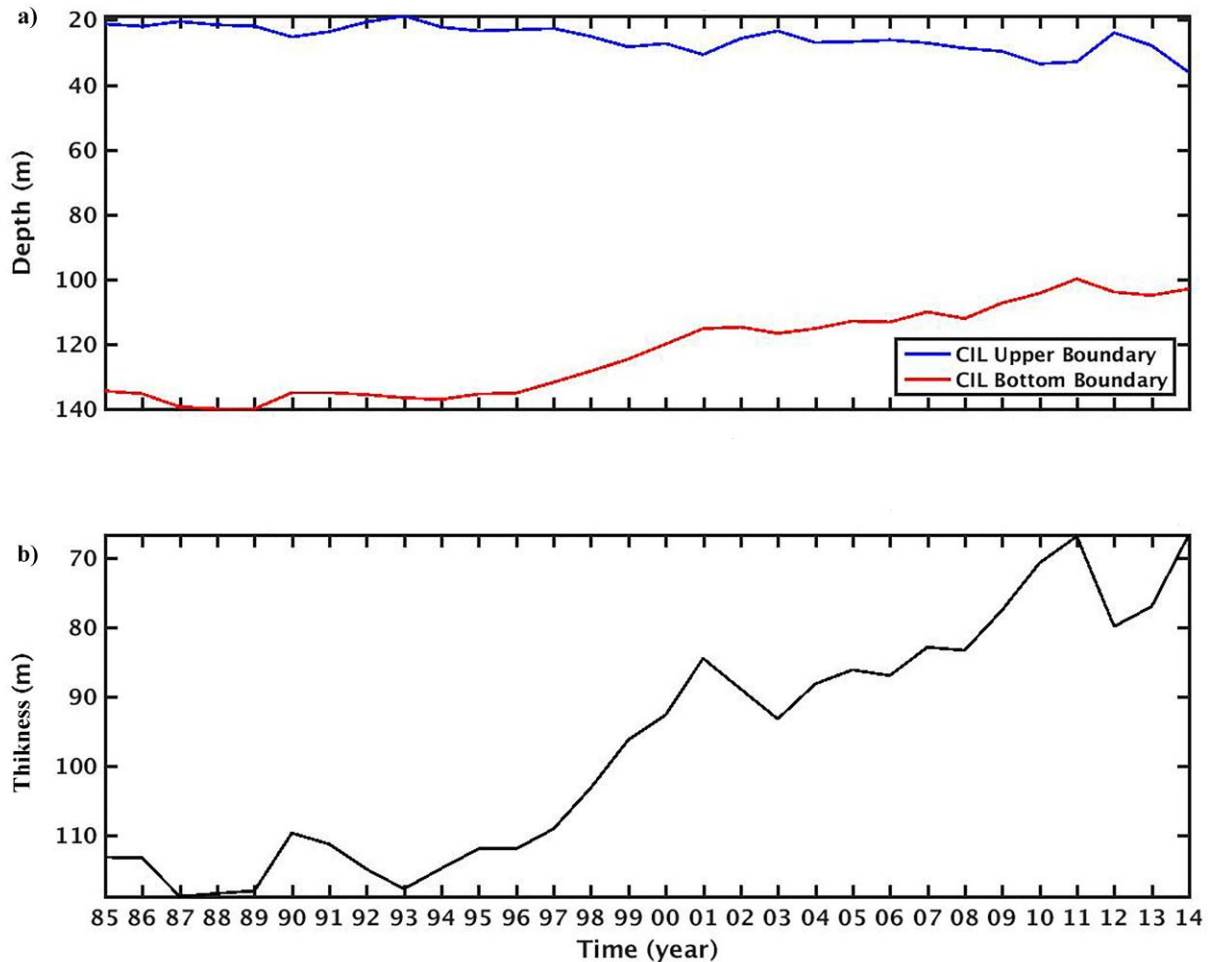
Figure 39: Simulated annual mean depth of Cold Intermediate Layer (CIL) (1985 - 2014) at a grid point in the center of the Black Sea (white circle in Figure 1). CIL mean upper and lower boundary depth is 23.31 m (blue line) and 116.10 m (red line), respectively (a). Annual mean CIL thickness variations (1985-2014), (b).

Mixed Layer Depth

Annual MLD anomaly shows no significant trend and has 13 positive and 17 negative anomalies over 1985 to 2014 (Figure 41). Maximum negative anomaly of MLD is 0.94 m and maximum positive MLD anomaly is 1.24 m. Hence, deviation from long term mean is about ±1 m. This implies that annual mean MLD of the Black Sea has not changed over the period and is not shoaling even

though the Black Sea is warming. This agrees with the study by Somavilla et al. (2017) that found that stratification during spring and summer as a result of warmer ocean surface stabilizes buoyancy due to heating and in autumn and winter destabilization of buoyancy forcing by the surface cooling convective mixing results in deeper MLD (Somavilla et al., 2017). Model calculates MLD from density differences and therefore, MLD is not influenced by SST variations.
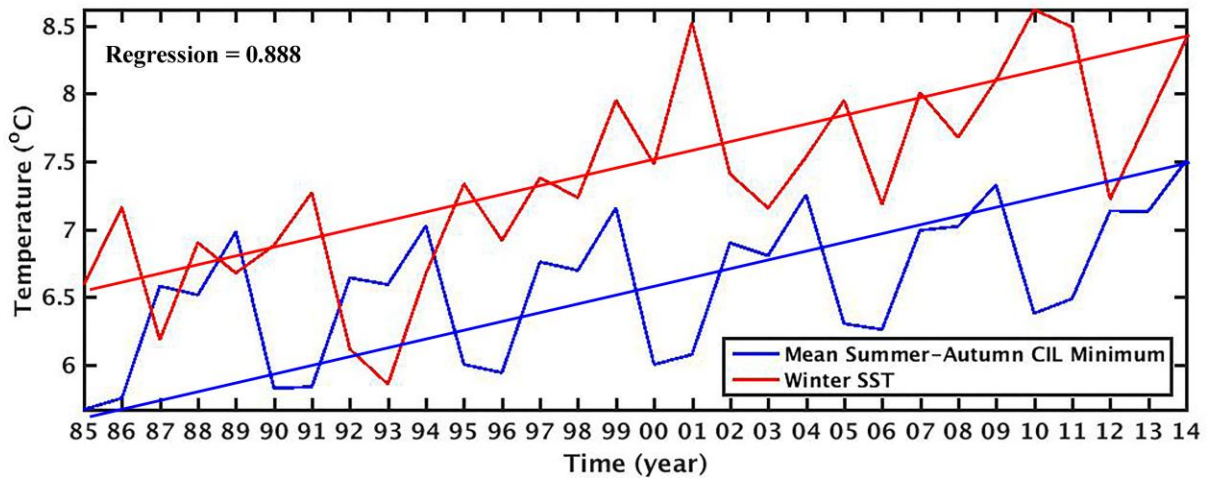
Figure 40: Winter SST warming trend from 1985 to 2014 and the subsequent CIL summer temperature warming trend as a signature of climate change over 30 years.
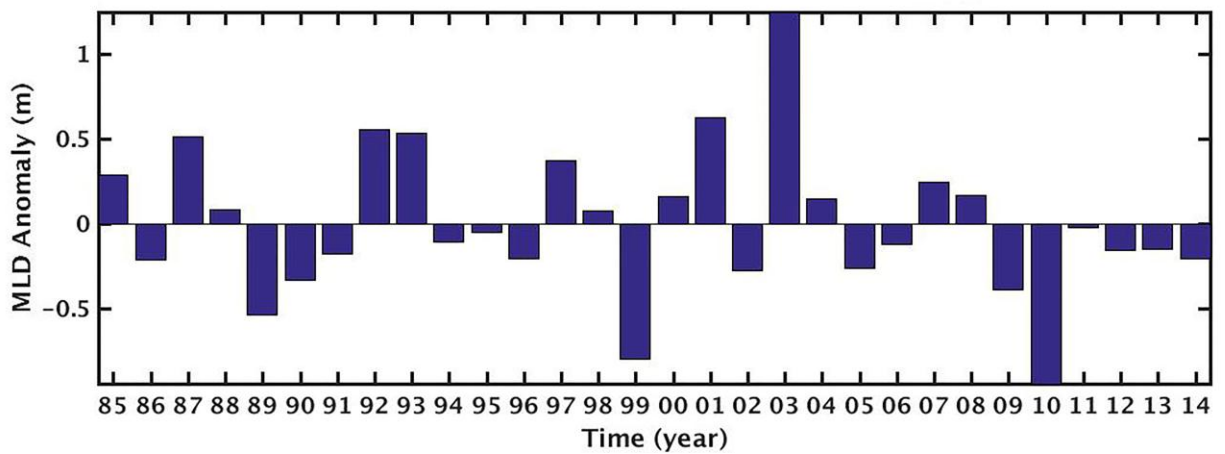
Figure 41: MLD anomaly form1985 to 2014.
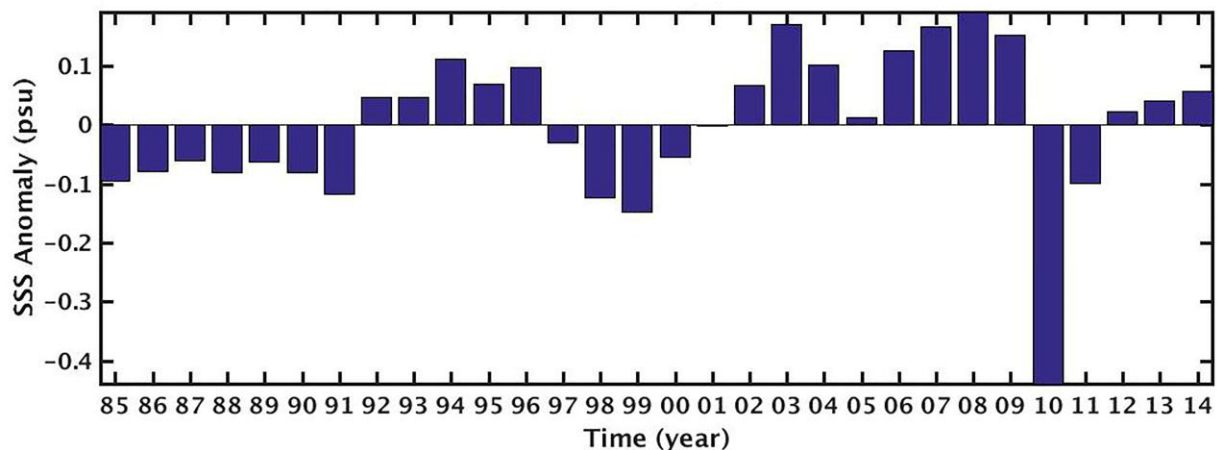
Figure 42: SSS anomaly from 1985 to 2014.

Sea Surface Salinity

Sea surface salinity (SSS) anomaly elucidates periodical variation from 1985 to 2014 (Figure 42). Negative and positive anomalies of SSS are connected to three main parameters determining the Black Sea's salinity: evaporation, river inflow and precipitation. Negative SSS anomalies during periods 1985-1991, 1997-2000 and 2010-2011 indicate that SSS is lower than the mean over 30 years. Referring to variations in the main components influencing salinity, low or negative evaporation anomaly during 1985-1991 may be the main reason for the salt content decrease (Figure 43a). From 1997 to 2000 negative SSS anomaly (Figure 42) may be caused by positive river flux and precipitation anomaly (Figure 43b and c) that counteract a low positive evaporation anomaly. One extreme year is 2010 with the maximum negative SSS anomaly with referring to Figure 43 it is observed that there is a negative evaporation and positive river flux and precipitation anomalies. Similarly, evaporation, river flux and precipitation variations show that the net anomaly (evaporation – precipitation – river flux) is negative meaning that evaporation is less than the sum of precipitation and river flux anomaly which indeed results in lower salinity in years 2010 and 2011. 1992-1996, 2002-2004, 2006-2009 and 2012-2014 are periods with positive SSS anomaly. During these years SSS is higher than the whole period mean. Negative precipitation and river flux anomaly and positive evaporation anomaly (Figure 43a, b and c) result in positive SSS anomaly, keeping in mind that precipitation and river flux play major role in SSS variations in the Black Sea.
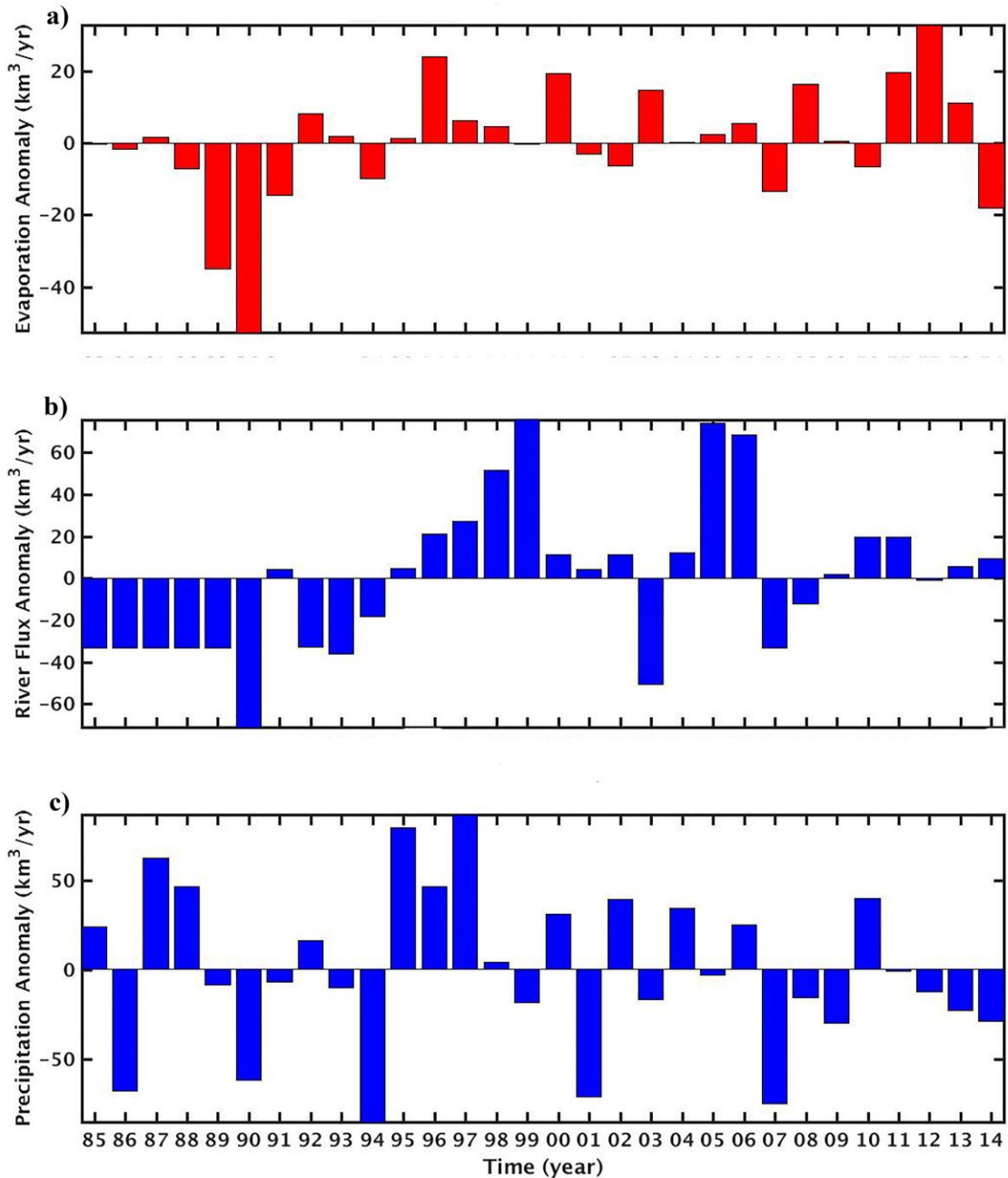
Figure 43: Evaporation (a), river flux (b) and precipitation (c) anomalies from 1985 to 2014.

Considering abovementioned reasons for SSS anomalies, it should be emphasized that over 1985-2014 deviation from mean resides between -0.4395 and +01915 with a mean of -0.1056 for negative anomalies and +0.0924 for positive anomalies, implying that SSS in the Black Sea does not change much and mean of negative and positive anomalies -2.96×10^{-5} indicating that there is almost

no change in SSS in 30 years. This implies that model is able to maintain salt content conserved which returns into conservation of density and hence permanent pycnocline.

15.4 kg/m³ Isopycnal Interannual Variability

The 15.4 kg/m^3 isopycnal is observed as the depth of oxygen minimum (Oguz, 2008; Stanev et al., 2013; Tugrul et al., 2014) and nitrate maximum (Oguz, 2008; Tugrul et al., 2014) in the Black Sea and is of importance for biogeochemical processes. Hence, understanding of interannual variability of this isopycnal gives a clear insight to how it is linked to physical properties. For this purpose, density of seawater is calculated from temperature and salinity model outputs and the depth relating to isopycnal 15.4 kg/m^3 is computed and averaged over the basin. The simulated daily, basin averaged depth of the 15.4 kg/m^3 isopycnal (Figure 44a) shows the depth of the dissolved oxygen minimum and nitrate maximum. Maximum isopycnal depth is 96.7 m on 28 March 1985 and its minimum depth is 75.9 m on 05 September 2009 (Figure 44a). Mean annual isopycnal depth maximum is in 1985 with 95.8 and its minimum is in 2005 with a depth of 77.1 m (Figure 44b). Following CIL shoaling 15.4 kg/m³ has become shallower meaning that density changes are influenced by temperature and salinity changes over the 30 years and temperature variation is the dominant factor in 15.4 kg/m³ isopycnal shoaling. It is inferred that over 30 years there is a displacement of the oxic-suboxic layer toward the surface layer leading to oxygen content decrease in the Black Sea. Daily isopycnal (Figure 44a) shows variations during the whole period. Variation of 15.4 kg/m³ isopycnal from its mean (variance) is 28.8 m. Over the period 1985 to 2014 there is a shoaling of the 15.4 kg/m^3 isopycnal observed that is rather similar to the CIL shoaling (Figure 39) except for the years 2002 to 2004 where almost no annual mean variation (< 10 cm) is observed (Figure 44b). The reason for this stagnation is not clear.
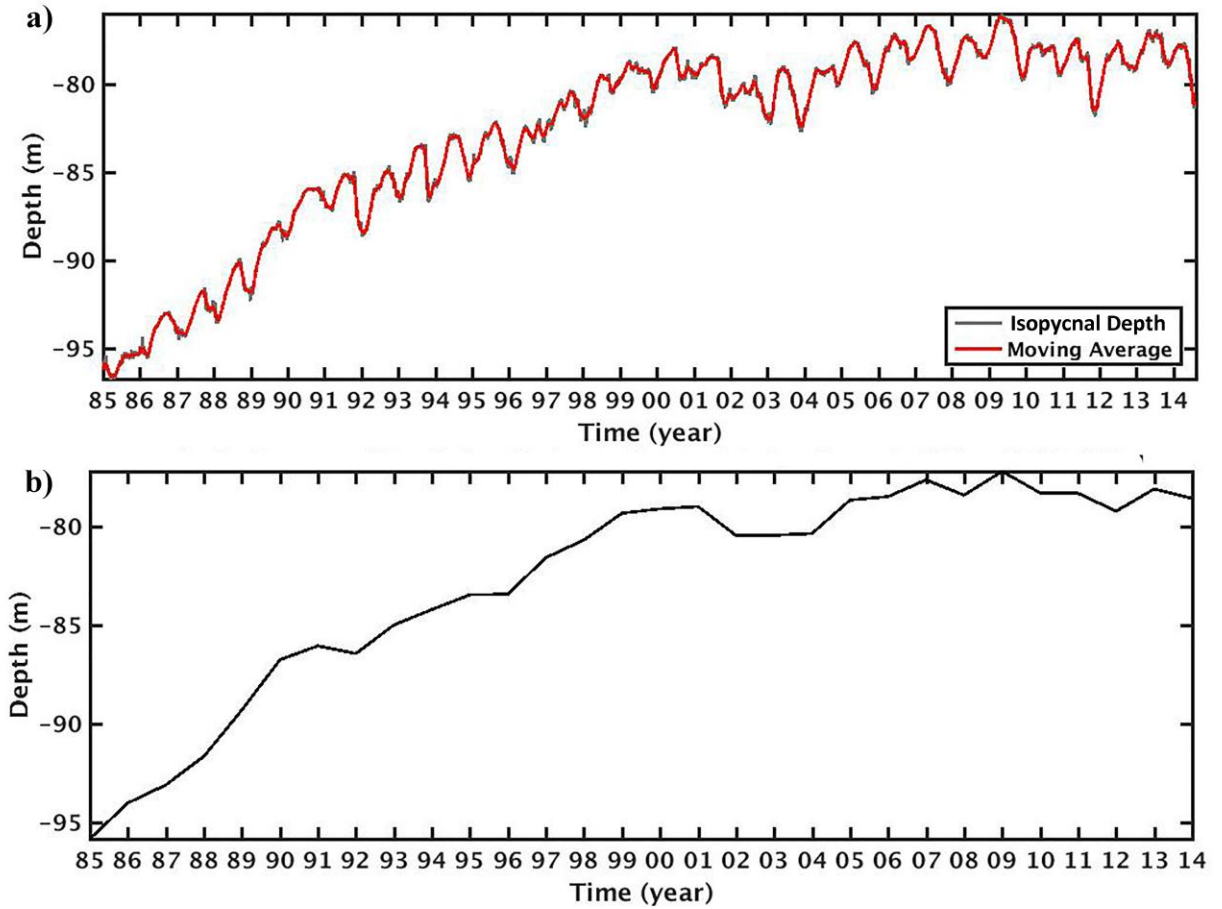
Figure 44: Daily isopycnal (15.4 kg/m³) depth variation from 1985 to 2014 (a) and annual mean isopycnal (15.4 kg/m³) variations from 1985 to 2014 (b).

4.2 Variability in Current Dynamics of the Black Sea

In this section the relationship between wind stress curl and the strength of the Rim Current (ADT-2: second mode of SSH EOF), kinetic energy and the number of eddies present in the Black Sea is investigated in more detail to analyze decadal variations of dynamics of the Black Sea.

As described in 3.4.2 the first mode of SSH EOF (ADT-1) represents mean SSH variations due to changes in the total water budget of the Black Sea (see Figure 35 and Figure 36) while the second mode of the EOF analysis represents Rim Current variability. Variation of wind stress curl and the second EOF spatial mode (ADT-2) shows that a stronger wind stress curl is related to a stronger Rim Current (Figure 45). Wind stress curl variation is followed by ADT-2 meaning that the

Rim Current variations are directly proportional to wind stress curl changes with a positive correlation coefficient of 0.71 representing the wind stress curl as the main driving force of the Rim Current in the Black Sea. Strong winds drive the Rim Current. During winter, wind stress curl and ADT-2 both have their maximum and in summer when winds lose their strength, minimum wind stress curl and ADT-2 values are reached and the Rim Current weakens. Monthly mean climatology of ADT-2 and wind stress curl over the 30-year simulation (Figure 46) show that distributed over the course of a year the times with strong winds and maximum wind stress curl ADT-2 reaches its maximum is during January to March and that wind stress curl is at a minimum from June to September when ADT-2 is also at its lowest magnitude. Similarly, variations of TKE follows wind stress curl variations indicating (Figure 47) that the wind plays the main role in transferring of energy from atmosphere to the ocean. TKE is positively correlated with the wind stress curl with correlation coefficient of 0.68 meaning that wind is the main source of energy in the Black Sea.
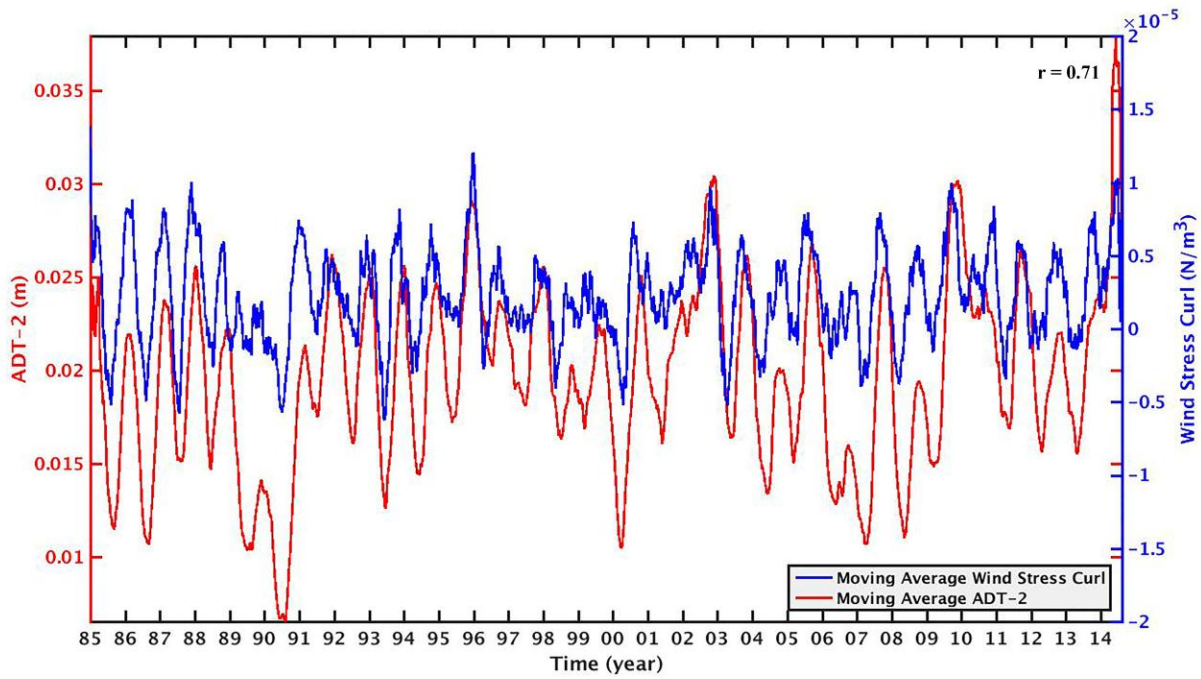
Figure 45: Moving averaged daily varying ADT-2 (EOF mode 2) and wind stress curl (1985-2014).
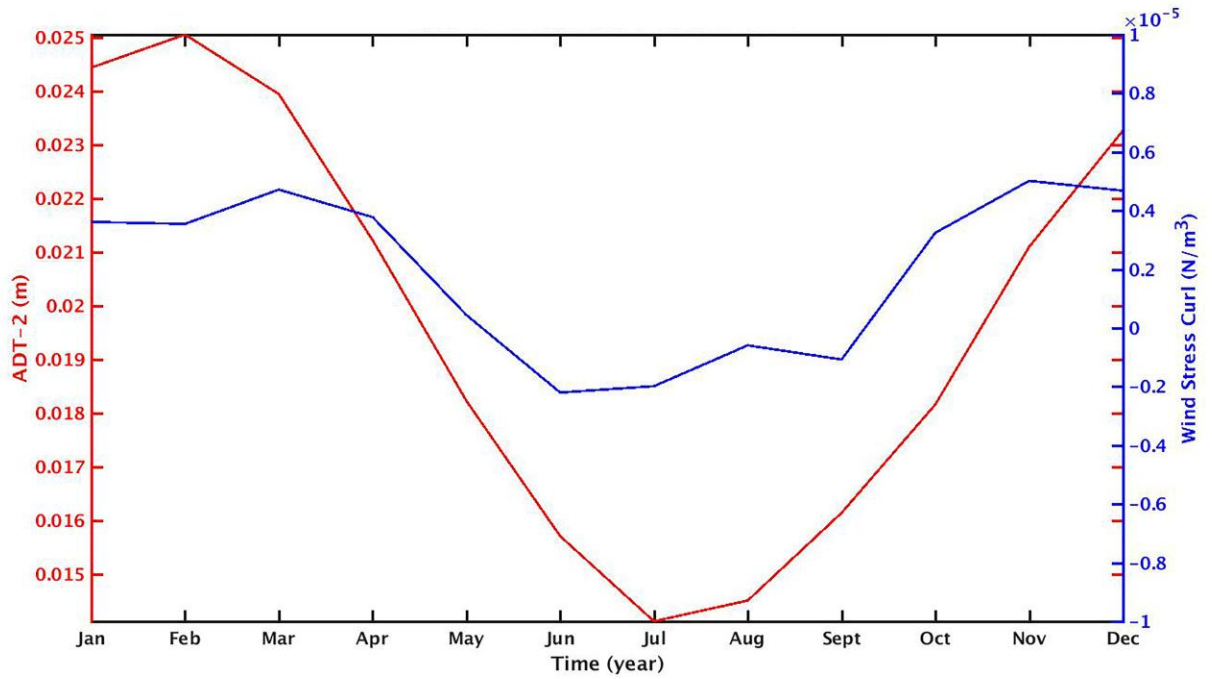
Figure 46: Monthly mean ADT-2 (EOF mode 2) and wind stress curl climatologies averaged over the time 1985 to 2014.
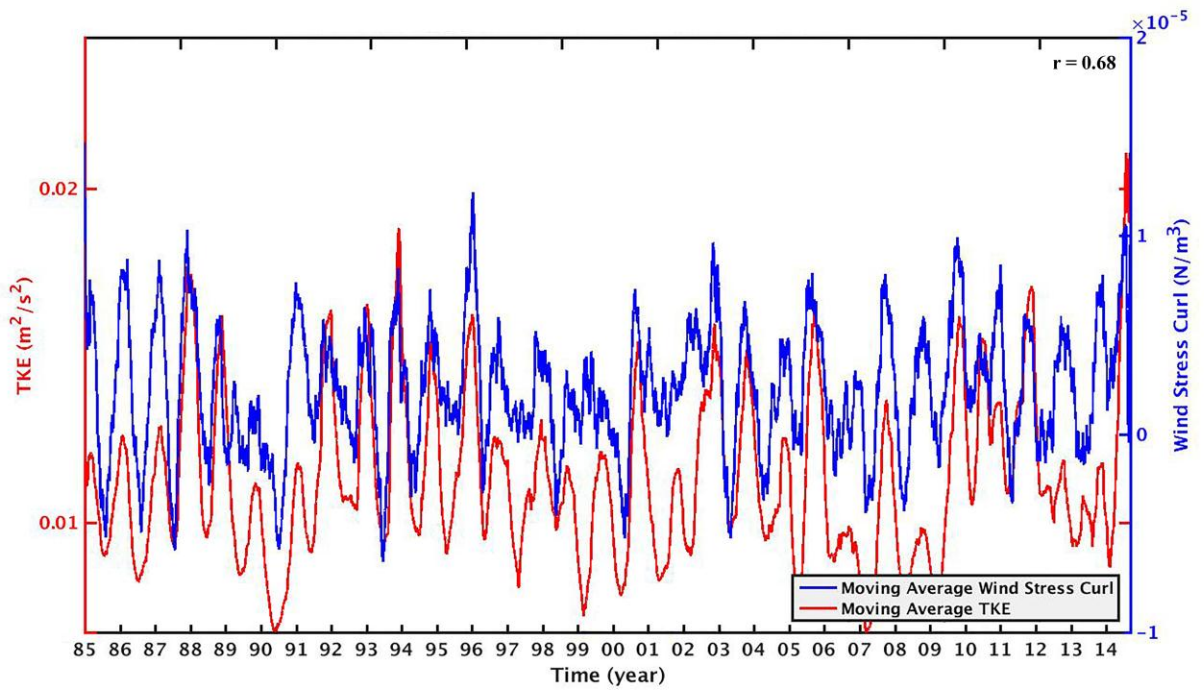
Figure 47: TKE and wind stress curl from 1985 to 2014. TKE is positively correlated with the wind stress curl.

Daily varying MKE (Figure 48a, blue line) and TKE (Figure 48b, blue line) are well correlated with ADT-2 (red line) with a correlation coefficient equal to +0.60 and +0.69, respectively. This is in line with the fact that wind stress curl is the main driving force of the Rim Current. The mean atmospheric circulation has a cyclonic pattern throughout the year which provides a positive wind stress curl which is maximum in winter and minimum in summer (Korotaev et al., 2001). The positive wind stress curl and the buoyancy contrast between the freshwater from rivers and Mediterranean saline underflow into the Black Sea through the Bosphorus Strait induces the Rim Current leading to a large TKE and MKE. Stronger winds create stronger currents and consequently larger kinetic energy (Figure 48). Both MKE and TKE are wind force dependent and maxima and minima of the two parameters strongly follow wind forcing variations and ADT-2 as the signature of the Rim Current. MKE and TKE gain their maxima during a strong Rim Current in winter of each year and as Rim Current weakens MKE and TKE have their minima (Figure 48a and b).

Total number of eddies (cyclonic and anticyclonic) in the Black Sea is inversely proportional to the strength of the Rim Current (ADT-2) with a negative correlation coefficient (r = -0.45) (Figure 49). In winter when strong prevailing winds are present the Rim Current is dominant with semi-permanent anticyclonic eddies between the Rim Current and continental shelf. As winds weaken in spring and summer and consequently, the Rim Current weakens, and the number of eddies increase. Hence, in winter during strong Rim Current the number of eddies decrease and in spring and summer as the Rim Current disappears number of eddies increase. Figure 49 clearly shows number of eddies reaches its minimum when ADT-2 is maximum. As MKE and TKE variations are directly proportional to ADT-2, this relationship is also applicable about MKE and TKE variations with the number of eddies. Analysis shows that the maximum number of eddies is observed when MKE reaches its minimum value (Figure 50). Number of eddies is negatively correlated with MKE with a correlation coefficient equal to 0.52. Hence, while wind, the main force driving water movement weakens, MKE decreases and ultimately in summer reaches its minimum resulting in weakening of the Rim Current and its disintegration into eddies. This reverses in winter period when strong winds are dominant MKE gains its maximum value resulting in formation of the Rim Current and finally a decrease in the number of eddies. Consequently, total number of eddies and MKE are inversely proportional.
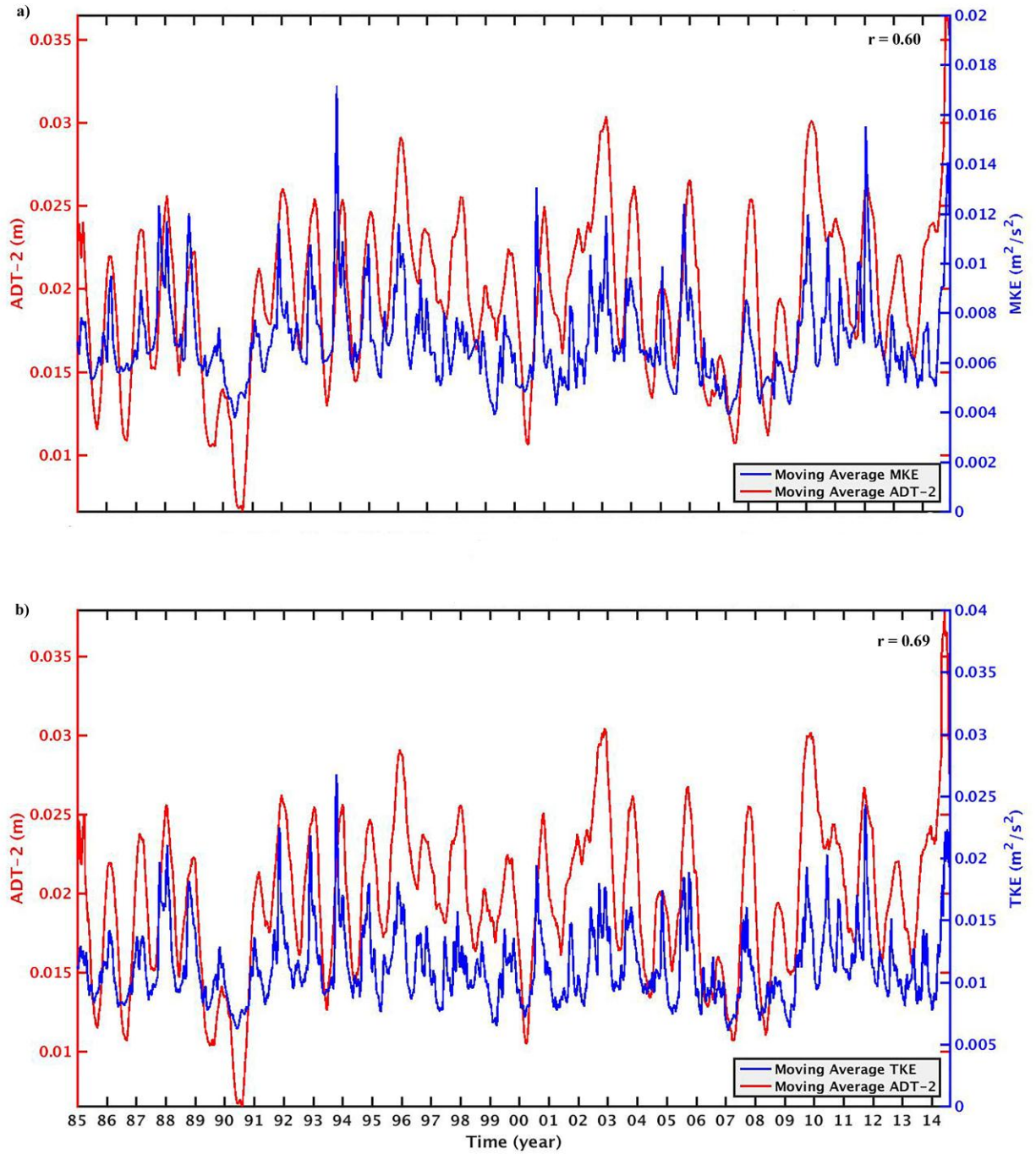
Figure 48: Moving averaged daily varying ADT-2 and MKE and TKE (1985-2014).
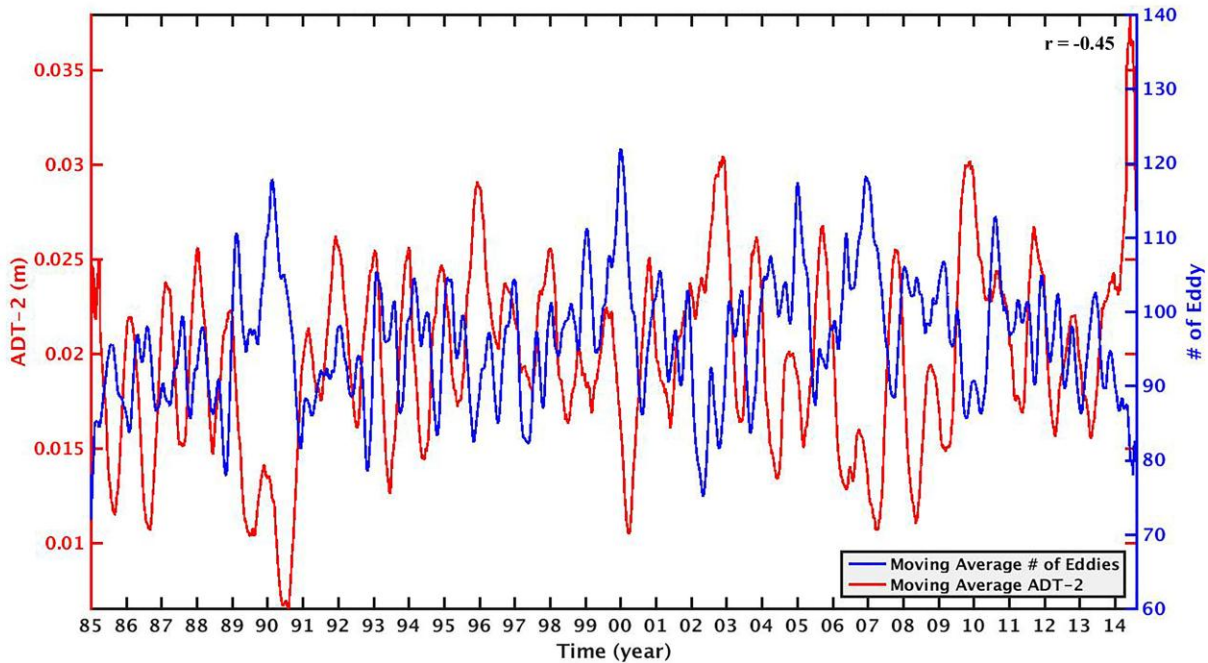
Figure 49: Moving averaged daily varying ADT-2 (EOF mode 2) and number of eddies.

Decrease and increase of the MKE results in generation and disappearance of eddies (Figure 50), respectively, meaning that the number of eddies and MKE are inversely proportional. Likewise, the abundance of cyclonic and anticyclonic eddies is inversely proportional to EKE (Figure 51). Kinetic energy is directly dependent on the wind. Although the number of cyclonic and anticyclonic eddies present in the Black Sea during winter is less than summer period, strong winds transfer energy to the ocean leading to the larger magnitude of the kinetic energy. As wind weakens in spring and summer kinetic energy decreases and as a consequence of the Rim Current weakening number of eddies increase. However, despite large number of eddies generation in the Black Sea at that time their energy is low because of the weak transfer of energy from atmosphere to the ocean and the dissipation of the kinetic energy already present in the system. As it will be shown in section 4.3 this is in contrast to late winter and early spring, when the weakening of strong winter winds weakens the Rim Current that disintegrates into eddies which have higher velocities, inherited from the Rim Current. In the time period after generation these eddies they lose their energy from April to August and as winds strengthen from the end of summer increasing trend in EKE is observed (Figure 52). Eddy kinetic energy is negatively correlated with the total number of eddies with a correlation coefficient of r = -0.18 (Figure 51) meaning that although the number of eddies increase during disintegration of the Rim Current they are not as energetic because EKE is low, which indicates no correlation.

88
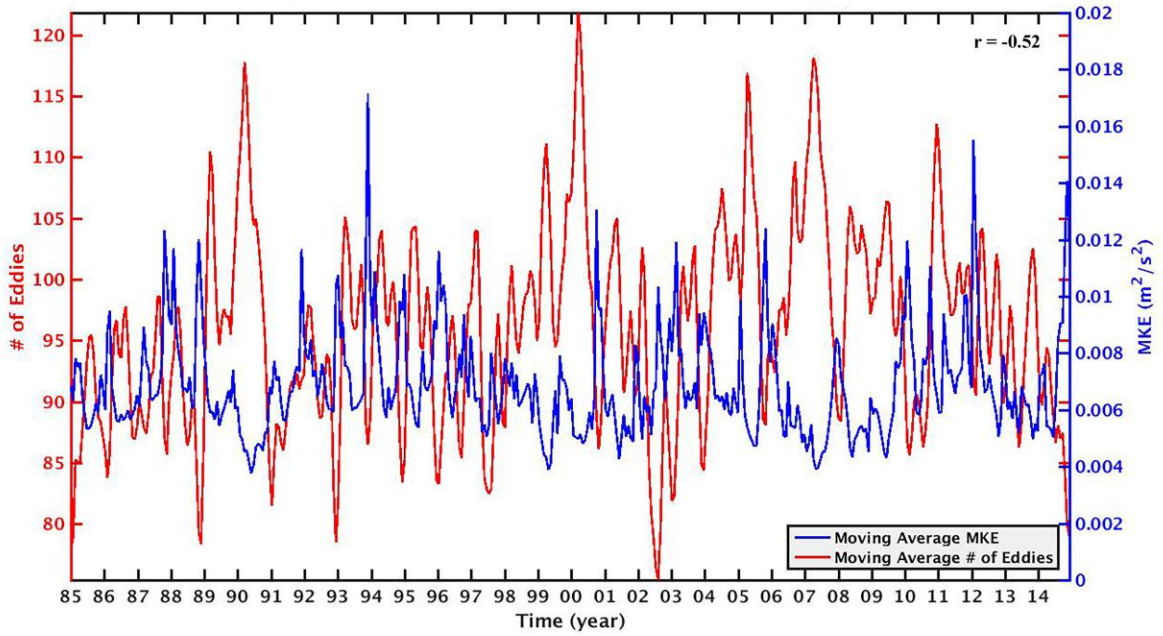
Figure 50: MKE and total number of eddies variation from 1985 to 2014.
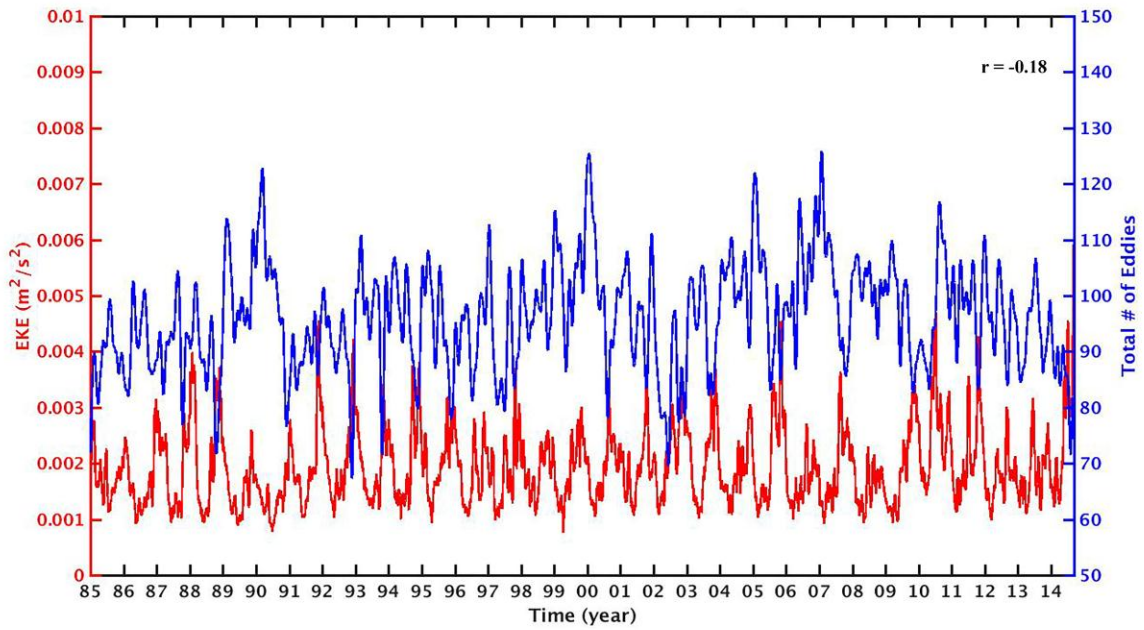
Figure 51: EKE and total number of eddies variation from 1985 to 2014.

Monthly mean eddy kinetic energy climatology over the 30-year simulation illustrates in more detail how kinetic energy of eddies has its maximum in winter and its minimum occurs in summer (Figure 52) indicating that decrease of energy transfer from atmosphere to the ocean highly influences EKE following TKE and MKE variations.
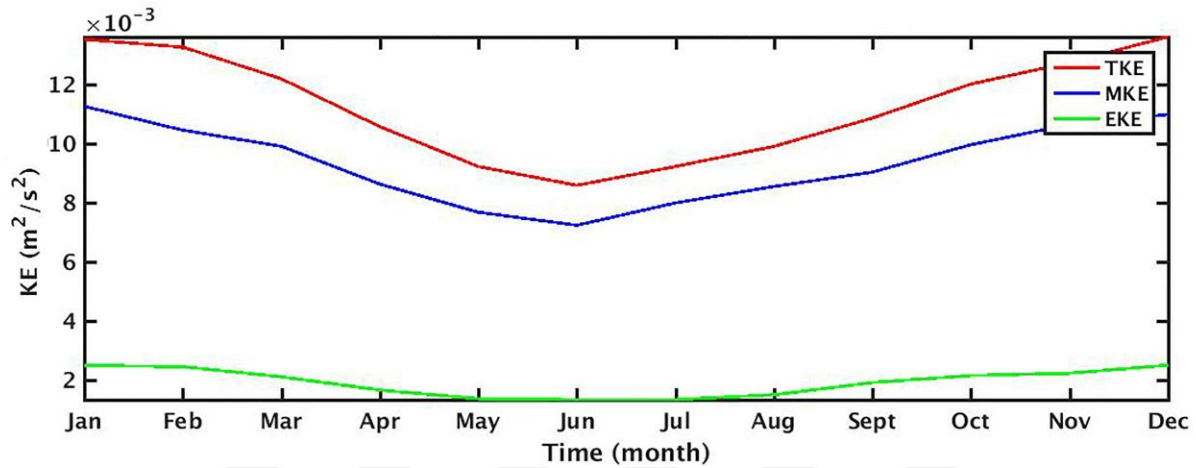
Figure 52: Mean monthly climatology of TKE, MKE and EKE averaged over the time 1985 to 2014.

4.3 Horizontal and Vertical Water Transport Dynamics in the Black Sea

After a thorough analysis of the interactions between wind, kinetic energy and current dynamics above in section 4.2, the horizontal and vertical mixing dynamics within the Rim Current in the southern Black Sea during three different months (January, March and May) is detailed in the following section. Results will disclose the role of large and mesoscale features in cross-shelf transport in different periods.

To investigate the role of eddies for horizontal and vertical transport of water and with it nutrients or any other tracer from the coast to the interior basin and from surface to bottom, a box has been considered at 42.09 °N and 33.20 °E, close to Belyaka to Inceburun near Sinop at 42.09 °N 34.92 °E in the coast toward the sea at 42.54 °N and 33.20 °E to 42.54 °N and 34.92 °E (see Figure 1). In both horizontal and vertical directions the velocities, and consequently the fluxes into the box, are calculated from the surface to the bottom of the box, that was defined as the depth of the 15.4 kg/m^3 isopycnal, to study seasonal changes of the fluxes entering the box and their variability with respect to the Rim Current and eddies present in the box region.

The x- and y-components of horizontal fluxes variations (Figure 53) show that in the horizontal direction the volume of water into the box in x direction is negatively correlated with the volume of water that passes into the box in the y direction with a correlation coefficient of r = -0.169, which indicates no correlation. It can be seen that the x-component of horizontal flow into the box is larger than the y-component meaning that volume of water passing through the box area is larger in the Rim Current path. Consequently, the flux volume transport is strongly dependent on circulation patterns and dynamics of the Black Sea. Negative correlation coefficient shows that water flux transport in x-direction opposes the transport in y-direction but it is not necessarily always opposite.
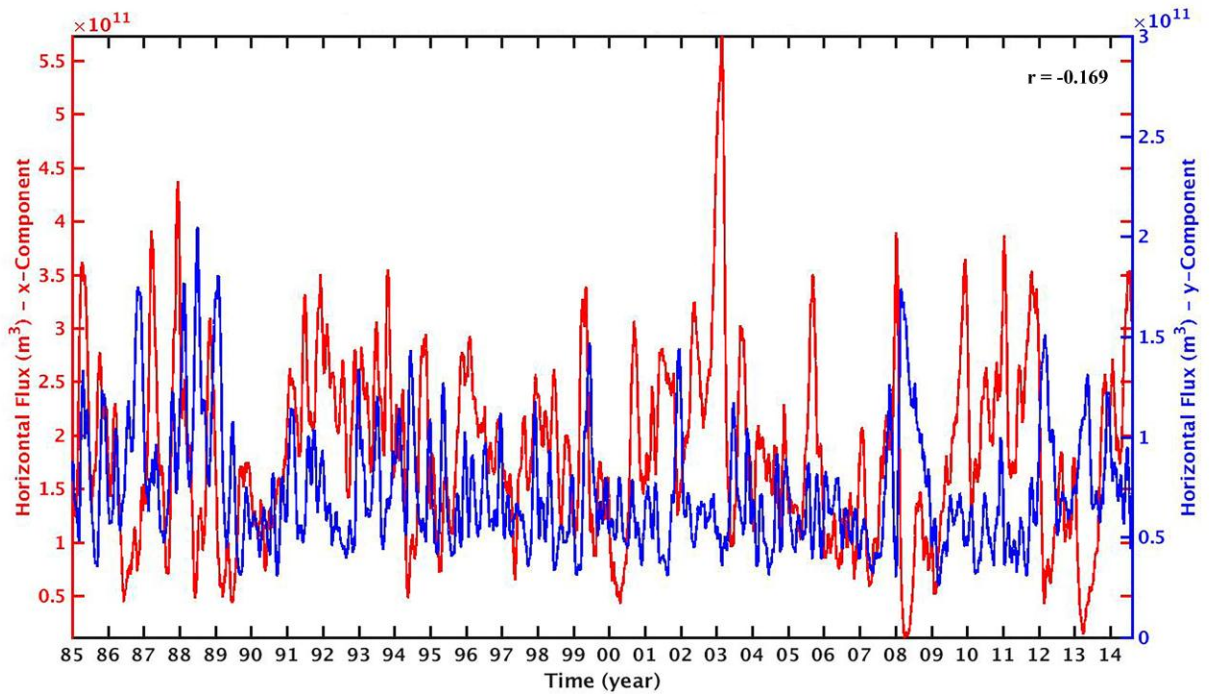
Figure 53: Basin averaged x- and y-components of horizontal fluxes temporal variation from 1985 to 2014.

Monthly mean climatology of the horizontal flux into the box, integrated from bottom of the box to the surface, illustrates that the volume of water entering the box reaches its maximum in winter (Figure 54), specifically in January and February at the time of strong Rim Current presence where velocity x-component reaches its maximum. In the vertical, the volume of the water transported is less than in the horizontal but similar seasonal changes are observed (Figure 55). In winter, stronger winds (southwestern and northeastern) result in higher vertical velocities and the volume of water transported upward into the box is maximum. This transport is enhanced by Ekman pumping as well as other dynamical features such as eddies and filaments. Mean monthly climatology of vertical flux

91

(Figure 56) reveals that in winter (January to March) vertical flux transported upward into the box reaches its maximum and in summer (July to September) the volume of water transported upward is minimum due to reduced wind stress. It increases again in autumn (October to December). In addition, the monthly mean climatology of Ekman pumping velocities shows larger velocities in January to March and October to December indicating upwelling of subsurface water due to Ekman pumping which is the signature of vertical transport of water (Figure 57). This variation is similar to volume flux variation proving the fact that Ekman pumping plays a major role in Black Sea circulation. This fact indicates the role of Ekman pumping as an important driver of upper layer circulation of the Black Sea, which has also been noted by Kubryakov et al., (2016). As winds get weaker and the Rim Current disappears velocity mitigates and therefore the volume of water transported into the box decreases and reaches its minimum in late spring and summer.
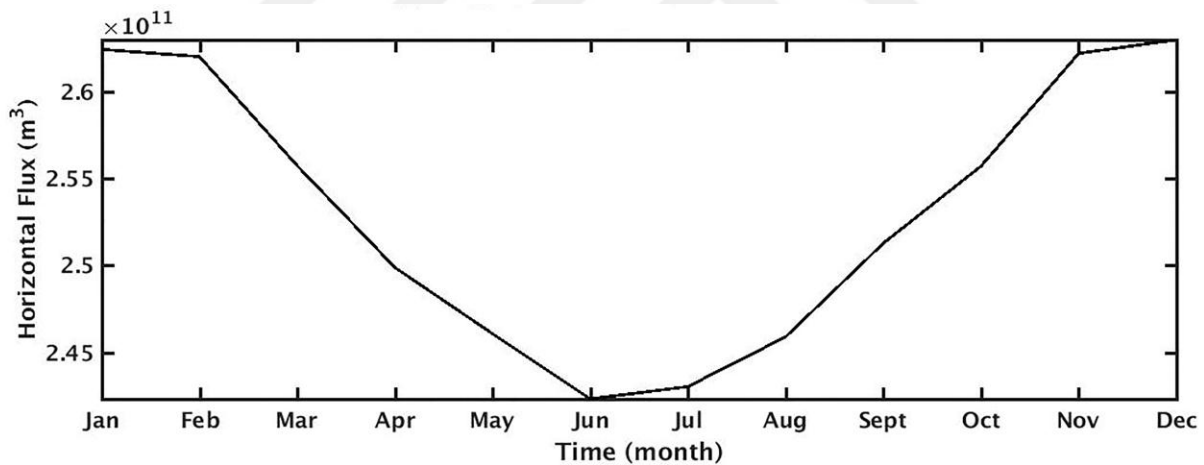
Figure 54: Monthly mean horizontal flux climatology (sum of horizontal fluxes in both x- and y-components) averaged over the time1985-2014.
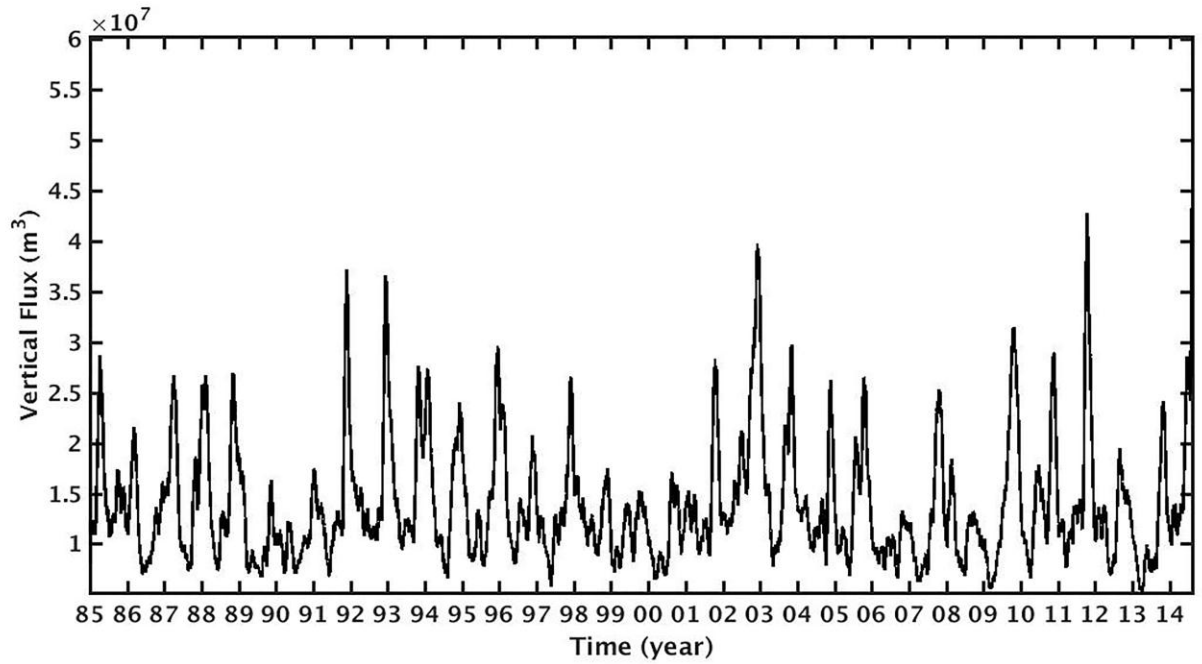
Figure 55: Basin averaged vertical flux temporal variation from 1985 to 2014.
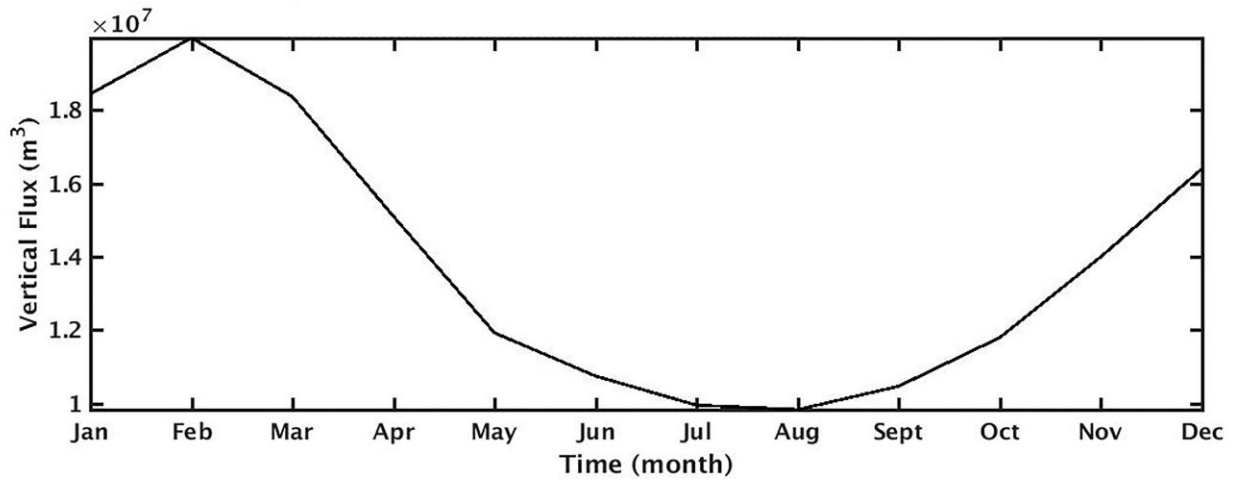
Figure 56: Monthly mean climatology of vertical flux averaged over the time 1985 to 2014.

93
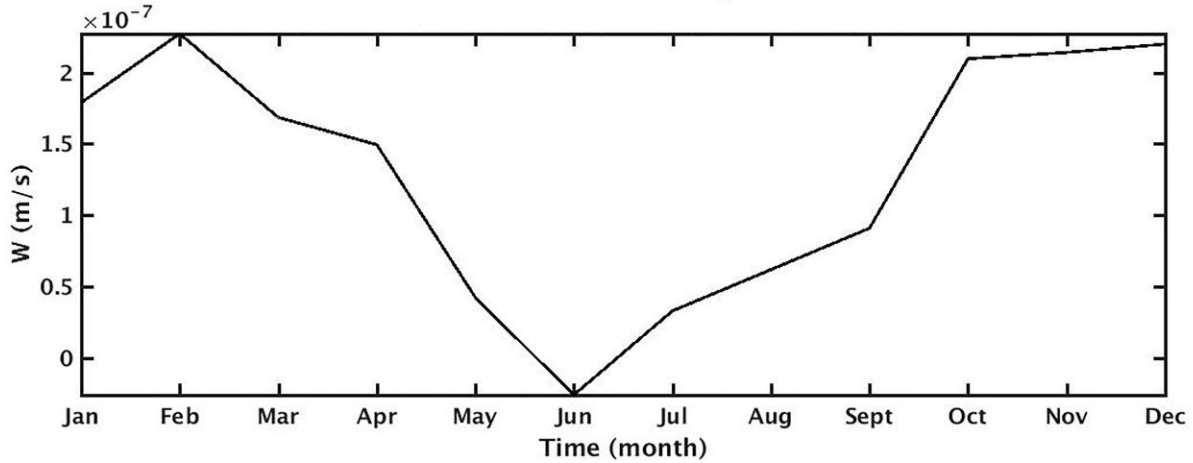
Figure 57: Monthly mean climatology of Ekman pumping velocity averaged over the time 1985 to 2014.

Further investigation shows that volume transport into the box in x-direction is positively correlated with ADT-2 (Rim Current mode) with a correlation coefficient of 0.64, proving that the x-component which carries water masses into the box, strengthens and weakens following the Rim Current variations (Figure 58a). At the times that ADT-2 reaches its minimum indicating a weakening of the Rim Current, the volume of the water transported into the box reduces accordingly (Figure 58a). In the y-direction this reverses meaning that maximum ADT-2 is proportional to the minimum y-component of the horizontal flux (Figure 58b). However no correlation is found between ADT-2 and y-component of the horizontal flux. Consequently this means that when the Rim Current is not dominant the horizontal transport from the continental shelf to interior basin does not increase. One reason for this reason could possibly be the longer period of less energetic eddies presence in the region (May to September), meaning that these eddies move slower than their generation time when they are energetic (March and April). However, it can be concluded that in the periods of strong Rim Current northward transport of water decreases and hence, transport of nutrients from coast to the interior basin are inhibited by the strong Rim Current.

Following above analysis and in an effort to investigate horizontal and vertical fluxes and their relation to the presence of eddies in more detail, three different dates are randomly chosen considering TKE magnitudes (Figure 48b) and Black Sea dynamics. Representing high TKE, 11 January 2008 was chosen, representing a time with strong Rim Current (Figure 59a left) including a strong eastward flow (Figure 59a right). Representing the time at which TKE is decreasing from its

maximum to its minimum when eddies are generated, 01 March 2008 was chosen (Figure 59b left) and the transport in the study area is influenced by these eddies (Figure 59b right).
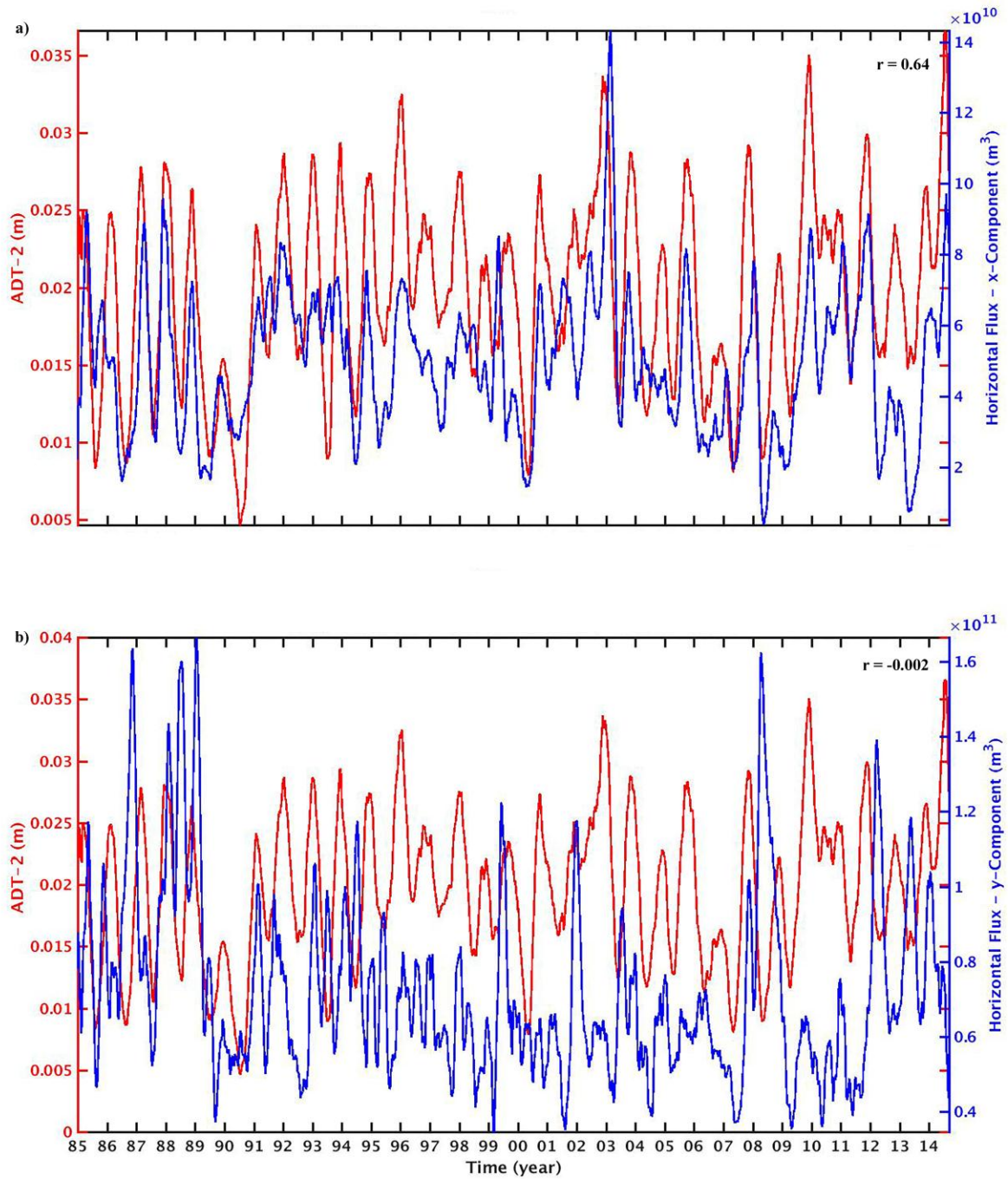
Figure 58: ADT-2 variations in comparison to horizontal flux variations in x-direction (a) and y-direction (b) into the box depicted in Figure 1 from 1985 to 2014.

As a representation of a weak Rim Current and its decomposition into mesoscale eddies the 01 May 2008 was chosen (Figure 59c). To study transport mechanisms impact, horizontal (x- and y-components) and vertical (z-component) components of velocity are compared in both zonal (west-east) and meridional (south-north) directions.

The zonal and meridional plots of velocity x-components (Figure 60a and d) show that at the time of a strong Rim Current u-velocities are dominant with high magnitudes, transporting nutrients and tracers eastward in the zonal direction. Transport from the continental shelf towards the inner basin is confined to the width of the Rim Current, meaning that northward transport is dependent on the Rim Current extension from coast to the north. Accordingly, zonal and meridional transect plots of v-velocity (Figure 61 a and d) confirm that at the time of strong Rim Current the y-component of velocity is weak and there is only little northward or southward transport proving that in winter and in times with high TKE the Rim Current plays the major role in the transport of nutrients and water masses eastward and it acts as a barrier preventing northward transport of water masses toward interior basin

The second case, when TKE is decreasing and Rim Current starts losing its energy and eddies are formed (Figure 59b) zonal transect of u-velocity (west to east direction) shows that the transport direction depends on the anticyclonic eddies orientation (Figure 60b and e). On the northern and southern parts of anticyclonic eddies the x-component of velocity is dominant and in the opposite direction (west to east transport in the northern edges of an anticyclone and east to west in the south edge of the eddy). In the west and east edges of the eddy y-components are stronger and the transport is carried northward on the left and southward on the right wall of the eddy. This pattern is reversed for cyclonic eddies. Consequently, when eddies are present both types of transport occurs, zonal and meridional (Figure 60b and e and Figure 61b and e).

In the third case (01 May 2008), when the Rim Current is decomposed into eddies, wind speed is low and hence there is little transport of energy from atmosphere to ocean Figure 59c). Velocity of the eddies is not large and they are not energetic (Figure 59c). In addition, in this particular simulation year the Sinop eddy is present and part of it always exists in northeast of the box. However, in comparison to the two previous cases zonal and meridional x- and y-component of velocity (Figure 60c and f) are very small and in meridional transect plots (Figure 60f and Figure 61f) even zero velocities are observed. This indicates that any horizontal (zonal or meridional) transport is energy dependent. Larger transfer of energy from atmosphere to ocean enhances and facilitates the transport in the ocean.
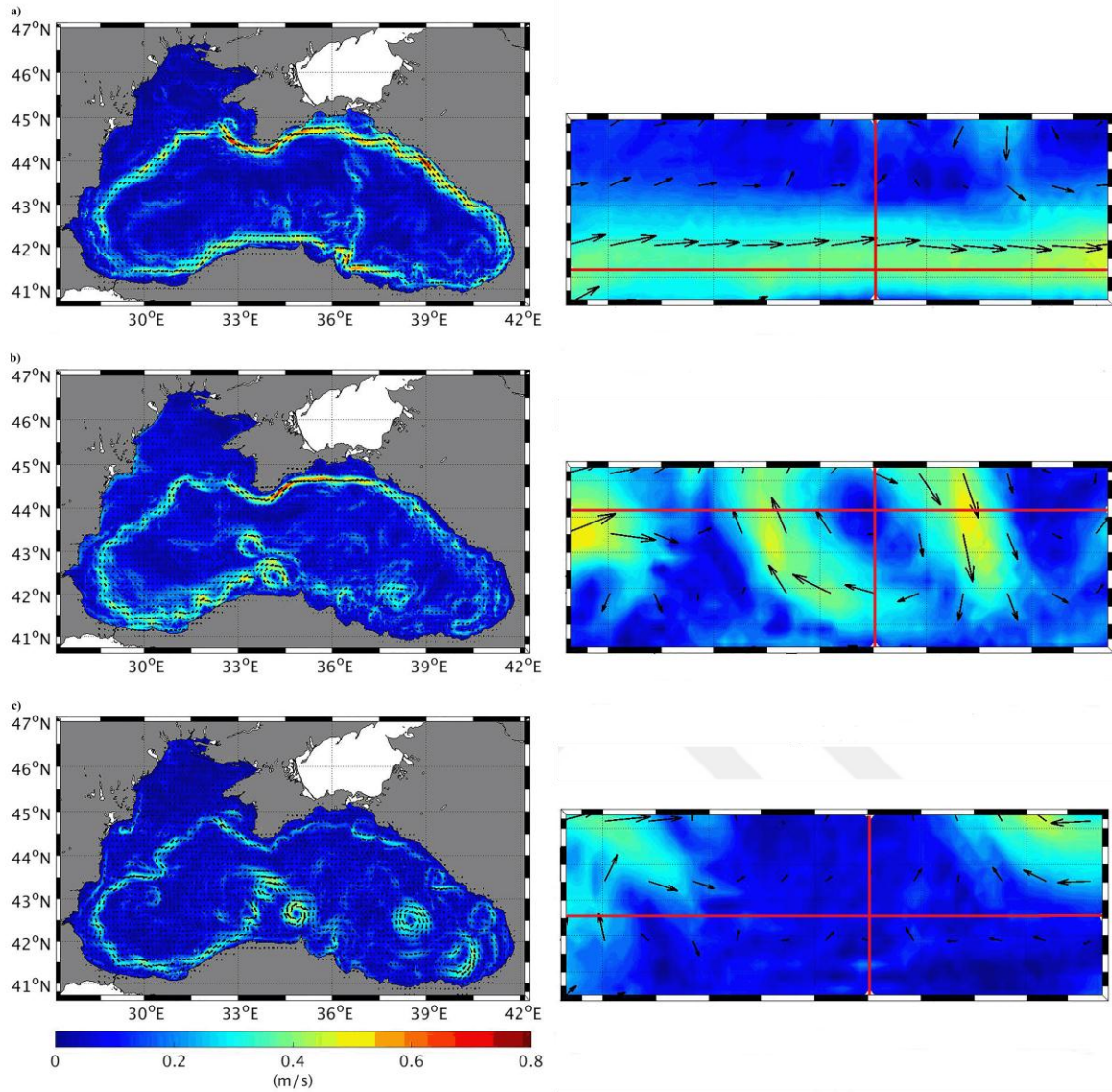
Figure 59: Circulation pattern on 11 January 2008 with strong Rim Current present in the Black Sea (left) and zoomed into the box depicted in Figure 1(right) (a), 1 March 2008 strong eddies presence in the Black Sea (left) and zoomed into the box depicted in (b), 1 May 2008 weaker eddies presence in the Black Sea (left) and zoomed into the box depicted in Figure 1 (c).
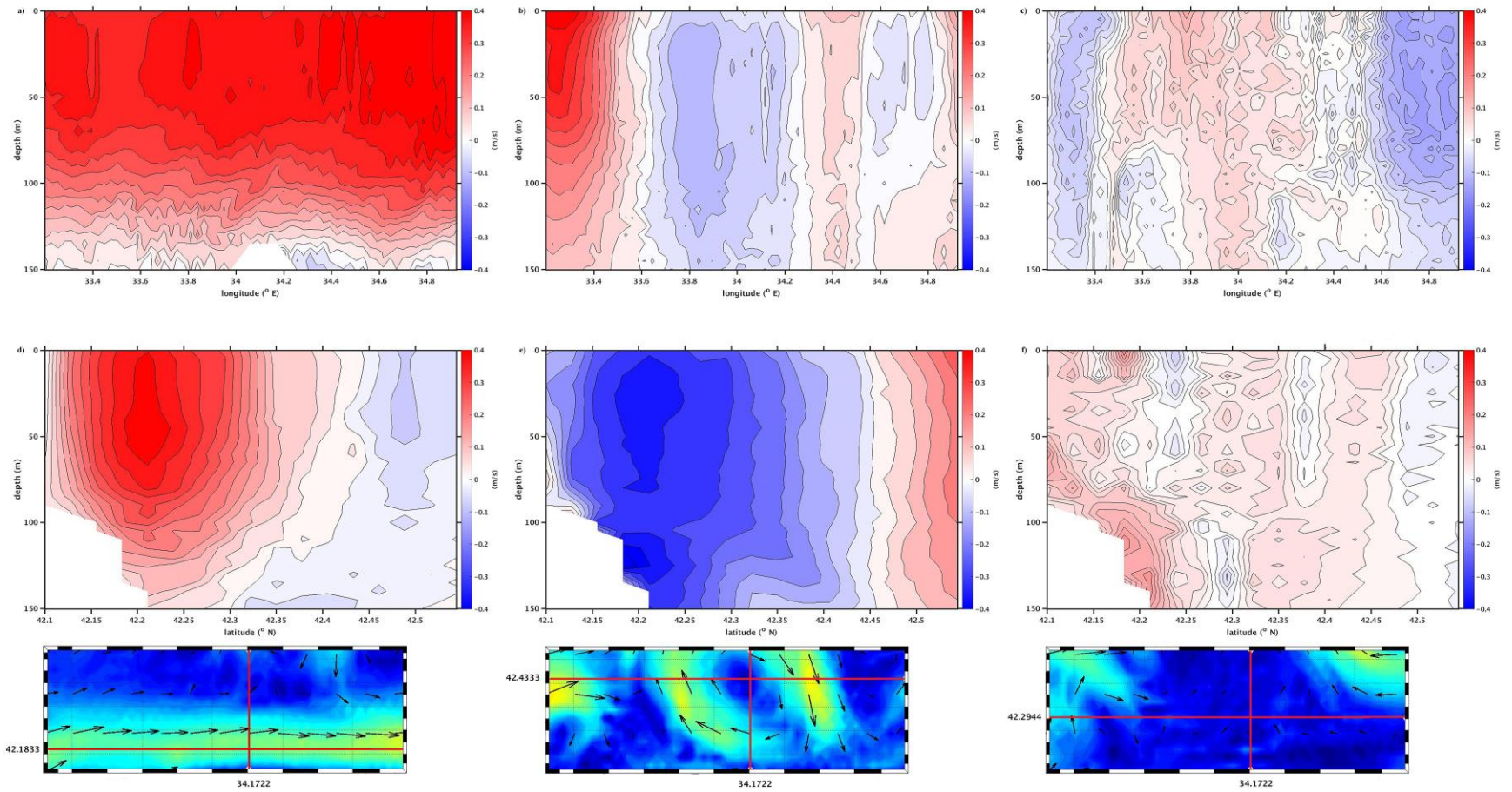
Figure 60: Zonal transect of horizontal velocity (velocity x-component) transect for 11 January 2008 (a), 1 March 2008 (b) and 1 May 2008 (c) and meridional transect of horizontal velocity (velocity x-component) transect for 11 January 2008 (d), 1 March 2008 (e) and 1 May 2008 (f).

98
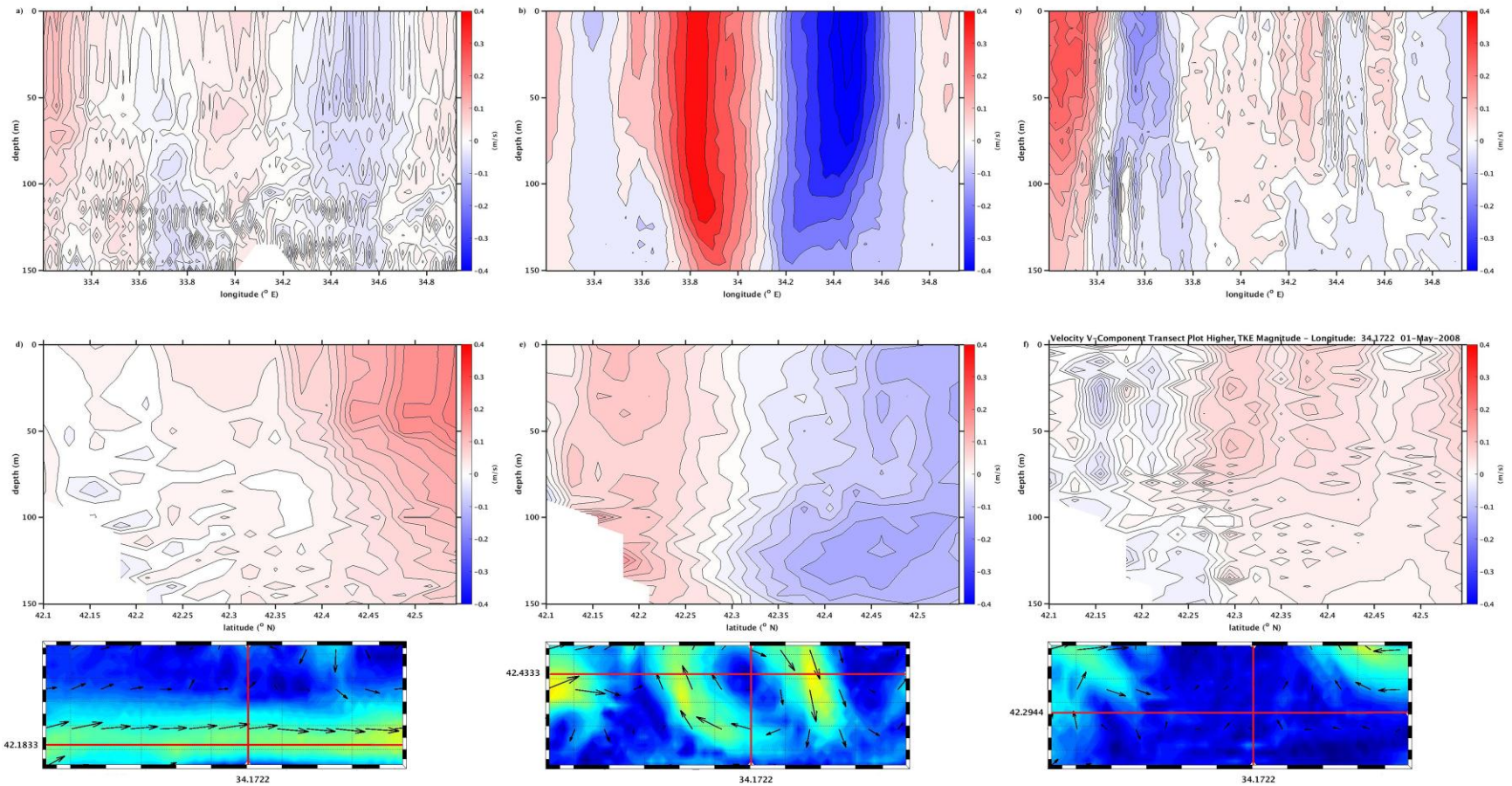
Figure 61: Zonal transect of horizontal velocity (velocity y-component) transect for 11 January 2008 (a), 1 March 2008 (b) and 1 May 2008 (c) and meridional transect of horizontal velocity (velocity y-component) transect for 11 January 2008 (d), 1 March 2008 (e) and 1 May 2008 (f).
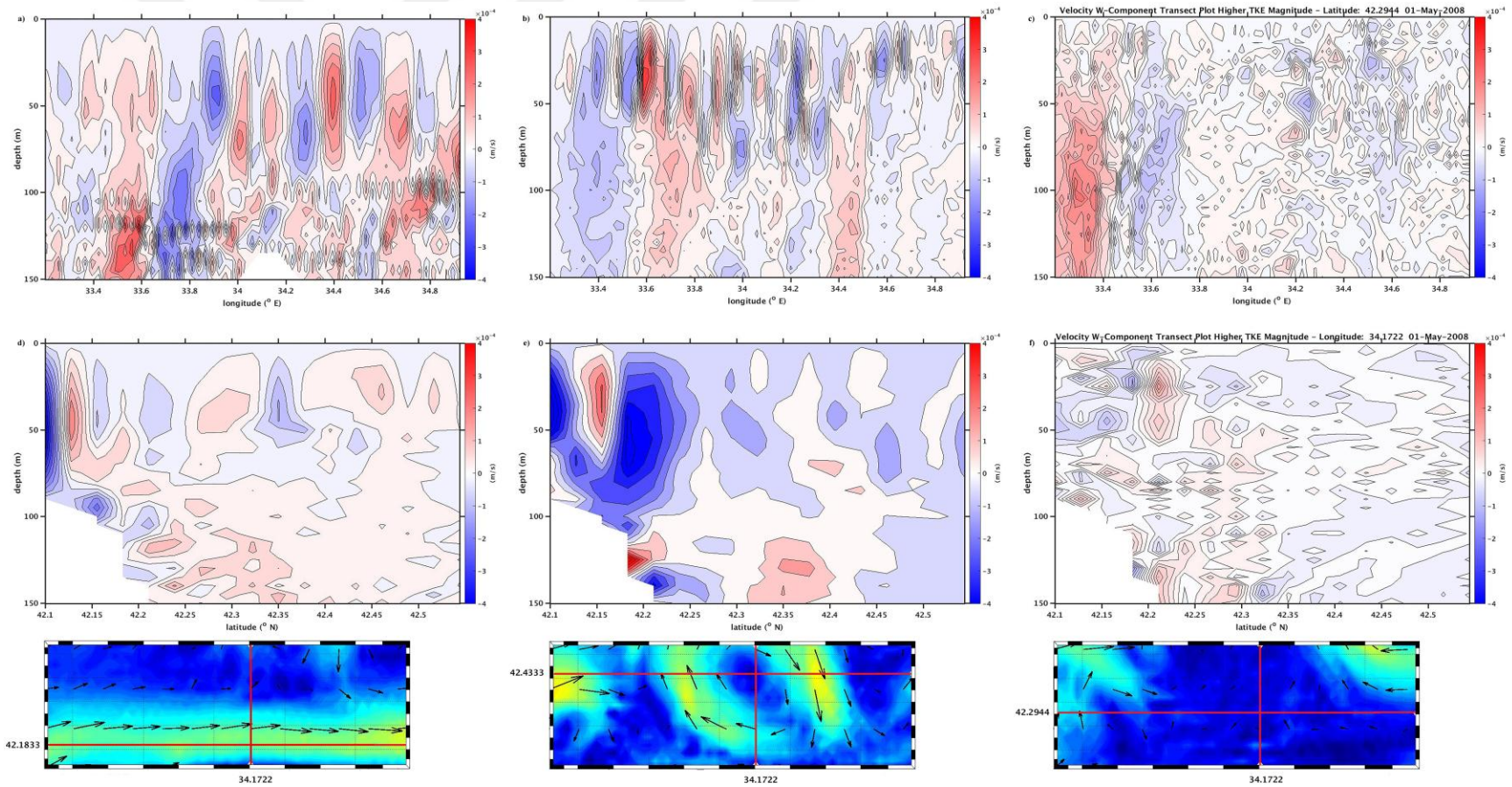
Figure 62: Zonal transect of vertical velocity (velocity z-component) transect for 11 January 2008 (a), 1 March 2008 (b) and 1 May 2008 (c) and meridional transect of vertical velocity (velocity z-component) transect for 11 January 2008 (d), 1 March 2008 (e) and 1 May 2008 (f).

Vertical velocity transect plots for strong Rim Current and energetic eddy cases confirm that higher energy transfer not only highly influences horizontal (both zonal and meridional) transport processes but also it exacerbates vertical velocities, leading to upward and/or downward transport of water masses Figure 62a, b, d and e. Upward and downward velocities (zonal and meridional) in the third case (01 May 2008) show that as energy decreases and eddies are weakened vertical velocities are strongly reduced such that states of no motion (w = 0) are formed in water column which is a signature of strong stratification in late spring and summer (Figure 62c and f). In Figure 62c larger upward velocity is observed at the coast which is most probably due to Ekman pumping phenomena which pumps deeper water masses to the surface. Other than that no significant vertical water transport is observed. In the case of Strong Rim Current and energetic eddies (Figure 59a and Figure 59b) stronger vertical velocities are in zonal direction meaning that upwellings and downwellings almost occur in west to east (or east to west) direction while this is not seen in the third case (Figure 59c).

CHAPTER 5

DISCUSSION

The Black Sea NEMO model presented in this study produces consistent results with several modeling studies described in the literature. However, its major and the most important advantage and difference, which makes it be unique, is the implementation of the Bosphorus Strait as an unstructured boundary condition providing the two layer flow into and out of the Black Sea along with its high resolution. In previous modeling studies of the Black Sea Bosphorus Strait is described as a negative river discharge (Staneva et al., 2001; Grayek et al., 2010; Shapiro et al., 2013; Zhou et al., 2014; Cannaby et al., 2015; Miladinova et l., 2017) and only in few modeling studies Bosphorus Strait has been parameterized as a two layer flow (e.g. Capet et al., 2012). This advantage ensures conservation of the Black Sea water budget and total salt content and is required to sustain the halocline. Newtonian damping (nudging) of temperature and salinity used for conservation of the pycnocline over the 30 years in the model was necessary to counteract the weakening of the strong density gradients originating from numerical errors in the form of diffusion regardless of the Bosphorus implementation. Univariate and multivariate validation of physical properties described in Chapter 3 shows that model is able to compute physical properties of the Black Sea and capture seasonal and interannual variabilities which are of Black Sea's well-known characteristics. Overall correlation coefficient of 0.84 and 0.86 for temperature and salinity, respectively, indicates that model is in good fit with measured in-situ data. The high resolution of the model (3 km $\times$ 3 km in horizontal and 61 z-levels in vertical) enables reproduction of the ocean mesoscale processes, fronts and filaments at a level statistically consistent with observations. This specification of model provides a realistic simulation of the Black Sea physical properties (e.g. temperature, general circulation including Rim Current and mesoscale features, CIL, sea level) in the long term (1985-2014).

Simulations show that the bottom boundary of the CIL, a permanent feature of vertical stratification in the Black Sea, is found between 140 m to 100 m in 1985 and 2014, respectively with a shoaling of its depths and hence decrease in its thickness from 133.3 m to 66.7 m with a mean thickness of 97 m. This is in agreement with findings of Akpinar et al., (2017) and Stanev et al., (2019). Shoaling of the CIL displaces oxic, suboxic and anoxic layers boundaries and consequently, influences oxygen concentration and biogeochemical processes in the Black Sea. Interannual variations of oxygen renovations in CIL lead to changes of the anoxic boundary position in the

density field (Podymov et al., 2011). Shoaling of the CIL is identical to its thinning. As CIL gets thinner, its oxygen content decreases. Since vertical distribution of oxygen maintains the oxycline and the upper boundary of suboxic layer (Konovalov et al., 2002), hence, shallow CIL (thinner) enhances displacement of oxic, suboxic and anoxic layers upward. Comparison of the model simulated winter SST and CIL summer-autumn minimum temperature elucidates that there is a dramatic change in temperature. A continuous warming is found from 1985 to 2014 with winter SST changing from ~6.5 °C to 8.4 °C and summer-autumn CIL minimum temperature from ~5.6 °C to 7.5 showing a warming trend in the CIL temperature equal to ~0.0603 °C/yr. The CIL warming found in this study is consistent with the most recent studies of Stanev et al., (2019) who found that the warming trend is ~0.05 °C/yr which is found to be more than double the trend in the previous decades and Miladinova et al., (2018) who found that in the last two decades deep water temperature in the NWS which contributes in the formation of the CIL is approaching 8 °C.

There is no systematic relationship between interannual MLD variations and SST in the mode as this MLD anomaly is ~1.0 m over 30 years (Somavilla et al., 2017). Thus, it is preceived that the wind stress plays the key role in the deepening or shoaling of the MLD in the Black Sea. Referring to the wind curl variation in two specific years 1999 and 2011 with a very shallow winter MLD it is seen that wind curl has its minimum and the year 2003 with larger wind curl corresponds to a deeper MLD.

SST distribution in the Black Sea has been compared to satellite SST data obtained from NOAA AVHRR satellite indicating model efficiency in computation of SST with a bias -1.27 °C. This is most likely due to the evaporation coefficient used in the model. Evaporation is calculated by model itself and it is adjusted through a coefficient. To find a proper value for evaporation coefficient, ECMWF Era-Interim evaporation data is used which leads to a bias between reanalysis data and actual evaporation in the Black Sea. Higher evaporation rate results in cooling of SST which creates underestimation of SST by model. However, the model is capable of reproducing accurate spatial distribution of SST as illustrated by the EOF analysis. The first spatial and temporal modes of SST EOF analysis is correlated with mean satellite SST with a correlation coefficient of 0.99, which is mainly due to SST restoring used in the model. The second and third spatial modes describe zonal (west to east) and meridional (northeast to southwest) temperature gradients as described in Capet et al., (2014) and Miladinova et al., (2017). The SST gradient in the basin is an indication of the Rim Current impact on the spatial distribution of the SST variation with lower temperatures in the NWS and western Black Sea and higher temperatures in the eastern Black Sea. It shows the transport of cold water masses from western Black Sea resulting cooler temperatures in the southwestern Black

Sea and transport of heat gained water masses from the eastern Black Sea to the northeastern Black Sea which itself is the signature of the thermohaline circulation in the Black Sea. EOF first temporal mode of SST indicates the warming trend of SST from 1985 to 2014 and the third mode gives seasonal SST changes showing that model is capable of detecting interannual and seasonal variability. Continuous SST increase over 30 years is consistent with findings of Oguz (2006), Oguz et al., (2006), Kazmin et al., (2010), Akpinar (2016) and Miladinova et al., (2017).

Characteristic dynamical features of general circulation of the Black Sea are comprised of the Rim Current and mesoscale eddies. First spatial EOF mode of SSH describes water budget and mean SSH anomaly of the Black Sea with a correlation coefficient of 0.99 in comparison to satellite SSH indicating model is able to capture mean dynamics of the Black Sea. The second spatial mode with higher values in the periphery and lower values in the basin interior represents the most important general circulation of the Black Sea, the Rim Current. SSH second spatial mode of the model and satellite are significantly correlated (r = 0.69) but a distinct variability in the southeastern Black Sea where the Batumi eddy resides is observed, which has also been experienced in the study of Capet et al., (2012). The third spatial mode of model SSH has a lower correlation with satellite data (r = 0.34) which is representative of meso- and sub-mesoscale dynamics of the Black Sea. This is an expected mismatch between model computation and satellite data due to lack of SSH/SLA assimilation and the error caused by the low resolution of the atmospheric forcing fields. SSH data assimilation has been applied by Grayek et al., (2010), however, they found the same mismatch of model SSH output and satellite data while data assimilation is turned off. Their model is only able to replicate observed maximum in the amplitudes of interior basin oscillations (Grayek et al., 2010). In the current model, SSH standard deviation excluding coastal areas is found to be 0.075 m (7.5 cm) which is close to the values 6.0 to 9.0 cm calculated in the study of Kara et al., (2008).

A shoaling of nitrate maximum-oxygen minimum isopycnal (15.4 kg/m^3) is detected in simulations. The depth varies from 95.7 m in 1985 to 77.1 m in 2014 showing ~18.6 m shoaling of oxic and suboxic layers. As described in 3.1 pycnocline is conserved and there is no considerable drift from initial conditions which implies model is able to detect shoaling of oxic and suboxic layers. Shoaling of 15.4 kg/m^3 isopycnal follows CIL depth shoaling which varies from 140 m to 100 m. Similar shoaling phenomenon is found in observational studies of Tugrul et al., (2014) and Capet at al., (2016). Findings of Capet et al., (2016) show that oxygen penetrated depth in 1985 is ~105 m and in 2005 it shoals to ~95 m. There is ~10 m difference between maximum oxygen concentration depth (ship-based oxygen profiles and Argo floats data by Capet et al., 2016) and 15.4 kg/m^3 isopycnal displacement captured by model. This depth difference can be due to model bias over 30 years.

Continuous SST warming trend (Oguz et al., 2006; Kazmin et al., 2010; Akpinar 2016; Miladinova et al., 2017) and limiting ventilation processes (Capet et al., 2014) result in CIL shoaling and hence oxygen penetration depth reduction. Findings of Stanev et al., (2013) also confirms that there is a noticeable shift in the upper boundary of suboxic layer (boundary between oxic and suboxic layer) over 50 years from 16.5 kg/m^3 to 15.5 kg/m^3 confirming displacement of oxic, suboxic and hence anoxic layers over a long period.

Variability of the Black Sea TKE, MKE and EKE climatologies reveal that energy variation follows wind stress curl changes as the main driver of the Black Sea circulation system. Figure 47 and Figure 52 show that in winter with the presence of strong winds TKE, MKE and EKE gain their maximum magnitude and in summer when wind weakens they have minimum magnitudes. The Rim Current speed gains its maximum (ADT-2, Figure 46) in February at the time (January and February) when the wind stress curl has its maximum and in summer with dropped wind stress curl it weakens which is consistent with the study of Kubryakov and Stanhchny, (2015). This strong seasonal variability with intensification of the Rim Current in winter and its attenuation in summer is the main characteristic of the Black Sea dynamics which has been subject of several studies (e.g. Oguz et al., 1993; Oguz and Besiktepe, 1999; Korotaev et al., 2003). Comparison of MKE with total number of eddies (Figure 50) demonstrates intensification of eddy activity in the Black Sea as a result of the Black Sea general circulation weakening. Hence, a major contribution to MKE and in general kinetic energy originates from the main feature of the Black Sea circulation, the Rim Current. As forcing of circulation (i.e. wind) weakens and consequently, the Rim Current decelerates and disintegrates into eddies, while intensification of the Rim Current and its shift toward the coast as a result of strong wind forcing in winter suppresses eddies leading to decrease in number of eddies. Total number of eddies detected through eddyscan algorithm (140 eddies detected) is larger than the number of eddies mentioned in Kubryakov and Stanichny, (2015), (66 eddies). This difference is due to coarse resolution of satellite data and the different methods used for the detection of eddies, as that study was limited to eddies exceeding 40 km in diameter (Kubryakov and Stanichny, 2015) which is the main reason for the difference in detection of eddies between the studies.

It is found that eddies, filaments and meanders of the Rim Current are the main mechanisms in the cross-shelf water exchange (Oguz et al., 2002; Zatsepin et al., 2003; Shapiro et al., 2010; Zhou et al., 2014). Transport of nutrients by either mesoscale cyclonic or anticyclonic eddies from inshore to offshore and their ability in generating localized regions of higher productivity reveals their major role in facilitating exchanges between the shelf and deep sea waters (Shapiro et al., 2010). Analyses of the Rim Current and eddy activity role in the box area (Figure 1) show that transport mechanism

106

in the Black Sea is highly dependent on the wind stress curl and the kinetic energy transferred from atmosphere to the ocean. In the periods with strong winds the Rim Current is the dominant mechanism driving horizontal transport which acts as a dynamic barrier preventing the transport of nutrients from inshore to the interior basin. In that time the model shows only west-east transport of mass in the southern Black Sea where the area of the study has been located. This is identical to findings of Kubryakov et al., (2018) conducted in the NWS of the Black Sea where Danube plume waters are locked by strong Rim Current and transferred in a southern direction in the form of a geostrophic alongshore current and the exchange between the shelf and deep sea is inhibited (Kubryakov et al., 2018). Similar to strong horizontal velocities at the time of strong Rim Current, in upper 150 m high vertical velocities (both in upward and downward) are observed. Results show that during strong Rim Current in winter and in the period when strong eddies are generated (late winter, early spring) higher vertical velocities of about 4×10^{-4} m/s as an influence of strong Rim Current and/or eddy activity resulting in upwelling and/or downwelling processes are captured while in spring and summer as winds weaken and kinetic energy is minimum vertical velocities are very small and even levels of no motion are observed.

Baroclinic instability of the Rim Current in response to decrease of the wind stress curl results in formation of powerful eddies in the cross-shelf break which have higher horizontal velocities (both x- and y-component) in March. Velocity transect plots indicate that these eddies play a dual transport role, west-east (east-west) transport on their south (north) edges and south-north (north-south) exchange on their west (east) edges. Newborn eddies are energetic with high horizontal and vertical velocities and hence their role in the exchange between the shelf and deep sea is inevitable. Consequently, in the period of decreasing TKE/MKE from maximum to minimum eddies act as a cross-boundary agent in the Black Sea.

In the period with minimum TKE/MKE in late spring and summer Rim Current breaks into a large number of eddies. However, it is found that these eddies are not as energetic as the eddies in winter and early spring. Although the number of eddies are high, they are very slow and the associate vertical velocities also are low. From mid-spring to mid-summer (April-August) eddies have their minimum EKE due to losing their energy gained from the Rim Current and deceleration of the wind stress curl. In vertical during winter strong winds break down stratification and hence, mixing process enhances higher vertical velocities. Similarly, in late winter and early spring when energetic eddies exist vertical velocities are relatively high. Consequently, as a result of high vertical velocities upwelling and downwelling processes facilitate transport of water masses and hence nutrients up/downward in the Black Sea. Higher kinetic energy provides both horizontal and vertical transport

of water masses in the Black Sea. In late spring and summer as the Rim Current weakens and eddies lose their energy and horizontal velocities cannot support the exchange between the shelf and interior basin likewise, vertical velocities reduce prohibiting vertical transport of water masses and hence, nutrients.

Decadal variation of number of eddies shows periodical increase or decrease over 30 years. Referring to wind stress curl data it is found that there is a negative correlation between the number of eddies and wind stress curl, meaning that wind regime influences generation or dissipation of eddies in the Black Sea.

Owing to the high horizontal resolution (3 km × 3 km) of model, mesoscale eddies ($O(10 - 100$ km)) which include coherent vortices as well as filaments, fronts, jets and spirals that carry out exchange between the continental shelf and offshore are well resolved. Surface layer circulation patterns demonstrate the high mesoscale eddy variability in the Black Sea with presence of quasi-permanent eddies enhancing physical, chemical and biological processes. However, sub-mesoscale eddies ($O(0.1 - 10$ km) less than 10 km are not resolved.

Frontal jets and frontogenesis, which is an active sub-mesoscale process that rapidly sharpens the horizontal density gradient at the surface, are processes regulating nutrient transport and enhance productivity. Results of horizontal and vertical velocities described in section 4.3 indicate that these processes may play a major role in amplification of productivity and upward/downward transport of nutrients in the Black Sea. However, this should be studied in detail in future studies.

CHAPTER 6

SUMMARY AND CONCLUSION

This dissertation studies the role of dynamic physical processes in nutrient transport in the Black Sea through numerical modeling of the Black Sea hydrodynamics. The three dimensional Nucleus for European Modeling of the Ocean (NMEO) is used to simulate the general circulation of the Black Sea with a resolution of 3 km × 3 km in horizontal and 61 z-levels in vertical from 1985 to 2014. Model has been tested and thoroughly validated applying univariate and multivariate skill assessment methods. To achieve a long term (30 years) conservation of salt and water content Bosphorus Strait has been parameterized as a two-layer exchange which makes it a prominent approach in Black Sea hydrodynamic modeling. To avoid artificial drifts in temperature and salinity simulation nudging technique has been applied below 207 m. Hence upper layer model dynamics is not influenced by nudging process.

Analyses of model output physical properties (e.g. SST, SSS, MLD, CIL, isopycnal 15.4 kg/m^3) indicate a continuous warming trend over 30 years in the period between 1985-2014 with a warming trend of 0.0603 °C/year. Winter SST warming shows ~1.81 °C increase from 1985 to 2014 which influences CIL summer temperature to reach 7.50 °C in 2014 with an increase of ~1.81 °C over 30 years. Accordingly, CIL depth has changed becoming shallower from 134.5 m in 1985 to 102.9 m in 2014. Following the CIL changes the isopycnal 15.4 kg/m^3, which is the signature of oxygen minimum and nitrate maximum in the Black Sea shoals from ~96 m in 1985 to ~77 m in 2014. These trends detected by the model agree with findings in the literature.

To investigate the role of dynamic processes in horizontal and vertical transport which constitutes the main goal of this study, temporal variability of the Rim Current and mesoscale eddies in the Black Sea and their connection with the wind stress curl, TKE, MKE and EKE is investigated over 30 years. Results of the study show that the wind plays the main role in driving general circulation of the Black Sea. Kinetic energy of the Black Sea is strongly correlated to the wind regime in addition to Ekman pumping velocity. Analyses show that the Rim Current gains its maximum velocity and strength in February at the time when kinetic energy is maximum as a result of strong winds presence and in June-July is weak when kinetic energy is at a minimum. In late winter and early spring the Rim Current starts losing its strength which coincides with its decomposition into a number of anticyclonic eddies resulting in the formation of energetic eddies between the coast and

Rim Current path. These eddies are fast and play an important role in transport of water masses from the continental shelf toward the interior basin and hence inshore offshore nutrient exchange. Results of the study revealed that approaching summer the number of eddies increase while they lose their energy because of the absence of strong winds and inshore offshore transport of water reduces. Strong winds enhance the transfer of energy from atmosphere to the ocean in winter and break down stratification resulting deep mixing and higher vertical velocities. Similarly, generation of energetic eddies (cyclonic and anticyclonic) in late winter and early spring while their movement causes upwelling/downwelling leading to upward/downward transport of water. It is perceived that physical mechanisms in winter enhance both horizontal and vertical transport of nutrients in the Black Sea while as energy transfer reduces the Rim Current weakens and eddies lose their energy leading to decrease in horizontal and vertical water transport. Consequently, it is inferred that late winter and early spring is the time period with effective water mass transport to the inner basin in both horizontal and vertical leading to higher biological productivity in the Black Sea.

A precise understanding of ocean dynamics and its investigation through modeling is highly dependent on model accuracy. One of major challenges in ocean modeling remains realistic atmospheric forcing data and initial conditions data. In the present study, coarse spatial resolution of ECMWF Era-Interim forcing data in the Black Sea region is likely to have an effect on model outcome. The wind data in Era-Interim is known to be rather unrealistic. For instance, reanalysis wind data did not show a shift in wind stress curl in 2002 to a high variability regime, while it was captured by QuickScat wind dataset. In addition, the heat flux calculated from ERA-interm data proved problematic. Restoring of SST using satellite data as described in 2.2.7 solved the problem of heat flux to some extent. The deviation of model simulated SSH from satellite data was another challenge in this study which resulted in difference in spatial occurrence of transient mesoscale features as captured by the EOF analysis. This deficiency can be solved through data assimilation of SSH into the model which will be a choice for further development of this high resolution Black Sea hydrodynamic model for further research.

REFERENCES

Acha, E. M., Mianzan, H. W., Guerrero, R. A., Favero, M., & Bava, J. (2004). Marine fronts at the continental shelves of austral South America: physical and ecological processes. *Journal of Marine systems*, *44*(1), 83-105.

Akoglu, E., Salihoglu, B., Libralato, S., Oguz, T., & Solidoro, C. (2014). An indicator-based evaluation of Black Sea food web dynamics during 1960–2000. *Journal of Marine Systems*, *134*, 113-125.

Akpinar, A. (2016). Seasonal to decadal variablility in the physical and biological properties of the Black Sea and Levantine basin as inferred from satellite remote sensing (Ph. D. thesis). Middle East Technical University.

Akpinar, A., Fach, B. A., & Oguz, T. (2017). Observing the subsurface thermal signature of the Black Sea cold intermediate layer with Argo profiling floats. *Deep Sea Research Part I: Oceanographic Research Papers*, *124*, 140-152.

Altiok, H., & Kayisoglu, M. (2015). Seasonal and interannual variability of water exchange in the Strait of Istanbul. *Mediterranean Marine Science*, *16*(3), 644-655.

Alvera Azcarate, A., Barth, A., Sirjacobs, D., & Beckers, J. M. (2009). Enhancing temporal correlations in EOF expansions for the reconstruction of missing data using DINEOF. *Ocean Science*, *5*(4), 475-485.

ALVERA-AZCÁRATE, A., Barth, A., Sirjacobs, D., Lenartz, F., & Beckers, J. M. (2011). Data Interpolating Empirical Orthogonal Functions (DINEOF): a tool for geophysical data analyses. *Mediterranean Marine Science*, *12*(3), 5-11.

Apeldorn, D. & Bouwman, L. (2014); SES land –based runoff and nutrient load data. www.perseus-net.eu

Arkhipkin, V. S., Gippius, F. N., Koltermann, K. P., & Surkova, G. V. (2014). Wind waves in the Black Sea: results of a hindcast study. *Natural Hazards and Earth System Sciences*, *14*(11), 2883.

Arkin, S., Akpinar, A., Fach, B. A., Salihoglu, B. & Oguz T. (2016), The link between climate, circulation and phytoplankton biomass in the Black Sea. *Ocean Sciences Meeting, Ankara, Turkey, 2016.*

Bernard, B., Madec, G., Penduff, T., Molines, J. M., Treguier, A. M., Le Sommer, J., ... & Derval, C. (2006). Impact of partial steps and momentum advection schemes in a global ocean circulation model at eddy-permitting resolution. *Ocean dynamics*, *56*(5-6), 543-567.

Barceló-Llull, B., Mason, E., Capet, A., & Pascual, A. (2016). Impact of vertical and horizontal advection on nutrient distribution in the southeast Pacific. *Ocean Science*, *12*(4), 1003-1011.

Beckers, J. M., Barth, A., & Alvera-Azcárate, A. (2006). DINEOF reconstruction of clouded images including error maps? application to the Sea-Surface Temperature around Corsican Island. *Ocean Science*, *2*(2), 183-199.

(2015) Black Sea - Temperature and salinity observation collection V2. https://doi.org/10.12770/227e9f7b-ddfc-4004-b0e5-f4785d36d43f

Blokhina, M. D., & Afanasyev, Y. D. (2003). Baroclinic instability and transient features of mesoscale surface circulation in the Black Sea: Laboratory experiment. *Journal of Geophysical Research: Oceans*, *108*(C10).

Cannaby, H., Fach, B. A., Arkin, S. S., & Salihoglu, B. (2015). Climatic controls on biophysical interactions in the Black Sea under present day conditions and a potential future (A1B) climate scenario. *Journal of Marine Systems*, *141*, 149-166.

Capet, A., Barth, A., Beckers, J. M., & Marilaure, G. (2012). Interannual variability of Black Sea's hydrodynamics and connection to atmospheric patterns. *Deep Sea Research Part II: Topical Studies in Oceanography*, *77*, 128-142.

Capet, A., Troupin, C., Carstensen, J., Grégoire, M., & Beckers, J. M. (2014). Untangling spatial and temporal trends in the variability of the Black Sea Cold Intermediate Layer and mixed Layer Depth using the DIVA detrending procedure. *Ocean Dynamics*, *64*(3), 315-324.

Capet, A., Stanev, E., Beckers, J. M., Murray, J., & Grégoire, M. (2016). Decline of the Black Sea oxygen inventory. *Biogeosciences*, *13*, 1287-1297.

Carton, J. A., Chepurin, G. A., Chen, L., & Grodsky, S. A. (2018). Improved global net surface heat flux. *Journal of Geophysical Research: Oceans*, *123*(5), 3144-3163.Castellari, S., Pinardi, N., &

Leaman, K. (1998). A model study of air–sea interactions in the Mediterranean Sea. *Journal of Marine Systems*, *18*(1-3), 89-114.

Casati, B., Ross, G., & Stephenson, D. B. (2004). A new intensity-scale approach for the verification of spatial precipitation forecasts. *Meteorological Applications*, *11*(2), 141-154.

Castellari, S., Pinardi, N., & Leaman, K. (1998). A model study of air–sea interactions in the Mediterranean Sea. *Journal of Marine Systems*, *18*(1-3), 89-114.

Chadwick, R., Good, P., & Willett, K. (2016). A simple moisture advection model of specific humidity change over land in response to SST warming. *Journal of Climate*, *29*(21), 7613-7632.

Cummins, P. F. (1991). The deep water stratification of ocean general circulation models. *Atmosphere-Ocean*, *29*(3), 563-575.

Dalziel, S. B. (1991). Two-layer hydraulics: a functional approach. *Journal of Fluid Mechanics*, *223*, 135-163.

Dee, D. P., Uppala, S. M., Simmons, A. J., Berrisford, P., Poli, P., Kobayashi, S., ... & Bechtold, P. (2011). The ERA-Interim reanalysis: configuration and performance of the data assimilation system, QJ Roy. Meteor. Soc., 137, 553–597.

Demyshev, S. G., & Evstigneeva, N. A. (2016). Modeling meso-and sub-mesoscale circulation along the eastern Crimean coast using numerical calculations. *Izvestiya, Atmospheric and Oceanic Physics*, *52*(5), 560-569.

Dunstan, P. K., Foster, S. D., King, E., Risbey, J., O'Kane, T. J., Monselesan, D., ... & Thompson, P. A. (2018). Global patterns of change and variation in sea surface temperature and chlorophyll a. *Scientific reports*, *8*(1), 14624.

Epicoco, I., & Mocavero, S. (2012, June). The performance model of an enhanced parallel algorithm for the SOR method. In *International Conference on Computational Science and Its Applications* (pp. 44-56). Springer, Berlin, Heidelberg.

Faghmous, J. H., Styles, L., Mithal, V., Boriah, S., Liess, S., Kumar, V., ... & dos Santos Mesquita, M. (2012, October). Eddyscan: A physically consistent ocean eddy monitoring application. In *2012 Conference on Intelligent Data Understanding* (pp. 96-103). IEEE.

Giardino, A., di Leo, M., Bragantini, G., de Vroeg, H., Tonnon, P. K., Huisman, B., & de Bel, M. (2015). An Integrated Sediment Management Scheme for the Coastal Area of Batumi (Georgia). In *Proceedings of the MEDCOAST 2015 Conference. Varna, Bulgaria*.

Ginzburg, A. I., Kostianoy, A. G., & Sheremet, N. A. (2007). Sea surface temperature variability. In *The Black Sea Environment* (pp. 255-275). Springer, Berlin, Heidelberg.

Goosse, H., Deleersnijder, E., Fichefet, T., & England, M. H. (1999). Sensitivity of a global coupled ocean-sea ice model to the parameterization of vertical mixing. *Journal of Geophysical Research: Oceans*, *104*(C6), 13681-13695.

Graham, J. A., O'Dea, E., Holt, J., Polton, J., Hewitt, H. T., Furner, R., Guihou, K., Brereton, A., Arnold, A., Wakelin, S., Castillo Sanchez, J. M.,& Mayorga Adame, C. G.,(2017): AMM15: A new high resolution NEMO configuration for operational simulation of the European North West Shelf. *Geosci. Model Dev. Discuss, https://doi.org/10.5194/gmd-2017-127,* 1-23.

Grayek, S., Stanev, E. V., & Kandilarov, R. (2010). On the response of Black Sea level to external forcing: altimeter data and numerical modelling. *Ocean Dynamics*, *60*(1), 123-140.

Haustein, K., Allen, M. R., Forster, P. M., Otto, F. E. L., Mitchell, D. M., Matthews, H. D., & Frame, D. J. (2017). A real-time global warming index. *Scientific reports*, *7*(1), 15417.

Hill, C., Ferreira, D., Campin, J. M., Marshall, J., Abernathey, R., & Barrier, N. (2012). Controlling spurious diapycnal mixing in eddy-resolving height-coordinate ocean models–Insights from virtual deliberate tracer release experiments. *Ocean Modelling*, *45*, 14-26.

Holt, J., Schrum, C., Cannaby, H., Daewel, U., Allen, I., Artioli, Y., ... & Pushpadas, D. (2016). Potential impacts of climate change on the primary production of regional seas: A comparative analysis of five European seas. *Progress in Oceanography*, *140*, 91-115.

Iovino, D., Masina, S., Storto, A., Cipollone, A., & Stepanov, V. N. (2016). A 1/16 eddying simulation of the global NEMO sea-ice–ocean system. *Geoscientific Model Development*, *9*(8), 2665-2684.

Jaoshvili, S. (2002). *The rivers of the Black Sea*. Copenhagen: European Environment Agency.

Jose, Y. S., Aumont, O., Machu, E., Penven, P., Moloney, C. L., & Maury, O. (2014). Influence of mesoscale eddies on biological production in the Mozambique Channel: Several contrasted examples

from a coupled ocean-biogeochemistry model. *Deep Sea Research Part II: Topical Studies in Oceanography*, *100*, 79-93.

Juza, M., Escudier, R., Pascual, A., Pujol, M. I., Taburet, G., Troupin, C., ... & Tintoré, J. (2016). Impacts of reprocessed altimetry on the surface circulation and variability of the Western Alboran Gyre. *Advances in Space Research*, *58*(3), 277-288.

Kara, A. B., Hurlburt, H. E., Wallcraft, A. J., & Bourassa, M. A. (2005). Black Sea mixed layer sensitivity to various wind and thermal forcing products on climatological time scales. *Journal of climate*, *18*(24), 5266-5293.

Kara, A. B., Wallcraft, A. J., Hurlburt, H. E., & Stanev, E. V. (2008). Air–sea fluxes and river discharges in the Black Sea with a focus on the Danube and Bosphorus. *Journal of Marine Systems*, *74*(1), 74-95.

Kara, A. B., Barron, C. N., Wallcraft, A. J., & Oguz, T. (2008). Interannual variability of sea surface height over the Black Sea: relation to climatic patterns. *Earth Interactions*, *12*(10), 1-11.

Karger, D. N., Conrad, O., Böhner, J., Kawohl, T., Kreft, H., Soria-Auza, R. W., ... & Kessler, M. (2017). Climatologies at high resolution for the earth's land surface areas. *Scientific data*, *4*, 170122.

Kazmin, A. S., Zatsepin, A. G., & Kontoyiannis, H. (2010). Comparative analysis of the long-term variability of winter surface temperature in the Black and Aegean Seas during 1982–2004 associated with the large-scale atmospheric forcing. *International Journal of Climatology*, *30*(9), 1349-1359.

Kliem, N., & Pietrzak, J. D. (1999). On the pressure gradient error in sigma coordinate ocean models: A comparison with a laboratory experiment. *Journal of Geophysical Research: Oceans*, *104*(C12), 29781-29799.

Knysh, V. V., Korotaev, G. K., Moiseenko, V. A., Kubryakov, A. I., Belokopytov, V. N., & Inyushina, N. V. (2011). Seasonal and interannual variability of Black Sea hydrophysical fields reconstructed from 1971–1993 reanalysis data. *Izvestiya, Atmospheric and Oceanic Physics*, *47*(3), 399.

Konovalov, S. K., Murray, J. W., Luther, G. W., Buesseler, K. O., Friederich, G., Tebo, B. M., ... & Clement, B. (2002). Oxygen Fluxes, Redox Processes and the Suboxic Zone in the Black Sea (046-047 combined).

Korotaev, G. K., Saenko, O. A., & Koblinsky, C. J. (2001). Satellite altimetry observations of the Black Sea level. *Journal of Geophysical Research: Oceans*, *106*(C1), 917-933.

Korotaev, G., Oguz, T., Nikiforov, A., & Koblinsky, C. (2003). Seasonal, interannual, and mesoscale variability of the Black Sea upper layer circulation derived from altimeter data. *Journal of Geophysical Research: Oceans*, *108*(C4).

Korotenko, K. A. (2015). Modeling mesoscale circulation of the Black Sea. *Oceanology*, *55*(6), 820-826.

Kubryakov, A. A., & Stanichny, S. V. (2015). Seasonal and interannual variability of the Black Sea eddies and its dependence on characteristics of the large-scale circulation. *Deep Sea Research Part I: Oceanographic Research Papers*, *97*, 80-91.

Kubryakov, A. A., Stanichny, S. V., Zatsepin, A. G., & Kremenetskiy, V. V. (2016). Long-term variations of the Black Sea dynamics and their impact on the marine ecosystem. *Journal of Marine Systems*, *163*, 80-94.

Kubryakov, A. A., Stanichny, S. V., & Zatsepin, A. G. (2018). Interannual variability of Danube waters propagation in summer period of 1992–2015 and its influence on the Black Sea ecosystem. *Journal of Marine Systems*, *179*, 10-30.

Kubryakov, A., Stanichny, S., Shokurov, M., & Garmashov, A. (2019). Wind velocity and wind curl variability over the Black Sea from QuikScat and ASCAT satellite measurements. *Remote sensing of environment*, *224*, 236-258.

Lane-Serff, G. F., Rohling, E. J., Bryden, H. L., & Charnock, H. (1997). Postglacial connection of the Black Sea to the Mediterranean and its relation to the timing of sapropel formation. *Paleoceanography*, *12*(2), 169-174.

Large, W. G., & Yeager, S. G. (2004). Diurnal to decadal global forcing for ocean and sea-ice models: the data sets and flux climatologies.

Lemarié, F., Kurian, J., Shchepetkin, A. F., Molemaker, M. J., Colas, F., & McWilliams, J. C. (2012). Are there inescapable issues prohibiting the use of terrain-following coordinates in climate models?. *Ocean Modelling*, *42*, 57-79.

Li, Q. P., Franks, P. J., Ohman, M. D., & Landry, M. R. (2012). Enhanced nitrate fluxes and biological processes at a frontal zone in the southern California current system. *Journal of plankton research*, *34*(9), 790-801.

Lima, I. D., Olson, D. B., & Doney, S. C. (2002). Biological response to frontal dynamics and mesoscale variability in oligotrophic environments: Biological production and community structure. *Journal of Geophysical Research: Oceans*, *107*(C8).

Locarnini, R. A., Mishonov, A.V., Antonov, J.I., Boyer, T.P., Garcia, H.E., Baranova, O.K., Zweng, M.M., Paver, C.R., Reagan, J.R., Johnson, D.R., Hamilton, M., Seidov, D. (2013). World Ocean Atlas 2013, Volume 1: Temperature. S., Levitus, Ed.; A., Mishonov, Technical Ed.; NOAA Atlas NESDIS 73,40pp.

Ludwig, W., Dumont, E., Meybeck, M., & Heussner, S. (2009). River discharges of water and nutrients to the Mediterranean and Black Sea: major drivers for ecosystem changes during past and future decades? *Progress in Oceanography*, *80*(3), 199-217.

Ludwig, W., A. F. Bouwman, E. Dumont, & F. Lespinas. "Water and nutrient fluxes from major Mediterranean and Black Sea rivers: Past and future trends and their implications for the basin-scale budgets." *Global biogeochemical cycles* 24, no. 4 (2010).

Madec, G. (2015). NEMO ocean engine.

Maes, C., & O' Kane, T. J. (2014). Seasonal variations of the upper ocean salinity stratification in the Tropics. *Journal of Geophysical Research: Oceans*, *119*(3), 1706-1722.

Martin, M. J., Balmaseda, M., Bertino, L., Brasseur, P., Brassington, G., Cummings, J., ... & Oke, P. R. (2015). Status and future of data assimilation in operational oceanography. *Journal of Operational Oceanography*, *8*(sup1), s28-s48.

Martinho, A. S., & Batteen, M. L. (2006). On reducing the slope parameter in terrain-following numerical ocean models. *Ocean Modelling*, *13*(2), 166-175.

McGillicuddy, D. J., Robinson, A. R., Siegel, D. A., Jannasch, H. W., Johnson, R., Dickey, T. D., ... & Knap, A. H. (1998). Influence of mesoscale eddies on new production in the Sargasso Sea. *Nature*, *394*(6690), 263-266.

Medhaug, I., Stolpe, M. B., Fischer, E. M., & Knutti, R. (2017). Reconciling controversies about the 'global warming hiatus'. *Nature*, *545*(7652), 41.

Mellor, G. L., Oey, L. Y., & Ezer, T. (1998). Sigma coordinate pressure gradient errors and the seamount problem. *Journal of Atmospheric and Oceanic Technology*, *15*(5), 1122-1131.

Menna, M., & Poulain, P. M. (2014). Geostrophic currents and kinetic energies in the Black Sea estimated from merged drifter and satellite altimetry data. *Ocean Science*, *10*(2), 155-165.

Miladinova, S., Stips, A., Garcia-Gorriz, E., & Macias Moy, D. (2017). Black Sea thermohaline properties: Long-term trends and variations. *Journal of Geophysical Research: Oceans*.

Miladinova, S., Stips, A., Garcia-Gorriz, E., & Moy, D. M. (2018). Formation and changes of the Black Sea cold intermediate layer. *Progress in oceanography*, *167*, 11-23.

Mizyuk, A. I., Senderov, M. V., Korotaev, G. K., & Sarkysyan, A. S. (2016). Features of the horizontal variability of the sea surface temperature in the Western Black Sea from high resolution modeling. *Izvestiya, Atmospheric and Oceanic Physics*, *52*(5), 570-578.

Murray, J. W., Top, Z., & Özsoy, E. (1991). Hydrographic properties and ventilation of the Black Sea. *Deep Sea Research Part A. Oceanographic Research Papers*, *38*, S663-S689.

Neves, A. A. S., Pinardi, N., & Martins, F. (2016). IT-OSRA: applying ensemble simulations to estimate the oil spill risk associated to operational and accidental oil spills. *Ocean Dynamics*, *66*(8), 939-954.

O'dea, E. J., Arnold, A. K., Edwards, K. P., Furner, R., Hyder, P., Martin, M. J., ... & Liu, H. (2012). An operational ocean forecast system incorporating NEMO and SST data assimilation for the tidally driven European North-West shelf. *Journal of Operational Oceanography*, *5*(1), 3-17.

Oguz, T., Latun, V. S., Latif, M. A., Vladimirov, V. V., Sur, H. I., Markov, A. A., ... & Ünlüata, Ü. (1993). Circulation in the surface and intermediate layers of the Black Sea. *Deep Sea Research Part I: Oceanographic Research Papers*, *40*(8), 1597-1612.

Oguz, T., Aubrey, D. G., Latun, V. S., Demirov, E., Koveshnikov, L., Sur, H. I., ... & Eremeev, V. (1994). Mesoscale circulation and thermohaline structure of the Black Sea observed during HydroBlack'91. *Deep Sea Research Part I: Oceanographic Research Papers*, *41*(4), 603-628.

Oguz, T., Malanotte-Rizzoli, P., & Aubrey, D. (1995). Wind and thermohaline circulation of the Black Sea driven by yearly mean climatological forcing. *Journal of Geophysical Research: Oceans*, *100*(C4), 6845-6863.

Oguz, T., & Malanotte-Rizzoli, P. (1996). Seasonal variability of wind and thermohaline-driven circulation in the Black Sea: Modeling studies. *Journal of Geophysical Research: Oceans*, *101*(C7), 16551-16569.

Oguz, T., & Besiktepe, S. (1999). Observations on the Rim Current structure, CIW formation and transport in the western Black Sea. *Deep Sea Research Part I: Oceanographic Research Papers*, *46*(10), 1733-1753.

OGUZ, T. (2005). Black Sea ecosystem response to climatic teleconnections. *Oceanography*, *18*(2), 122-133.

Oguz, T., Deshpande, A. G., & Malanotte-Rizzoli, P. (2002). The role of mesoscale processes controlling biological variability in the Black Sea coastal waters: inferences from SeaWIFS-derived surface chlorophyll field. *Continental Shelf Research*, *22*(10), 1477-1492.

Oguz, T., TUGRUL, S., KIDEYS, A. E., EDIGER, V., & KUBILAY, N. (2005). . PYHSICAL AND BIOGEOCHEMICAL CHARACTERISTICS OF THE BLACK SEA (28, S). *The sea*, *14*, 1331-1369.

Oguz, T., Dippner, J. W., & Kaymaz, Z. (2006). Climatic regulation of the Black Sea hydro-meteorological and ecological properties at interannual-to-decadal time scales. *Journal of Marine Systems*, *60*(3-4), 235-254.

Oguz, T., & Gilbert, D. (2007). Abrupt transitions of the top-down controlled Black Sea pelagic ecosystem during 1960–2000: evidence for regime-shifts under strong fishery exploitation and nutrient enrichment modulated by climate-induced variations. *Deep Sea Research Part I: Oceanographic Research Papers*, *54*(2), 220-242.

Oguz, T. (2008). General oceanographic properties: physico-chemical and climatic features. *State of Environment of the Black Sea (2001-2006/7). Publication of the Commission on the Protection of the Black Sea Against Pollution (BSC). Istanbul, Turkey*, 39-60.

Oguz, T., Macias, D., Garcia-Lafuente, J., Pascual, A., & Tintore, J. (2014). Fueling plankton production by a meandering frontal jet: a case study for the alboran sea (Western mediterranean). *PloS one*, *9*(11), e111482.

Oguz, T., Mourre, B., & Tintoré, J. (2016). Upstream control of the frontal jet regulating plankton production in the Alboran Sea (Western Mediterranean). *Journal of Geophysical Research: Oceans*, *121*(9), 7159-7175.

Oguz, T. (2017). Impacts of a buoyant strait outflow on the plankton production characteristics of an adjacent semi-enclosed basin: A case study of the Marmara Sea. *Journal of Marine Systems*, *173*, 90-100.

Ortega, P., Guilyardi, É., Swingedouw, D., Mignot, J., & Nguyen, S. (2017). Reconstructing extreme AMOC events through nudging of the ocean surface: a perfect model approach. *Climate dynamics*, *49*(9-10), 3425-3441.

Özsoy, E., & Ünlüata, Ü. (1997). Oceanography of the Black Sea: a review of some recent results. *Earth-Science Reviews*, *42*(4), 231-272.

Pacanowski, R. C., & Gnanadesikan, A. (1998). Transient response in a z-level ocean model that resolves topography with partial cells. *Monthly Weather Review*, *126*(12), 3248-3270.

Penduff, T., Le Sommer, J., Barnier, B., Tréguier, A. M., Molines, J. M., & Madec, G. (2007). Influence of numerical schemes on current-topography interactions in 1/4 global ocean simulations. *Ocean Science Discussions*, *4*(3), 491-528.

Peneva, E., Stanev, E., Belokopytov, V., & Le Traon, P. Y. (2001). Water transport in the Bosphorus Straits estimated from hydro-meteorological and altimeter data: seasonal to decadal variability. *Journal of Marine Systems*, *31*(1-3), 21-33.

Penven, P., Marchesiello, P., Debreu, L., & Lefevre, J. (2008). Software tools for pre-and post-processing of oceanic regional simulations. *Environmental Modelling & Software*, *23*(5), 660-662.

Pitcher, G. C., Figueiras, F. G., Hickey, B. M., & Moita, M. T. (2010). The physical oceanography of upwelling systems and the development of harmful algal blooms. *Progress in Oceanography*, *85*(1-2), 5-32.

Podymov, O. I., Yakushev, E. V., & Kostyleva, A. V. (2011). On Interannual Variability of Chemical Characteristics of Redox Layer and Cold Intermediate Layer of the Black Sea. In *Chemical Structure of Pelagic Redox Interfaces* (pp. 121-135). Springer, Berlin, Heidelberg.

Reffray, G., Bourdalle-Badie, R., & Calone, C. (2015). Modelling turbulent vertical mixing sensitivity using a 1-D version of NEMO. *Geoscientific Model Development*, *8*(1), 69-86.

Ross, D. A., Uchupi, E., Prada, K. E., & MacIlvaine, J. C. (1974). Bathymetry and Microtopography of Black Sea: Structure.

Salihoglu, B., Arkin, S. S., Akoglu, E., & Fach, B. A. (2017). Evolution of future Black Sea fish stocks under changing environmental and climatic conditions. *Frontiers in Marine Science*, *4*, 339.

Shapiro, G. I., Aleynik, D. L., & Mee, L. D. (2010). Long term trends in the sea surface temperature of the Black Sea. *Ocean Science*, (2).

Shapiro, G. I., Stanichny, S. V., & Stanychna, R. R. (2010). Anatomy of shelf–deep sea exchanges by a mesoscale eddy in the North West Black Sea as derived from remotely sensed data. *Remote Sensing of Environment*, *114*(4), 867-875.

Shapiro, G., Luneva, M., Pickering, J., & Storkey, D. (2013). The effect of various vertical discretization schemes and horizontal diffusion parameterization on the performance of a 3-D ocean model: the Black Sea case study. *Ocean Science*, *9*(2), 377.

Sheppard, C. (Ed.). (2018). *World Seas: An Environmental Evaluation: Volume I: Europe, The Americas and West Africa*. Academic Press.

Shutler, J. D., Smyth, T. J., Saux-Picart, S., Wakelin, S. L., Hyder, P., Orekhov, P., ... & Allen, J. I. (2011). Evaluating the ability of a hydrodynamic ecosystem model to capture inter-and intra-annual spatial characteristics of chlorophyll-a in the north east Atlantic. *Journal of Marine Systems*, *88*(2), 169-182.

Sikirić, M. D., Janeković, I., & Kuzmić, M. (2009). A new approach to bathymetry smoothing in sigma-coordinate ocean models. *Ocean Modelling*, *29*(2), 128-136.

Simoncelli, S., Coatanoan, C., Myroshnychenko, V., Sagen, H., Back, O., Scory, S., ... & Fichaut, M. (2015). Second release of the SeaDataNet aggregated data sets products, WP10 Fourth Year Report–DELIVERABLE D10. 4.

Somavilla, R., González-Pola, C., & Fernández-Diaz, J. (2017). The warmer the ocean surface, the shallower the mixed layer. How much of this is true?. *Journal of Geophysical Research: Oceans*

Soontiens, N., Allen, S. E., Latornell, D., Le Souëf, K., Machuca, I., Paquin, J. P., ... & Korabel, V. (2016). Storm surges in the Strait of Georgia simulated with a regional model. *Atmosphere-Ocean*, *54*(1), 1-21.

Sorgente, R., Olita, A., Oddo, P., Fazioli, L., & Ribotti, A. (2011). Numerical simulation and decomposition of kinetic energy in the Central Mediterranean: insight on mesoscale circulation and energy conversion. *Ocean Science (OS)*.

Stanev, E. V., & Beckers, J. M. (1999). Numerical simulations of seasonal and interannual variability of the Black Sea thermohaline circulation. *Journal of Marine Systems*, *22*(4), 241-267.

Staneva, J. V., Dietrich, D. E., Stanev, E. V., & Bowman, M. J. (2001). Rim current and coastal eddy mechanisms in an eddy-resolving Black Sea general circulation model. *Journal of Marine Systems*, *31*(1-3), 137-157.

Stanev, E. V., Beckers, J. M., Lancelot, C., Staneva, J. V., Le Traon, P. Y., Peneva, E. L., & Grégoire, M. (2002). Coastal–open Ocean Exchange in the Black Sea: observations and modelling. *Estuarine, coastal and shelf science*, *54*(3), 601-620.

Stanev, E. V., Bowman, M. J., Peneva, E. L., & Staneva, J. V. (2003). Control of Black Sea intermediate water mass formation by dynamics and topography: Comparison of numerical simulations, surveys and satellite data. *Journal of Marine Research*, *61*(1), 59-99.

Stanev, E. V., Staneva, J., Bullister, J. L., & Murray, J. W. (2004). Ventilation of the Black Sea pycnocline. Parameterization of convection, numerical simulations and validations against observed chlorofluorocarbon data. *Deep Sea Research Part I: Oceanographic Research Papers*, *51*(12), 2137-2169.

Stanev, E. V., He, Y., Grayek, S., & Boetius, A. (2013). Oxygen dynamics in the Black Sea as seen by Argo profiling floats. *Geophysical Research Letters*, *40*(12), 3085-3090.

Stanev, E. V., Grashorn, S., & Zhang, Y. J. (2017). Cascading ocean basins: numerical simulations of the circulation and interbasin exchange in the Azov-Black-Marmara-Mediterranean Seas system. *Ocean Dynamics*, 1-23.

Stanev, E. V., Poulain, P. M., Grayek, S., Johnson, K. S., Claustre, H., & Murray, J. W. (2018). Understanding the Dynamics of the Oxic-Anoxic Interface in the Black Sea. *Geophysical Research Letters*, *45*(2), 864-871.

Stanev, E. V., Peneva, E., & Chtirkova, B. (2019). Climate change and regional ocean water mass disappearance: Case of the Black Sea. *Journal of Geophysical Research: Oceans*.

Staneva, J., Kourafalou, V., & Tsiaras, K. (2010). Seasonal and Interannual Variability of the North-Western Black Sea Ecosystem. *Terrestrial, Atmospheric & Oceanic Sciences*, *21*(1).

Stewart, K., Kassakian, S., Krynytzky, M., DiJulio, D., & Murray, J. W. (2007). Oxic, suboxic, and anoxic conditions in the Black Sea. In *The Black Sea flood question: Changes in coastline, climate, and human settlement* (pp. 1-21). Springer, Dordrecht.

Storkey, D., Blockley, E. W., Furner, R., Guiavarc'h, C., Lea, D., Martin, M. J., ... & Siddorn, J. R. (2010). Forecasting the ocean state using NEMO: The new FOAM system. *Journal of operational oceanography*, *3*(1), 3-15.

Stow, C. A., Jolliff, J., McGillicuddy Jr, D. J., Doney, S. C., Allen, J. I., Friedrichs, M. A., ... & Wallhead, P. (2009). Skill assessment for coupled biological/physical models of marine systems. *Journal of Marine Systems*, *76*(1-2), 4-15.

Toderascu, R., & Rusu, E. (2013). Evaluation of the circulation patterns in the Black Sea using remotely sensed and in situ measurements. *International Journal of Geosciences*, *4*(7), 1009-1017.

Trotta, F., Fenu, E., Pinardi, N., Bruciaferri, D., Giacomelli, L., Federico, I., & Coppini, G. (2016). A Structured and Unstructured grid Relocatable ocean platform for Forecasting (SURF). *Deep Sea Research Part II: Topical Studies in Oceanography*, *133*, 54-75.

Tsiaras, K. P., Kourafalou, V. H., Davidov, A., & Staneva, J. (2008). A three-dimensional coupled model of the western Black Sea plankton dynamics: Seasonal variability and comparison to SeaWiFs data. *Journal of Geophysical Research: Oceans*, *113*(C7).

Tuğrul, S., Murray, J. W., Friederich, G. E., & Salihoğlu, İ. (2014). Spatial and temporal variability in the chemical properties of the oxic and suboxic layers of the Black Sea. *Journal of Marine Systems*, *135*, 29-43.

Umlauf, L., & Burchard, H. (2003). A generic length-scale equation for geophysical turbulence models. *Journal of Marine Research*, *61*(2), 235-265.

Ünlülata, Ü., Oğuz, T., Latif, M. A., & Özsoy, E. (1990). On the physical oceanography of the Turkish Straits. In *The physical oceanography of sea straits* (pp. 25-60). Springer Netherlands.

Vandenbulcke, L., Capet, A., Beckers, J. M., Grégoire, M., & Besiktepe, S. (2009). An operational implementation of the GHER model for the Black Sea, with SST and CTD data assimilation. *Ocean Science Discussions*, *6*(2), 1895-1911.

Vandenbulcke, L., Capet, A., Beckers, J. M., Grégoire, M., & Besiktepe, S. (2010). Onboard implementation of the GHER model for the Black Sea, with SST and CTD data assimilation. *Journal of Operational Oceanography*, *3*(2), 47-54.

von Schuckmann, K., Le Traon, P. Y., Smith, N., Pascual, A., Brasseur, P., Fennel, K., ... & Axell, L. (2018). Copernicus marine service ocean state report. *Journal of Operational Oceanography*, *11*(sup1), S1-S142.

Wang, Q., Wekerle, C., Danilov, S., Wang, X., & Jung, T. A 4.5 km resolution Arctic Ocean simulation with the global multi-resolution model FESOM1.4. *Geosci. Model Dev. Discuss.,https://doi.org/10.5194/gmd-2017-136,* 1-47.

Wang, Y., Zhang, H. R., Chai, F., & Yuan, Y. (2018). Impact of mesoscale eddies on chlorophyll variability off the coast of Chile. *PloS one*, *13*(9), e0203598.

Williams, R. G., & Follows, M. J. (2003). Physical transport of nutrients and the maintenance of biological production. In *Ocean biogeochemistry* (pp. 19-51). Springer, Berlin, Heidelberg.

Winther, N. G., & Evensen, G. (2006). A hybrid coordinate ocean model for shelf sea simulation. *Ocean Modelling*, *13*(3), 221-237.

Zalesnyi, V. B., Gusev, A. V., & Agoshkov, V. I. (2016). Modeling Black Sea circulation with high resolution in the coastal zone. *Izvestiya, Atmospheric and Oceanic Physics*, *52*(3), 277-293.

Zatsepin, A. G., Ginzburg, A. I., Kostianoy, A. G., Kremenetskiy, V. V., Krivosheya, V. G., Stanichny, S. V., & Poulain, P. M. (2003). Observations of Black Sea mesoscale eddies and associated horizontal mixing. *Journal of Geophysical Research: Oceans*, *108*(C8).

Zatsepin, A., Kubryakov, A., Aleskerova, A., Elkin, D., & Kukleva, O. (2019). Physical mechanisms of submesoscale eddies generation: evidences from laboratory modeling and satellite data in the Black Sea. *Ocean Dynamics*, *69*(2), 253-266.

Zhong, Y., & Bracco, A. (2013). Submesoscale impacts on horizontal and vertical transport in the Gulf of Mexico. *Journal of Geophysical Research: Oceans*, *118*(10), 5651-5668.

Zhou, F., Shapiro, G., & Wobus, F. (2014). Cross-shelf exchange in the northwestern Black Sea. *Journal of Geophysical Research: Oceans*, *119*(4), 2143-2164.

Zweng, M. M., Reagan, J. R., Antonov, J. I., Locarnini, R. A., Mishonov, A. V., Boyer, T. P., ... & Biddle, M. M. (2013). *World ocean atlas 2013. Volume 2:*Salinity.S.Levitus,Ed.;A. Mishonov,TechnicalEd.;NOAA Atlas NESDIS 74,39pp.

CURRICULUM VITAE

e-mail: ehsan@ims.metu.edu.tr

sadighehsan@gmail.com

ResearchGate: https://www.researchgate.net/profile/Ehsan_Sadighrad2

Education

Doctor of Philosophy, Oceanography

Middle East Technical University, Institute of Marine Sciences, Turkey

(September 2013 – September 2019)

Title: Investigating Mesoscale Physical Processes for Vertical and Horizontal Transport in the Black Sea with the Implementation of a High Resolution Model

Master of Science, Physical Oceanography

IAU, Science and Research Branch, Iran

(September 2004 – September 2007)

Title: A Two Layer Model for Thermohaline Circulation between Two Deep Enclosed Basins

Bachelor of Science, Applied Physics

IAU, Oroumieh Branch, Iran

(September 2000 – September 2004)